UNIVERSITY OF CALIFORNIA
SANTA CRUZ

Non-Traditional Stable Isotopes in Land-to-Sea Fluxes

A dissertation submitted in partial satisfaction
of the requirements for the degree of

DOCTOR OF PHILOSOPHY

in

OCEAN SCIENCES

by

Kimberley Bitterwolf

September 2020

The Dissertation of Kimberley K. Bitterwolf is approved by:

Dr. Adina Paytan, chair

Professor Christina Ravelo

Associate Professor Carl Lamborg

Dr. Bernhard Peucker-Ehrenbrink

Quentin Williams
Vice Provost and Dean of Graduate Studies

Table of Contents

List of Figures

CHAPTER 2

CHAPTER 3

CHAPTER 4

List of Tables

CHAPTER 2

CHAPTER 3

CHAPTER 4

Dissertation Abstract

Non-Traditional Stable Isotopes in Land-to-Sea Fluxes

by
Kimberley K. Bitterwolf

Earth's biogeochemical evolution is inferred from the elemental compositions of past seawater and the rock record. These reconstructions generally assume: 1) a known and relatively constant flux of continent-derived solutes through time, 2) that the isotopic composition of these input fluxes is constant over geologic timescales, and 3) that the sensitivity of isotope proxies is constant over geologic timescales. However, it is prudent to test these assumptions in the modern amidst a well-understood natural environment before applying them to reconstructions of the past, where far more unknowns exist. In Chapter 2, I quantified a previously unaccounted for input of continent-derived solutes: groundwater discharge. My results indicate that the global groundwater flux is responsible for 12 – 23% of the riverine flux for Li, Mg, Ca, Sr, and Ba. Moreover, only the isotopic compositions of $\delta^{7}Li$ and $\delta^{138}Ba$ were indistinguishable from riverine values. The $\delta^{26}Mg$, $\delta^{44}Ca$, $^{87}Sr/^{86}Sr$ and $\delta^{88/86}Sr$ composition were all distinguishable from global riverine values. This difference was interpreted as an indication of the disproportionate role that coastal geology plays on the chemical composition of groundwater discharge. In chapter 3, I constructed the most comprehensive chemical mixing model of the Fraser River to-date, where the [Li], [Mg], [SO_4], [K], [Ca], [Sr], $\delta^{7}Li$, $\delta^{26}Mg$, $\delta^{34}S$, $\delta^{41}K$, $\delta^{44}Ca$, $^{87}Sr/^{86}Sr$, and $\delta^{88/86}Sr$ composition of the dissolved load of the Fraser River was modeled and compared to observational data. The variations observed were consistent with (and able to be successfully modeled as) mixing between the hydrologic outputs of two end-member sources: young igneous rocks of the Coast Range and ancient (Paleozoic/Precambrian) metamorphosed sedimentary/carbonate bedrock of the Rocky Mountains. This result of Chapter 3 provides a first-order approximation of how these isotope systems may co-vary globally if surficial processes were to shift from a regime dominated by young, volcanic bedrock (e.g. trap volcanism) to a regime dominated by the erosion and weathering of collisional orogens dominated by ancient metasedimentary sequences (e.g. Himalayas).

Furthermore, I found $\delta^{7}Li$ to be the isotope system that correlated most significantly with silicate-derived cation fluxes ($R^2 = 0.2 – 0.4$), which contributes to the growing body of work suggesting it be a more direct silicate weathering proxy than $^{87}Sr/^{86}Sr$ (Misra and Froelich, 2012). In Chapter 4, I focused on constraining the cycling and export of one of these non-traditional isotopes, $\delta^{138}Ba$, in Gulf of Aqaba seawater. Hot and devoid of riverine inputs, the Gulf of Aqaba has the lowest saturation state for barite of any marine basin in the world (Monnin *et al.*, 1999), which I utilized as a modern analog for arid conditions of Earth's past. My results indicate that the $\delta^{138}Ba$ composition of the exported particulate flux does not vary with respect to regional parameters, such as barite saturation state and primary productivity. Furthermore, the results of this chapter bolster the argument that $\Delta^{138}Ba$, the isotopic offset between barite and seawater from which it precipitated ($\delta^{138}Ba_{particulate} - \delta^{138}Ba_{seawater}$), is consistently -0.47‰. Overall, in this thesis, I have improved constraints on the magnitude and isotopic composition of groundwater, riverine, and exported particulate fluxes for modern seawater.

Acknowledgements

Adina Paytan and Bernhard Peucker-Ehrenbrink supervised the research that forms the basis for the dissertation. Anton Eisenhauer, Ana Kolevica, Tristan Horner, Maureen Auro, John Higgins, Danielle Santiago Ramos, Nic Slater, Tomas Magna, Ondra Šebek Adi Torfstein, Barak Yarden, and Rob Franks provided laboratory and analytical guidance. I thank Aaron Beck, Henrietta Dulai, Isaac Santos, Claudia Benitez-Nelson, Willard Moore, Ashley Martin, and Herb Windom for providing access to the samples utilized in Chapter 2. Nils Moosdorf assisted with the global extrapolation necessary for Chapter 2. Collaborators at University of the Fraser Valley (Abbotsford, B.C., Canada), Bernhard Peucker-Ehrenbrink, and Britta Voss were responsible for sample collection used in Chapter 3. Adi Torfstein provided access to samples utilized in Chapter 4. Carolyn Brady and Frankie Lon were critical to sample preparation and laboratory assistance. Nemanja Komar and Dennis Zomar provided coding assistance for Chapters 2 and 3. I, Kimberley Bitterwolf, conceived these studies and drafted all parts of the manuscripts in Chapters 2, 3, and 4.

This compilation of work would not have been possible without all the support I have received over the years – I am grateful for all of it – but first, I would like to thank my committee. Thank you, Adina Paytan, for setting me up with this opportunity, investing in me, being my advocate, going above and beyond when I needed it, helping me through this entire process, and constantly assuring me that everything will turn out fine. Thank you, Bernhard Peucker-Ehrenbrink, for fostering the confidence of a young undergraduate early on in her STEM career – without your encouragement, I would never even have dared to apply to graduate school to earn a Ph.D. Furthermore, despite not actually being a WHOI student, you ensured that I never lost the feeling of home there and that you remained an attentive Ph.D. advisor, regardless of our time difference! Christina Ravelo and Carl Lamborg, thank you for agreeing to be on a committee for a dissertation that, I will admit, doesn't utilize very much seawater or marine sedimentary data. You both approached my thesis research with open minds, provided thoughtful guidance regarding how these chapter results will be applied in studies to come, and fully engaged in your role as committee members when called upon. Anton

Eisenhauer, Tristan Horner, John Higgins, Tomas Magna, and Adi Torfstein, thank you for letting me use your lab spaces and equipment, for walking me through laboratory procedures, for answering all my questions, your guidance through my first publication, and for so many thoughtful contributions to my work. Your generosity with your time and facilities has been tremendous. Carolyn Brady, thank you for all those long days, nights, and weekends in the lab – cleaning Teflon, preparing and shipping samples, pipetting for hours, and keeping my spirits up. Thank you to Rob Franks and Brian Dreyer for your assistance in the Marine Analytical Lab and clean lab at UCSC.

Thank you to all the funding sources that made this work possible. This material is based upon work supported by the National Science Foundation Graduate Research Fellowship Program, two internships provided through the Graduate Research Internship Program (GRIP), an internship provided through the NSF INTERN program, and a supplement to Adina Paytan's previously existing NSF research grant that funded the participation in the European Research Commission's Horizon 2020 Marie Curie International Training Network – BaseLine Earth. This work was also supported by grants from: the German Academic Exchange Service, Northern California Chapter of the Achievement Rewards for College Scientists Foundation, UCSC President's Dissertation Fellowship, International Association of GeoChemistry, Geological Society of America, Northern California Geological Society, Myers Trust, Friends of Long Marine Lab, UCSC Graduate Student Association, and UC MEXUS.

I must also thank Lezlie Ward and Rondi Robison, the Ocean Science Department managers (past and present) for making sure everything ran smoothly from the moment I began this Ph.D. and for always looking out for me. They were there to make sure I didn't drop the ball and enthusiastically supported my ideas for the department. They are two of the most genuinely kind humans I have ever met and work so hard to make sure their students get the emotional, logistical, and financial support they need.

Thank you to my UCSC cohort, Caitlin Kroeger, Michelle Drake, Jessie Zupcic, Anna Lowe, Wilson Sauthoff, Dianna Baetscher, and Danielle Glynn for making my transition to Santa Cruz so smooth and being such an incredible support system through coursework and milestones. Your perseverance and support have been an incredible support over these many years. Thank you to the UCSC students outside of my cohort who helped me maintain my sanity through this process including: Kyle Broach (thank you for being the most incredible 'Travel Husband' ever) and Stephan Bitterwolf (thank you for your unwavering support and care over all the years). Colin Carney and Dana Shultz – thank you for helping me decompress when needed.

Thank you to my fellow labmates, past and present – I remember the day I arrived for prospective student week and was daunted by our sheer numbers, intimidated by the task of remembering so many names! However, not only do I remember all your names now, but your support and charisma are sealed into my memory into perpetuity. Carolyn Brady, Christina Richardson, Esra Mescioglu, Kyle Broach, Ana Martinez Fernandez, Joseph Murray, Chia-Te Chien, Pei Chuang, Karen Peterson, Delphine Deoffrey, Tracy Conrad, Michael Kong, Frankie Lon, Seth Williams, C.J Vigil, Ben Dejarnett, Maria Ferreira, Michael Taetzel, Susan Pit, and Madison Wood.

Thank to my extended Lab 'Ohana from all the institutions that I've had the privilege to work at. Julia Middleton, Jen Karolewski, Ann Dunlea, Logan Tegler, Jurek Bluzstajn, Peter Crockford, Dennis Mayk, and Laurenz Bo.

Thank to my friends and family who have been my unwavering cheerleaders from afar, who have unconditionally loved me through long absences in communication, and whom helped recharge my spirits when visits were possible: Christy Mayfield, Janet Mayfield, Jim Mayfield, Donna Goodwin, Katy Talvi, Walt McCoy, Susan Mayfield, Jenny Bernier, Augusto Callejas, and Austin Barnes. Also, Pawesome! You are the keeper of my sanity during so many long hours at the computer and the perfect distraction - you are my best friend, you force me to get up from the computer to walk

outside when I need it, make me laugh constantly, and your “woooooo”s are always perfectly timed. I am grateful to be able to call you all family.

And thank you to my ‘conference crews,’ who have made sure I never spent an awkward evening by myself during a conference and helped me navigate the mazes of AGU, Goldschmidt, OSM, ASLO, and ICP. You opened up your pre-formed geochemical family to me, even though I’m not ‘actually paleo.’ Richard Zeebe, James Zachos, Sambuddha Misra, Luc Lourens, Robin van der Ploeg, Rick Hennekam, Jessie Farmer, and Ann Dunlea.

To anyone else whom I’ve forgotten to thank who has provided guidance, advice, laughter, or kindness throughout this endeavor, you are in my heart, just currently not in my head because I have eight isotope systems in my head right now. Which reminds me, I owe the biggest thanks to my home island of Kaua`i, whose natural environment inspired me to pursue geoscience in the first place; it is the betterment of our environment and community that has kept me motivated amidst the challenges of pursuing a Ph.D. over the years.

Groundwater discharging to the ocean along a coastline in Hawai`i
Photo by Jenny Bernier.

***

ʻAʻohe pau ka ʻike i ka hālau hoʻokahi.

All knowledge is not learned in just one school

— ʻŌlelo No'eau, Hawaiian proverb

Dedication

This dissertation is dedicated to my family and chosen family, but especially to

***

Christy Mayfield

Christy, I wish you were here to see how it all turned out. You never cared too much about what it is I studied, as long as I was happy. You were always there to realign my priorities when I would overstress and be my biggest cheerleader when times were rough. You are my motivation for so many things and I see you in just about everything around me. Thank you for showing me how to practice kindness and compassion. You are my sister and my best friend, always, no matter the distance.

***

Chapter 1

Introduction

Elements with residence times longer than the mixing time of the ocean (>1000 years; e.g. Li, Mg, K, Ca, Sr, Ba) have oceanic distributions that are well mixed and, therefore, record global processes and leave records of isotopic variation in marine archives that are globally relevant (e.g. Broecker and Peng, 1982). Records of traditional stable (e.g. $\delta^{13}C$ and $\delta^{18}O$) and radiogenic (e.g. $^{87}Sr/^{86}Sr$) isotopes have been foundational to our understanding of Earth's biogeochemical evolution to date (e.g. Zachos *et al.*, 2001; Mcarthur *et al.*, 2016), but recent advancements in high-precision mass spectrometry now make possible the analysis of "non-traditional stable isotopes" in natural samples. This exciting new field, which includes $\delta^{7}Li$, $\delta^{26}Mg$, $\delta^{41}K$, $\delta^{44}Ca$, $\delta^{88/86}Sr$, and $\delta^{138}Ba$, makes possible the reconstruction of complementary records that will further detail our understanding of changes in global-scale processes of Earth's history, such as hydrology, silicate weathering, carbonate formation/dissolution, and oceanic circulation (Christina and DePaolo, 2000; Misra and Froelich, 2012; Higgins and Schrag, 2015; Geyman *et al.*, 2019). The paleoceanographic community is already active in reconstructing shifts in these isotope systems from marine archives over numerous geologic timescales (e.g. Cenozoic, Mesozoic, and Phanerozoic; Christina and DePaolo, 2000; Farkas *et al.*, 2007; Misra and Froelich, 2012; Vollstaedt *et al.*, 2014; Higgins and Schrag, 2015). However, in contrast to more traditional systems (e.g. $\delta^{13}C$, $\delta^{18}O$, and $^{87}Sr/^{86}Sr$), the isotope mass budgets of these elements are lacking in constraints for the inputs and output fluxes. Without accurate and well-understood marine isotope budgets, the utility of these exciting, new isotope systems is limited.

Dissertation Overview

The goal of this thesis is to provide further constraints on the non-traditional stable isotopic composition of two important inputs of solutes to the ocean (groundwater and river water) and one

important output (sedimentation). In CHAPTER 2, I calculate the magnitude and isotopic composition of a previously under-constrained, but important, flux of solutes to the global ocean: groundwater discharge. Utilizing the largest-ever amassed sample set of coastal groundwater samples and all available volumetric estimates of global groundwater discharge, I calculate the groundwater-derived fluxes of Li, Mg, Ca, Sr, and Ba to the global ocean, as well as the $\delta^{7}Li$, $\delta^{26}Mg$, $\delta^{44}Ca$, $^{87}Sr/^{86}Sr$, $\delta^{88/86}Sr$, and $\delta^{138}Ba$ compositions of this flux. This research has important implications for marine residence time estimates for these elements and their isotopic composition in seawater, as well as new proxy development and applications. In CHAPTER 3, I analyze $\delta^{7}Li$, $\delta^{26}Mg$, $\delta^{41}K$, $\delta^{44}Ca$, $^{87}Sr/^{86}Sr$, and $\delta^{88/86}Sr$ in the Fraser River (B.C., Canada), both the main stem and two gauging stations, intended to represent the two dominant geologic end-members contributing to the river's chemistry: the Coast Range and Rocky Mountains. Through the analysis and modeling of these isotope systematics in a time series on the Fraser River, I contribute to the growing body of work aimed at understanding how these isotope systems co-vary in the largest input flux for these elements: riverine discharge. Furthermore, by evaluating the co-variation of these isotopes in such a well-constrained river basin, I provide a first look into how these systems may co-evolve in riverine discharge and, consequently, seawater with changes in weathering provenance over time. In CHAPTER 4, I analyzed the $\delta^{138}Ba$ composition of seawater and suspended particulates in the water column from a time series in the Gulf of Aqaba. This study was intended to evaluate how the $\delta^{138}Ba$ composition of barite deposition (the largest Ba export flux from the ocean) may change with respect to environmental parameters, specifically primary productivity and barite saturation state. Combined, these chapters improve marine isotope budgets for these novel systems in the modern, which advances their oceanographic utility moving forward.

References

- Broecker, W. S. and Peng, T. H. (1982) *Tracers in the Sea, Lamont-Doherty Geological Observatory*. Palisades, New York.

- Farkas, J. *et al.* (2007) 'Calcium isotope record of Phanerozoic oceans: Implications for chemical evolution of seawater and its causative mechanisms', *Geochimica et Cosmochimica Acta*, 71(21), pp. 5117–5134.
- Geyman, B. M. *et al.* (2019) 'Barium in deep-sea bamboo corals: Phase associations, barium stable isotopes, & prospects for paleoceanography', *Earth and Planetary Science Letters*, 525, p. 115751.
- Higgins, J. A. and Schrag, D. P. (2015) 'The Mg isotopic composition of Cenozoic seawater - evidence for a link between Mg-clays, seawater Mg/Ca, and climate', *Earth and Planetary Science Letters*, 416, pp. 73–81.
- De La Rocha, C. L. and DePaolo, D. J. (2000) 'Isotopic evidence for variations in the marine calcium cycle over the Cenozoic', *Science*, 289(5482), pp. 1176–1178.
- Mcarthur, A. J. M. *et al.* (2001) 'Strontium Isotope Stratigraphy : LOWESS Version 3 : Best Fit to the Marine Sr - Isotope Curve for 0 – 509 Ma and Accompanying Look - up Table for Deriving Numerical Age', *Journal of Geology*, 109(2), pp. 155–170.
- Misra, S. and Froelich, P. N. (2012) 'Lithium isotope history of cenozoic seawater: Changes in silicate weathering and reverse weathering', *Science*, 335(6070), pp. 818–823.
- Vollstaedt, H. *et al.* (2014) 'The Phanerozoic $\delta^{88/86}$Sr record of seawater: New constraints on past changes in oceanic carbonate fluxes', *Geochimica et Cosmochimica Acta*, 128(May), pp. 249–265.
- Zachos, J. *et al.* (2001) 'Trends, rhythms, and aberrations in global climate 65 Ma to present', *Science*, 292(5517), pp. 686–693.

Chapter 2

The Importance of Groundwater Discharge in Marine Isotope Budgets of Li, Mg, Ca, Sr, and Ba

Abstract

Reconstructions of Earth's history rely on a detailed understanding of global climate-tectonic feedbacks. The effects of these feedbacks are integrated into continentally derived solute fluxes, for which rivers are considered the primary vector of transport. Groundwater discharge to the ocean has long been assumed static and subordinate to the riverine flux, if not neglected entirely, in marine isotope budgets. Here I present concentration and isotope data for Li, Mg, Ca, Sr, and Ba in coastal groundwaters to constrain the role of groundwater discharge in the magnitude and isotopic composition of their continentally derived solute fluxes. Concentration and isotope data were extrapolated globally using three volumetric estimates of global groundwater discharge, from which I estimate that groundwater discharge contributes, at the minimum, 5% of riverine fluxes for Li, Mg, Ca, Sr, and Ba to the ocean. The isotopic compositions of groundwater-derived Mg, Ca, and Sr are distinct from average riverine inputs, demonstrating a strong dependence on coastal lithology. Such dependence is not evident in this study for Li or Ba isotopes, which are indistinguishable from riverine values. These results imply that, globally, groundwater discharge may be a hitherto under-constrained conduit for weathering products, but the broad range of fluxes determined using available global groundwater discharge models emphasizes the need for more precise volumetric estimates.

Introduction

In this study, I define groundwater discharge as the flow of meteoric waters directly from aquifers to the coastal ocean. Globally, groundwater-derived solute fluxes, relative to riverine-derived fluxes, have been difficult to constrain due to large uncertainties in the volumetric flux, significant quantities of recirculated seawater, and chemical heterogeneity within—and between—aquifers. Volumetric fluxes of global groundwater discharge vary by an order of magnitude, ranging from 286 – 2,400 $km^3\ a^{-1}$, or 0.7 – 6% of the riverine flux (Zektser, 2006; Beck *et al.*, 2013; Peucker-Ehrenbrink, 2018; Zhou *et al.*, 2019; Luijendijk, *et al.*, 2020). Despite this large uncertainty, however, several studies have attempted to constrain the magnitude and isotopic composition of groundwater-derived solute fluxes to the ocean using available data from local studies of groundwater chemistry (Johannesson and Burdige, 2007; Beck *et al.*, 2013; Cho *et al.*, 2018; Rahman *et al.*, 2019; Luijendijk et al., 2020; Zhang and Planavsky, 2020). These studies found that groundwater discharge may significantly impact the residence times of important nutrients in the ocean (e.g. N, P, and Si) (Cho *et al.*, 2018; Rahman *et al.*, 2019; Luijendijk *et al.*, 2020), serve as a net carbon sink in short- and long-term carbon cycles (Zhang and Planavsky, 2020), and that its globally-averaged isotopic composition can differ from riverine discharge (e.g. Sr and Nd) (Johannesson and Burdige, 2007; Beck *et al.*, 2013). Quantifying and characterizing this continentally derived solute flux is central to our understanding of the sensitivity and interpretation of numerous oceanographic tracers.

In this study, I measured the concentration and isotopic compositions of a suite of elements – selected because of their ability to inform on aspects of tectonics, weathering, and biogeochemistry – in a globally distributed set of groundwater samples. Samples were opportunistically compiled from previous studies to assemble the most globally representative sample set available without necessitating additional field work (Fig. 1; Fig. 2; Table 1). Sample distribution is not representative of all global settings as groundwater sampling campaigns were not carried out evenly throughout the world (e.g. affluent regions are overrepresented while developing regions, such as Indonesia and western Africa, have not been adequately sampled, although they may be important). Despite these

limitations, however, the assembled data included aquifers from different geologic substrates (Table S1), which is important when extrapolating globally with lithologically weighted models of groundwater discharge (Beck *et al.*, 2013; Luijendijk et al., 2020). I use the results from these aquifers to provide new estimates of the magnitude and isotopic composition of groundwater-derived fluxes for major (Mg and Ca) and minor (Li, Ba, and Sr) cations to the ocean, as well as elucidate needs for future research. The $\delta^{7}Li$, $\delta^{26}Mg$, $\delta^{44/42}Ca$, $^{87}Sr/^{86}Sr$, $\delta^{88/86}Sr$, and $\delta^{138}Ba$ systems were selected for their roles as major components (Ca and Mg) or minor element proxies (Li, Sr, and Ba) of weathering and long-term carbon cycling (Misra and Froelich, 2012; Vollstaedt *et al.*, 2014; Horner, *et al.*, 2015). Recent models of global weatherability emphasize the importance of silicate weathering in humid, low-latitude, tectonically-active regions (Rad, Allègre and Louvat, 2007; Macdonald *et al.*, 2019) – the same regions modeled to host the majority (55 - 68%) of global groundwater discharge (Beck *et al.*, 2013; Zhou *et al.*, 2019; Luijendijk et al., 2020). This spatial overlap suggests that groundwater discharge may play an outsized role in silicate weathering and the regulation of atmospheric CO_2 on geologic timescales.

To test the hypothesis that, globally, groundwater discharge is a non-negligible source of Li, Mg, Ca, Sr, and Ba to the ocean and that its isotopic composition is distinct from riverine values, I analyzed groundwater from 20 subterranean estuaries, in addition to incorporating previously published data from other coastlines (Hogan and Blum, 2003; Holmden *et al.*, 2012; Beck *et al.*, 2013) (Fig. 2). Subterranean estuaries are the coastal extent of aquifers, where seawater mixes with meteoric groundwater (Moore, 1999), facilitating the collection of samples that span the full range of salinities, from fresh groundwater to coastal seawater (Fig. 1; Fig. 2; Fig. 3). To assess how concentrations and isotopic compositions of these elements vary with respect to lithology, each subterranean estuary was characterized according to local geology into one of four 'aquifer types,' including extrusive igneous, carbonate, intrusive igneous, and sedimentary (Fig. 2; Table 1). Elemental concentrations across the salinity gradient of the subterranean estuary were evaluated for conservative vs non-conservative behavior. The behaviors of Li, Mg, Ca, and Sr concentrations were conservative (Fig. 3, R^2 values of linear trendlines across salinity gradients were >0.6; Table 2) and, thus, their freshwater endmember

concentrations were estimated to equal the intercept of linear regressions with salinity for each 'aquifer type.' By using the intercept, which represents cation concentrations at a salinity of 0, I avoid overestimating the solute concentrations in fresh groundwater discharge due to recirculating seawater, whose influence is not within the scope of this study. Barium exhibited non-conservative behavior in this dataset, with maximum Ba concentrations ($[Ba]_{max}$) occurring at intermediate salinities, consistent with the expected mid-salinity desorption maxima of Ba in subterranean and riverine estuaries (Fig. 3) (Edmond *et al.*, 1985; Santos *et al.*, 2011). The $[Ba]_{max}$ concentration for each aquifer was used to represent the groundwater endmember, since desorbed Ba from coastal sediments is indeed a new (i.e. non-recirculated) source of Ba to the ocean, indicating that the $[Ba]_{max}$ value more accurately represents the concentration in the groundwater as it discharges to the ocean. Using the freshwater endmember, derived from the intercept, would have underestimated the groundwater-derived Ba flux. Thus, the Ba concentration in the groundwater endmember was estimated to equal the average of $[Ba]_{max}$ samples within each 'aquifer type' (Table 2).

The $\delta^{7}Li$, $\delta^{26}Mg$, $\delta^{44/42}Ca$, $^{87}Sr/^{86}Sr$, and $\delta^{88/86}Sr$ compositions of each 'aquifer type' endmember were calculated as the average of the values from the lowest salinity samples in each aquifer, provided that the sample had a salinity < 2 (Fig. 4; Table 3). Using only isotopic compositions of low-salinity samples reduced the likelihood of unintentionally incorporating values influenced by recirculated seawater into the groundwater flux characterization. The $\delta^{138}Ba$ composition of each 'aquifer type' was calculated as the average of the values from each of the $[Ba]_{max}$ samples (Fig. 4; Table 3). Since little is known about the role that desorption from coastal sediments plays in Ba isotope fractionation, it was prudent to only use the isotope values of the samples from which the cation flux was derived.

In the two global groundwater discharge models with lithologic weighting Beck *et al.* (2013) and Luijendijk *et al*. (2020), there are instances when the local geology of aquifers is wholly or partially unconstrained, which they respectively refer to as 'complex' and 'no lithology.' Since this unconstrained 'aquifer type' is responsible for 37% (Beck *et al.*, 2013) and 10% (Luijendijk *et al.,* 2020) of the global volumetric fluxes presented in the models, it was necessary to estimate a chemical

composition for this endmember. Therefore, I designed a fifth 'no lithology' aquifer type, whose elemental concentration was equal to the average of the other four lithologic 'aquifer types' and whose isotopic composition was calculated via a concentration-weighted average of the other four 'aquifer types' (Fig. 2; Table 5).

Global groundwater-derived solute fluxes were calculated by feeding the chemical compositions of these five 'aquifer type' endmembers into three models of volumetric groundwater discharge (Beck *et al.*, 2013; Zhou *et al.*, 2019; Luijendijk, *et al.*, 2020). Two of the models were lithologically weighted (Beck *et al.*, 2013; Luijendijk *et al.*, 2020); specifically, volumetric flux values per each groundwater flux region had a distribution of lithology associated with it (e.g. 40% carbonate, 60% sedimentary, etc.). Thus, the resultant flux from that region would have a chemical composition equal to the proportionate mixture of elemental concentrations and isotope ratios from those 'aquifer type' endmembers characterized in this study.

Materials and Methods

Dataset Sources

Samples were opportunistically amassed from groundwater researchers worldwide (Supplementary Information, Table S1). In the field, these samples were collected using traditional groundwater-sampling techniques – namely, digging pits or inserting piezometers into beach faces perpendicular to the shoreline to obtain a salinity-gradient: from fresh, meteoric groundwater to local coastal seawater (Fig. 1). Post-collection, samples were filtered through either 0.2 or 0.45 μm filters and acidified. Samples were in storage for anywhere between 9 years to a few weeks before analyses. Given the consistency of cation concentrations in the samples independent of storage time and the order-of-magnitude variability in the model outputs when extrapolating the data globally, evaporation during storage was considered negligible.

Due to the opportunistic nature of this sampling, sub-categories within each lithologic 'aquifer type' are not evenly represented. For example, the extrusive igneous category is comprised

predominantly of samples representing young geologies (e.g. Hawai`i and Mauritius), while groundwater samples from older extrusive igneous formations (e.g. the Deccan Trap region) are not represented. This may have influenced the representativeness of the dataset; for example, the $^{87}Sr/^{86}Sr$ composition calculated for the extrusive igneous member might be more radiogenic than calculated here. Most importantly, vast regions responsible for a large portion of the global groundwater flux, such as Indonesia and western Africa, were not be sampled for groundwater discharge. However, I argue that it is coastal carbonate deposits that are driving the other isotopic differences observed between groundwater and riverine discharge, globally, and that these are well-characterized by this study, since all coastal carbonate deposits should be relatively recent in age. Of course, improvements to the globally representative nature of this sample set are desired.

Historical Data Incorporation

Previously published data from other coastal aquifers/subterranean estuaries that included at least one of the isotope systems relevant to this study were included in the meteoric groundwater endmember calculations (Table 1) (Hogan and Blum, 2003; Holmden *et al.*, 2012; Beck *et al.*, 2013). Data from non-coastal aquifers were not included because the focus of this study was specifically to examine the groundwater-derived solute flux to the ocean and it is unclear if and how much transformation these constituents experience in the aquifer before reaching the coast. Thus, to ensure that data represent the solute load transported to the coast, only coastal groundwater samples and data from coastal subterranean estuaries were included.

Chemical Analyses

Dissolved concentrations of Li, Mg, Ca, Sr, and Ba were analyzed at the University of California, Santa Cruz using a Thermo Scientific™ Element XR™ inductively coupled plasma mass spectrometer (ICP-MS). Subsampling and subsequent analyses of dissolved concentrations to ensure reproducibility were performed at the Woods Hole Oceanographic Institute and Czech Geological Survey with a Thermo Scientific iCAP Qc quadrupole ICP-MS and Agilent 5110 ICP-optical emission

spectrometer, respectively. δ^{7}Li, δ^{26}Mg, $\delta^{44/42}$Ca, and $\delta^{138/134}$Ba data were collected using a Thermo Scientific™ Neptune™ multi-collector ICP-MS at the Czech Geological Survey, Princeton University, GEOMAR Helmholtz Center for Ocean Research, and Woods Hole Oceanographic Institution, respectively. $^{87}Sr/^{86}Sr$ and $\delta^{88/86}$Sr data were collected via thermal ionization mass spectrometry at GEOMAR. All isotope data, except $^{87}Sr/^{86}Sr$, are reported in per-mil (‰) relative to the corresponding reference materials using standard delta (δ) notation. Additional information on technical aspects of the analyses can be found below.

Li Isotope Analyses

Lithium analytical procedures and isotopic measurements were performed at the CGS using a method developed by Magna, et al. (2004), which involves ion-exchange chromatography with BioRad™ AG-50W-X8 cation exchange resin (repeated twice), followed by Li isotope analysis using a Neptune multi-collector inductively-coupled-plasma mass spectrometer (MC-ICP-MS; Thermo Scientific™). A sample-standard bracketing method using L-SVEC solution was utilized to determine natural Li isotopic variations in the groundwater samples. The results of Li isotopic measurements are reported in the δ-notation relative to the L-SVEC reference solution (Flesch, Anderson and Svec, 1973) and calculated as:

$$\delta^{7}\text{Li (‰)} = [(^{7}\text{Li}/^{6}\text{Li})_{\text{sample}} / (^{7}\text{Li}/^{6}\text{Li})_{\text{L–SVEC}} - 1] \times 1000$$

Four different reference materials were repeatedly analyzed alongside samples to monitor the consistency of the entire procedure: IAPSO (OSIL seawater; 30.85‰ ± 0.18; n = 4), NASS-6 (seawater; NIST) (30.78‰ ± 0.08; n = 3), NIST 1640a (river water; NIST) (16.76‰ ± 0.08; n = 4), and SLRS-5 (river water; NRC) (23.58‰ ± 0.33; n = 3), where the uncertainty represents 2SD. The resultant δ^{7}Li values for the standards fell within the range of previously published values available on GeoRem (Jochum *et al.*, 2005) and their reproducibility between runs (± ≤ 0.33‰; 2SD) was approximately equal to the uncertainty associated with their individual analyses (0.07 – 0.54‰). All analytical results for the δ^{7}Li composition of groundwater samples are in Table 3.

Mg Isotope Analyses

Magnesium isotopic compositions were measured at Princeton University using a method developed by Blättler et al. (2015), which involves automated, high pressure ion-exchange chromatography with a Dionex ICS-5000+ IC system, coupled with a Dionex AS-AP fraction collector, followed by Mg isotope analysis with a Neptune MC-ICP-MS (Thermo Scientific™). A sample-standard bracketing method using DSM-3 solution (Galy *et al.*, 2003) was utilized to determine natural Mg isotopic variations in the groundwater samples. The results of Mg isotopic measurements are reported in δ-notation relative to the DSM-3 reference solution and calculated as:

$$\delta^{x}\text{Mg (‰)} = [(^{x}\text{Mg}/^{24}\text{Mg})_{\text{sample}} / (^{x}\text{Mg}/^{24}\text{Mg})_{\text{DSM-3}} - 1] \times 1000$$

where the 'x' denotes 26 or 25, respectively.

To ensure that the separation procedure did not fractionate Mg, I processed standards alongside unknowns. Measured δ^{25}Mg and δ^{26}Mg compositions for IC-purified Cambridge-1 (δ^{25}Mg = -1.35 ±0.10‰; δ^{26}Mg = -2.62 ±0.13‰; 2, n=13) and Bermuda seawater (δ^{25}Mg = -0.45 ±0.09‰; δ^{26}Mg = -0.84 ±0.12‰; 2σ, n=13) standards are indistinguishable from published values (Galy *et al.*, 2003), attesting to the efficacy of this chemical purification protocol. All analytical results for the δ^{26}Mg composition of groundwater samples are provided in Table 3. For replicated samples (chemical purification + mass spectrometry), I report the 2σ error on the sample average; otherwise, reported errors correspond to long-term external precision on the Cambridge-1 standard at Princeton (0.09‰, 2σ, n=79; Blattler *et al.,* 2015).

Ca Isotope Analyses

Calcium isotopic compositions were measured at GEOMAR Helmholtz Center for Ocean Research (Kiel, Germany). Chemical separation of Ca from the matrix was conducted using an automated, commercially-available Prep*FAST* MC (ESI, Omaha, NE, USA) according to the method developed by Romaniello et al. (2015). The $\delta^{44/42}$Ca analyses were conducted on a Neptune™ MC-ICP-MS (Thermo Scientific™) with a method adapted from Eisenhauer et al. (2019), which utilizes a sample-standard bracketing technique using SRM-915a solution (Coplen *et al.*, 2002) to determine natural Ca isotopic variations.

$$\delta^{44/42}Ca\ (‰) = [(^{44/42}Ca/^{44/42}Ca)_{sample} / (^{44/42}Ca/^{44/42}Ca)_{SRM\text{-}915a} - 1] \times 1000$$

Three different reference materials were separated and analyzed alongside samples to monitor the consistency of the entire procedure: IAPSO (seawater; OSIL), SRM-915b (calcium carbonate; NIST), and SRM-1486 (bone meal; NIST). The resultant $\delta^{44/42}Ca$ values (+0.90‰, +0.35‰, and -0.50‰, respectively) are in good agreement with previously published values available on GeoRem (Jochum *et al.*, 2005) and their long-term reproducibility (± 2 SD) is equal to 0.08‰ (IAPSO, n = 135), 0.10‰ (SRM-915b, n = 15), and 0.05‰ (SRM-1486, n = 172). All analytical results for the $\delta^{44/42}Ca$ composition of groundwater samples are provided in Table 3. For ease of comparison with other previously published datasets, a conversion calculation to $\delta^{44/40}Ca$ is provided, based on a conversion factor from Gussone et al., 2016 (Gussone *et al.*, 2016), which assumes a kinetic fractionation coefficient of 2.05, where $\delta^{44/40}Ca = \delta^{44/42}Ca \times 2.05$.

Sr Isotope Analyses

Groundwater Sr isotopic compositions were measured at GEOMAR Helmholtz Center for Ocean Research (Kiel, Germany) using a method developed by Krabbenhöft *et al.*, (2009), which involves the chemical separation of every sample twice, once 'spiked' using a custom double spike and once 'unspiked.' Ion-exchange chromatography was conducted using Eichrom Sr Spec resin in BioRad™ micro bio-spin™ columns, followed by Sr ($\delta^{88/86}Sr$ and $^{87}Sr/^{86}Sr$) isotope analysis using a TRITON thermal ionization mass spectrometer (TIMS) (ThermoFisher, Bremen, Germany). The results of the $\delta^{88/86}Sr$ measurements are reported in δ-notation relative to the SRM-987 reference standard and calculated as:

$$\delta^{88/86}Sr\ (‰) = [(^{88}Sr/^{86}Sr)_{sample} / (^{88}Sr/^{86}Sr)_{SRM\text{-}987} - 1] \times 1000$$

To correct for session-to-session variations in isotopic ratios, 3 'spiked' and 2 'unspiked' SRM-987 analyses were conducted during each session – alongside every 8 samples. The average measured value of these SRM-987 analyses were compared to their accepted values ($^{88/86}Sr = 8.375209$ ($\delta^{88/86}Sr = 0$) and $^{87}Sr/^{86}Sr = 0.710240$) to calculate a correction factor for the session. This correction factor was applied to each sample, resulting in session-corrected values. Reported in Krabbenhöft et al. (2009), the long-term $\delta^{88/86}Sr$ reproducibility of SRM-987 with this method and instrumentation is

0.012 ± 0.044 (2 SD). All analytical results for the $\delta^{88/86}Sr$ and $^{87}Sr/^{86}Sr$ composition of groundwater samples are provided in Table 3.

Ba Isotope Analyses

Groundwater samples were prepared and measured for their Ba isotopic compositions at the NIRVANA Labs at Woods Hole Oceanographic Institution (WHOI) using the method described by Bates et al. (2017). Samples were spiked with an appropriate quantity of ^{135}Ba–^{136}Ba double spike so as to achieve a spike- to sample-derived Ba molar ratio of between 1–2. Samples with salinity >5 were co-precipitated via dropwise addition of Ba-free 1 M Na_2CO_3 solution. The resultant precipitate was dissolved in 6 M HCl and evaporated to dryness, before reconstituting in 250 µL of 2 M HCl. Samples with salinity < 5 were evaporated and reconstituted in 250 µL of 2 M HCl. Following reconstitution, all samples were twice passed through columns containing 500 µL of AG 50W-X8 resin that were precleaned of Ba with 6 M HCl. Following matrix elution (in 2 M HCl), Ba was eluted (and REE retained) with 2 M HNO_3. The resin was discarded after use. Purified samples were evaporated and reconstituted in 0.5 M HNO_3 to achieve a sample-derived [Ba] of ≈ 20 ng mL^{-1}.

Analyses were conducted at the WHOI Plasma Facility using a Thermo Finnigan Neptune MC-ICP-MS, operated in low resolution mode. Samples were aspirated, desolvated, and introduced into the mass spectrometer using a PFA nebulizer (at a rate of ≈140 µL min^{-1}), CETAC Aridus II, and as an aerosol in ~1 L Ar min^{-1} containing 3–5 mL min^{-1} admixed N_2, respectively. Samples were analyzed in 30–40 × ≈4.2 s integrations a minimum of two times, up to a maximum of eight. Spiked aliquots of NIST SRM 3104a were measured every fifth analysis; the spike-to-sample ratio of NIST SRM 3104a was adjusted to match bracketing samples and isotopic data reported relative to the nearest four bracketing standards using the δ notation:

$\delta^{138/134}Ba$ (‰) = $[(^{138}Ba/^{134}Ba)_{sample} / (^{138}Ba/^{134}Ba)_{SRM\text{-}3104a} - 1]$. Results for groundwater samples are provided in Table 3.

Analytical precision is reported as the greater of either long-term 2 SD reproducibility (± 0.03 ‰; Horner et al., 2015) or the measured 2 SE obtained from replicate analyses (i.e., where *n* was between 2–8). Accuracy was monitored by processing four aliquots of GEOTRACES SAFe D1

alongside sample unknowns; two aliquots were processed from bottle #591 and two from #596, yielding mean [Ba] and δ^{138}Ba of 99.0±2.5 nmol kg^{-1} and +0.33±0.03 ‰, and 99.4±2.5 nmol kg^{-1} and +0.33±0.03 ‰, respectively. Results from both bottles are in agreement with previous measurements of SAFe D1 from the NIRVANA Labs (98.7±2.5 nmol kg^{-1} and +0.31±0.03 ‰; Geyman et al., 2019) and elsewhere (99.6 nmol kg^{-1} and +0.27±0.02 ‰; Hsieh and Henderson, 2017).

Geologic 'Aquifer Type' Characterizations

Five geologic 'aquifer types' were designed for use in the geologically weighted groundwater discharge models. These types were: extrusive igneous, intrusive igneous, carbonate, sedimentary, and 'no lithology.' Individual aquifers (n = 27) were categorized into one of these four geologic 'aquifer types' and these categorizations are listed in Table 2. These categorizations were assigned based on descriptions of local geology from the papers that conducted the initially sampling/study or, for uncommon instances where geology was not defined in the sampling, regional maps of geology were used.

Global Extrapolation

The results of this geochemical survey of coastal groundwaters were extrapolated globally using three volumetric groundwater fluxes Beck et al. (2013), Zhou et al. (2019), and Luijendijk et al. (2020).

Beck et al., 2013 Model

The model developed by Beck et al. (2013) is based upon the volumetric groundwater fluxes of Zektser (2006) and the geologic map of Gibbs and Kump (1994). This Zektser model delineates 118 'groundwater regions,' for which volumetric fluxes of groundwater are calculated. This volumetric model was adapted by Beck et al. (2013) to include lithologic weighting by overlaying a coarse (2° x 2°) geologic map by Gibbs and Kump, (1994). In the Beck et al. (2013) model, there was an additional 'aquifer type' for slate lithologies that was removed in this study due to a lack of samples derived from slate-dominated aquifers. Before the addition of this new data, however, the slate aquifer endmember

was removed and there was no change to the resultant Sr flux or isotopic composition calculated with the data from Beck *et al.* (2013). I adapted the model, however, to include solute flux-weighting to the isotopic composition of the global output.

In the original model, an unweighted average Sr concentration ([Sr]) and $^{87}Sr/^{86}Sr$ value was used for the composition of all 118 'groundwater regions.' However, in this study, the elemental flux (i.e. concentration * annual groundwater flux) for each of the 118 'groundwater regions' was used to calculate the isotopic composition of the global groundwater-derived solute fluxes. The calculations were as follows:

1. Calculate annual solute fluxes (f_n) for each of the 118 groundwater regions:

$$f_n = ([X]_n * Q_n)$$

where $[X]_n$ refers to the solute concentration in a 'groundwater region,' which is dictated by local geology, and Q_n refers to the volumetric discharge of groundwater from that region.

2. Calculate % of global groundwater-derived flux for each 'groundwater region' (p):

$$\mathrm{p_n} = \frac{\mathrm{f_n}}{\sum_{\mathrm{i=1}}^{118} \mathrm{f_i}}$$

where the flux (*f*) from an individual groundwater region (*n*) is divided by the summation of fluxes from all 118 global 'groundwater regions.'

3. Calculate solute concentrations for global groundwater discharge ($Groundwater_{avg}[X]$):

$$Groundwater_{avg}[X] = \sum_{i=1}^{118} p_i * [X]_i$$

where $[X]_i$ represents the solute concentration for each aquifer.

4. Calculate isotopic compositions for global groundwater discharge ($Groundwater_{avg}\delta X$):

$$\mathrm{Groundwater}_{avg}\delta X = \frac{\sum_{m=1}^{118} \delta X_m * f_m}{\sum_{i=1}^{118} f_i}$$

where δX_m represents the isotopic composition of a solute for global groundwater discharge, f_i denotes the solute flux from each 'groundwater region,' and f_m is the global solute flux, namely:

$Groundwater_{avg}[X]$ multiplied by the volumetric estimate of global groundwater discharge from each model.

This change to the calculation of the chemical composition of global groundwater discharge only resulted in a small difference relative to the original model (Beck *et al.*, 2013) in the final output. For example, the Li concentration changed from 1.6 to 1.8 μM and δ^7Li changed from 24.0‰ to 23.1‰. These latter values (1.8 μM and 23.1‰), however, are more representative of the chemical composition of the global groundwater flux than the unweighted average because this solute flux-weighting approach corrects for the inequitable influence that regions responsible for only a small fraction of global groundwater discharge were having on the calculation of global groundwater chemistry. For example, in the original model, the chemical composition of Jamaica (a 'groundwater region' responsible for only 0.02% of the global volumetric flux and 0.04% of the global Ca flux) had the same impact on the global groundwater Ca isotopic composition as more voluminous 'groundwater regions' that are responsible for a greater portion of the global groundwater-derived Ca flux (e.g. New Guinea, which is responsible for 11% of the global volumetric flux and 4% of the groundwater-derived Ca flux). With this update to the model, each of these 118 'groundwater regions' are not weighted equally to one another in the calculation of global groundwater chemistry, but rather were considered in proportion to their volumetric and solute fluxes.

Luijendijk et al., 2020 Model

This volumetric model of global groundwater discharge integrates the watershed geometry, topographic gradients, permeability, and groundwater recharge of 39,858 coastal watersheds to construct one, global-scale groundwater flux. Lithologic weighting is integrated in this model as 17 different lithologic groupings derived from the GLiM geologic map (Hartmann and Moosdorf, 2012). Without the ability to characterize the chemical composition of 17 distinct lithologic 'aquifer type' endmembers in this study, these 17 lithologies were binned into the same five 'aquifer types' shared by Beck et al. (2013) – namely, extrusive igneous, intrusive igneous, carbonate, sedimentary, and 'no lithology' (Table 3). The relative abundance of each lithology within each 'groundwater region,' however, was far more precise in this model. Beck et al. (2013) estimated watershed geologic make-up

as a binary combination (i.e. present vs. absent) of each lithology (e.g. an aquifer with carbonates, granites, and sedimentary rocks would always be represented by a 33.3% share of each – additional precision was not resolved). This model utilized a higher-resolution geologic map (Hartmann and Moosdorf, 2012), which yielded a higher-resolution estimation of watershed geology.

Zhou et al., 2019 Model

This volumetric model of global groundwater fluxes is based on continental-scale hydrographic and climate datasets from NASA, spanning 60°N to 60°S. However, no lithologic weighting was considered in this model. In lieu of lithologic weighting, I opted to take the average of the final chemical compositions of global groundwater discharge calculated via the geologic weighting in the other two models: Beck et al. (2013) and Luijendijk et al. (2020) and simply multiply by the Zhou et al. (2019) flux.

Results and Discussion

Since the global volumetric groundwater flux estimates of the models used for extrapolation in this study span from 286 – 2,400 $km^3\ a^{-1}$, or 0.7 – 6% of the riverine flux (Zektser, 2006; Beck *et al.*, 2013; Peucker-Ehrenbrink, 2018; Zhou *et al.*, 2019; Luijendijk et al., 2020), the resultant solute fluxes span a similarly large range (Table 6). For example, in the case of Ba, the groundwater-derived solute flux ranges from 0.42 – 3.72 Gmoles a^{-1}, which corresponds to 5 – 45% of the riverine flux (Table 6). Groundwater-derived flux estimates for Li, Mg, Ca, and Sr are similarly broad ranging, spanning an order of magnitude (Table 6).

Of the three global groundwater flux models used in this study, the two published most recently (Zhou *et al.*, 2019; Luijendijk *et al*., 2020) agreed more closely with one another than that used by Beck *et al.*, (2013), yet there was still almost a two-fold difference (286 vs. 489 $km^3\ a^{-1}$) difference between even these models. I recognize that the range in global estimates of groundwater discharge is currently limiting my ability to precisely estimate associated solute fluxes. However, data

reported here could be used to update estimates as new and improved models become available. In addition, new chemical data collected from subterranean estuaries in under sampled regions, particularly in tropical climates with high rates of groundwater discharge, would help to better constrain the endmember concentrations and isotope ratios used in this study.

Relative to the magnitude of groundwater-derived solute flux estimates, the isotopic compositions of these fluxes were in closer agreement. They were calculated as the average of the two model outputs for which lithologic weighting was available (Beck *et al.*, 2013; Luijendijk *et al.*, 2020). This resulted in the isotopic compositions of modern global groundwater discharge to be determined as 22.3 ± 0.7‰ (δ^{7}Li), −1.40 ± 0.1‰ (δ^{26}Mg), 0.53 ± 0.08‰ ($\delta^{44/42}$Ca), 0.70878 ± 0.00005 ($^{87}Sr/^{86}Sr$), 0.292 ± 0.01‰ ($\delta^{88/86}$Sr), and 0.12 ± 0.03‰ (δ^{138}Ba), where ± values represent the greater of model output ranges or long-term analytical uncertainty (Table 6). The δ^{7}Li and δ^{138}Ba compositions of the global groundwater flux to the ocean, based on this data and model results, are nearly identical to riverine values (Misra and Froelich, 2012; Cao *et al.*, 2016) (Table 1). However, the δ^{26}Mg, $\delta^{44/42}$Ca, $\delta^{88/86}$Sr, and $^{87}Sr/^{86}Sr$ values are distinct from average riverine compositions (Tipper *et al.*, 2006; Fantle and Tipper, 2014; Peucker-Ehrenbrink and Fiske, 2019) (Table 6).

The global groundwater fluxes of the suite of elements reported here and the isotopic composition of these fluxes heavily depend on the distribution of coastal lithology in the models and the data obtained from each of these distinct settings. All estimates of global groundwater discharge agree that the majority (55 – 68%) of discharge is derived from tectonically-active, tropical regions (Beck *et al.*, 2013; Zhou *et al.*, 2019; Luijendijk *et al.*, 2020), which are typically characterized by young volcanic rocks and coastal carbonate deposits, hence skewing the global average towards these lithologies. The global riverine flux, in contrast, is more evenly distributed latitudinally and the chemistry of river discharge is more representative of the average exposure of different rock types on land (Peucker-Ehrenbrink and Fiske, 2019).

I argue that this is the cause of the observed differences (Sr, Ca, Mg) or similarities (Li, Ba) calculated between riverine and groundwater-derived solute fluxes. The dominance of young volcanic rocks and recent carbonate deposits (e.g. paleo-reefs) in low latitude areas with high groundwater

discharge contribute to the less radiogenic $^{87}Sr/^{86}Sr$ composition of the global groundwater flux, relative to riverine discharge. This finding is consistent with a previous assessment of global groundwater $^{87}Sr/^{86}Sr$ composition (Beck *et al.*, 2013) and *in situ* investigations of groundwater-derived Sr fluxes (Rad, Allègre and Louvat, 2007; Allègre *et al.*, 2010) from these regions. In addition to a less radiogenic $^{87}Sr/^{86}Sr$ composition, coastal carbonate deposits also have an abundance of Mg, Ca, and Sr with lower $\delta^{26}Mg$, $\delta^{44/42}Ca$, and $\delta^{88/86}Sr$ values, relative to seawater, as reflected in this data. The abundance of these coastal carbonate deposits in tropical regions disproportionally controls the $\delta^{26}Mg$, $\delta^{44/42}Ca$, and $\delta^{88/86}Sr$ signatures of global groundwater discharge, resulting in lighter signatures unique from riverine fluxes of these elements (Table 6).

I attribute the isotopic similarity between groundwater and riverine-derived fluxes of Li and Ba to inherent characteristics that make them less susceptible to differences in geologic age of substrate and coastal carbonate deposits. The $\delta^{7}Li$ composition of groundwater derived from young, tectonically active lithologies was found to be indistinguishable from that of older geologies (Table 5). Furthermore, since Li is not readily incorporated into carbonates and the $\delta^{7}Li$ composition of groundwater derived from carbonate aquifers was similar to that of igneous aquifers (Table 5), the abundance of coastal carbonate deposits in regions of high groundwater discharge had minimal impact on the $\delta^{7}Li$ composition of the global groundwater flux. The $\delta^{138}Ba$ composition of the global groundwater flux exhibited such a narrow range (0.14‰) across all lithologic 'aquifer type' endmembers that there was not enough variability in isotopic compositions to yield a geospatially driven offset from riverine values (Table 5). For example, the carbonate 'aquifer type' endmember was 0.09‰ and the extrusive igneous value was 0.18‰, which are encompassed by the riverine value of 0.2 ± 0.2‰ [20] and Bulk Silicate Earth (0.1 ± 0.1‰) (Charbonnier, *et al.*, 2018). This overlap suggests that there is likely minimal isotopic fractionation during the weathering of Ba from rocks.

These differences and similarities between riverine and groundwater discharge in solute composition should not be treated as static, however. I suggest that their solute fluxes may change over geologic timescales due to differing hydrologic controls on volumetric fluxes – namely, precipitation and changes in sea level (Stoll and Schrag, 1998; Krabbenhöft *et al.*, 2010), as well as changes in the

distribution of land masses and associated lithologies relative to climate regions. For example, during glacial periods, diminished precipitation would decrease riverine discharge (Gonneea, Mulligan and Charette, 2013), while falling sea levels would transitionally increase groundwater discharge and exposure of carbonate shelves (Stoll and Schrag, 1998; Krabbenhöft *et al.*, 2010; Vollstaedt *et al.*, 2014). These conditions should, consequently, increase the relative importance of groundwater-derived solute contributions globally and its associated isotopic signatures (Fig. 5).

Reconstructing changes to this terrestrial water flux (i.e. riverine + groundwater discharge), however, is a difficult task. Ba/Ca ratios in coastal carbonate deposits have been utilized with some success (Weldeab *et al.*, 2007), based on the premise that Ba concentrations of terrestrial water fluxes are high, which elevates the Ba/Ca ratio of local seawater, and results in a higher Ba/Ca ratio in coastal carbonate deposits. In coastal areas influenced by terrestrial water (riverine or groundwater), the Ba incorporated into these carbonate deposits should also have a lower δ^{138}Ba composition than that of seawater (+0.3 to +0.6‰) (Horner *et al*., 2015), more similar to the composition of meteoric waters found in this study and the global riverine average (≈ +0.1‰) (Cao *et al.*, 2016). This implies that Ba isotopes may have utility as a complementary paleo-proxy to Ba/Ca ratios for the reconstruction of terrestrial water input fluctuations in nearshore deposits to estimate changes in the relative influence of terrestrial water inputs over time.

Conclusions

It is clear from this study that groundwater-derived solute fluxes of Li, Mg, Ca, Sr, and Ba are of significance to marine isotope budgets, since solute fluxes account for at least 5% of the riverine input and the isotopic compositions of some of these solutes are distinct from those of riverine discharge. This additional solute flux will inherently impact conceptual models of these elements and their isotopic compositions in seawater, but also suggests potential implications for other elemental fluxes to the ocean derived from weathering. Due to the reliance on modeled volumetric fluxes of global groundwater discharge, combined with the limited number and wide range of volumetric

estimates currently available, I recommend that the solute fluxes calculated here be treated as first approximations. As additional models and geochemical data become available, these fluxes should be refined, but I hypothesize that these groundwater-derived solute fluxes will continue to be non-negligible and warrant inclusion in updated marine isotope budgets.

References

- Allègre, C. J. *et al.* (2010) 'The fundamental role of island arc weathering in the oceanic Sr isotope budget', *Earth and Planetary Science Letters*, 292(1–2), pp. 51–56.
- Bates, S. L. *et al.* (2017) 'Barium isotopes reveal role of ocean circulation on barium cycling in the Atlantic', *Geochimica et Cosmochimica Acta*, 204, pp. 286–299.
- Beck, A. *et al.* (2013) 'Dissolved strontium behavior in the subterranean estuary and implications for the Sr mass balance and isotope budget of the global ocean', *Geochimica et Cosmochimica Acta*, 117, pp. 33–52.
- Blättler, C. L., Miller, N. R. and Higgins, J. A. (2015) 'Mg and Ca isotope signatures of authigenic dolomite in siliceous deep-sea sediments', *Earth and Planetary Science Letters*, 419, pp. 32–42.
- Cao, Z. *et al.* (2016) 'Constraining the oceanic barium cycle with stable barium isotopes', *Earth and Planetary Science Letters*, 434, pp. 1–9.
- Charbonnier, Q., Moynier, F. and Bouchez, J. (2018) 'Barium isotope cosmochemistry and geochemistry', *Science Bulletin*, 63(6), pp. 385–394.
- Cho, H.M. *et al.* (2018) 'Radium tracing nutrient inputs through submarine groundwater discharge in the global ocean', *Scientific Reports*, 8(1), p. 2439.
- Coplen, T. B. *et al.* (2002) 'Compilation of minimum and maximum isotope ratios of selected elements in naturally occurring terrestrial materials and reagents', *U.S. Department of the Interior U.S. Geological Survey Water-Resources Investigations Report*, 01–4222, pp. 1–76.
- Edmond, J. M. *et al.* (1985) 'Chemical dynamics of the Changjiang estuary', *Continental*

Shelf Research, 4(1–2), pp. 17–36.

- Eisenhauer, A. *et al.* (2019) 'Calcium isotope ratios in blood and urine: A new biomarker for the diagnosis of osteoporosis', *Bone Reports*, 10(March), p. 100200.
- Fantle, M. S. and Tipper, E. T. (2014) 'Calcium isotopes in the global biogeochemical Ca cycle: Implications for development of a Ca isotope proxy', *Earth-Science Reviews*, 129, pp. 148–177.
- Flesch, G. D., Anderson, A. R. and Svec, H. J. (1973) 'A secondary isotopic standard for $^{6}Li/^{7}Li$ determinations', *International Journal of Mass Spectrometry and Ion Physics*, 12(3), pp. 265–272.
- Galy, A. *et al.* (2003) 'Magnesium isotope heterogeneity of the isotopic standard SRM980 and new reference materials for magnesium-isotope-ratio measurements', *Journal of Analytical Atomic Spectrometry*, 18(11), pp. 1352–1356.
- Gibbs, M. T. and Kump, L. R. (1994) 'Global chemical erosion during the Last Glacial Maximum and the present: Sensitivity to changes in lithology and hydrology', *Paleoceanography*, 9(4), pp. 529–543.
- Gonneea, M. E., Mulligan, A. E. and Charette, M. A. (2013) 'Climate-driven sea level anomalies modulate coastal groundwater dynamics and discharge', *Geophysical Research Letters*, 40(11), pp. 2701–2706.
- Gussone, N. *et al.* (2016) *Calcium Stable Isotope Geochemistry*, *Advances in Isotope Geochemistry*. Springer.
- Hartmann, J. and Moosdorf, N. (2012) 'The new global lithological map database GLiM: A representation of rock properties at the Earth surface', *Geochemistry, Geophysics, Geosystems*, 13(12), pp. 1–37.
- Heuser, A. *et al.* (2002) 'Measurement of calcium isotopes ($\delta^{44}Ca$) using a multicollector TIMS technique', *International Journal of Mass Spectrometry*, 220(3), pp. 385–397.
- Higgins, J. A. and Schrag, D. P. (2010) 'Constraining magnesium cycling in marine

sediments using magnesium isotopes', *Geochimica et Cosmochimica Acta*, 74(17), pp. 5039–5053.

- Hogan, J. F. and Blum, J. D. (2003) 'Boron and lithium isotopes as groundwater tracers: A study at the Fresh Kills landfill, Staten Island, New York, USA', *Applied Geochemistry*, 18(4), pp. 615–627.
- Holmden, C. *et al.* (2012) '$\delta^{44/40}$Ca variability in shallow water carbonates and the impact of submarine groundwater discharge on Ca-cycling in marine environments', *Geochimica et Cosmochimica Acta*, 83, pp. 179–194.
- Horner, T. J., Kinsley, C. W. and Nielsen, S. G. (2015) 'Barium-isotopic fractionation in seawater mediated by barite cycling and oceanic circulation', *Earth and Planetary Science Letters*, 430, pp. 511–522.
- Jochum, K. P. *et al.* (2005) 'GeoReM: A New Geochemical Database for Reference Materials and Isotopic Standards', *Geostandards and Geoanalytical Research*, 29(3), pp. 333–338.
- Johannesson, K. H. and Burdige, D. J. (2007) 'Balancing the global oceanic neodymium budget: Evaluating the role of groundwater', *Earth and Planetary Science Letters*, 253(1–2), pp. 129–142.
- Krabbenhöft, A. *et al.* (2009) 'Determination of radiogenic and stable strontium isotope ratios (^{87}Sr/^{86}Sr; $\delta^{88/86}$Sr) by thermal ionization mass spectrometry applying an ^{87}Sr/^{84}Sr double spike'. *Journal of Analytical Atomic Spectrometry*, 24(9), pp. 1267-1271.
- Krabbenhöft, A. *et al.* (2010) 'Constraining the marine strontium budget with natural strontium isotope fractionations (^{87}Sr/^{86}Sr*, $\delta^{88/86}$Sr) of carbonates, hydrothermal solutions and river waters', *Geochimica et Cosmochimica Acta*, 74(14), pp. 4097–4109.
- Luijendijk, E., Gleeson, T. and Moosdorf, N. (2020) 'Fresh groundwater discharge insignificant for the world's oceans but important for coastal ecosystems', *Nature Communications*, 11(1), pp. 1–12.
- Macdonald, F. A. *et al.* (2019) 'Arc-continent collisions in the tropics set Earth's climate

state', *Science*, 184(April), pp. 181–184.

- Magna, T., Wiechert, H. and Halliday, A. (2004) 'Low-blank isotope ratio measurement of small samples of lithium using multiple-collector ICPMS', *International Journal of Mass Spectrometry*, 239, pp. 67–76.
- Misra, S. and Froelich, P. N. (2012) 'Lithium isotope history of cenozoic seawater: Changes in silicate weathering and reverse weathering', *Science*, 335(6070), pp. 818–823.
- Moore, W. S. (1999) 'The subterranean estuary: a reaction zone of ground water and sea water', *Marine Chemistry*, 65(1–2), pp. 111–125.
- Peucker-Ehrenbrink, B. (2018) *Land2Sea Database, Version 2.0*, *Pangaea*.
- Peucker-Ehrenbrink, B. and Fiske, G. J. (2019) 'A continental perspective of the seawater $^{87}Sr/^{86}Sr$ record: A review', *Chemical Geology*, 510(January), pp. 140–165.
- Rad, S. D., Allègre, C. J. and Louvat, P. (2007) 'Hidden erosion on volcanic islands', *Earth and Planetary Science Letters*, 262, pp. 109–124.
- Rahman, S. *et al.* (2019) 'Dissolved silica in the subterranean estuary and the impact of submarine groundwater discharge on the global marine silica budget', *Marine Chemistry*, 208, pp. 29–42.
- Romaniello, S. J. *et al.* (2015) 'Fully automated chromatographic purification of Sr and Ca for isotopic analysis', *Journal of Analytical Atomic Spectrometry*. Royal Society of Chemistry, 30(9), pp. 1906–1912.
- Santos, I. R. *et al.* (2011) 'Uranium and barium cycling in a salt wedge subterranean estuary: The influence of tidal pumping', *Chemical Geology*, 287(1–2), pp. 114–123.
- Stoll, H. M. and Schrag, D. P. (1998) 'Effects of Quaternary sea level cycles on Sr in seawater', *Geochimica et Cosmochimica Acta*, 62(7), pp. 1107–1118.
- Tipper, E. T. *et al.* (2006) 'The magnesium isotope budget of the modern ocean: Constraints from riverine magnesium isotope ratios', *Earth and Planetary Science Letters*, 250(1–2), pp. 241–253.

- Vollstaedt, H. *et al.* (2014) 'The Phanerozoic $\delta^{88/86}$Sr record of seawater: New constraints on past changes in oceanic carbonate fluxes', *Geochimica et Cosmochimica Acta*, 128(May), pp. 249–265.
- Weldeab, S. *et al.* (2007) '155,000 Years of West African Monsoon and Ocean Thermal Evolution', *Science*, 316, pp. 1303–1307.
- Zektser, I. S. (2006) *Groundwater as a component of the environment*. Boston, MA: Springer.
- Zhang, S. and Planavsky, N. J. (2020) 'Revisiting groundwater carbon fluxes to the ocean with implications for the carbon cycle', *Geology*, 48(1), pp. 67–71.
- Zhou, Y. *et al.* (2019) 'Fresh submarine groundwater discharge to the near-global coast', *Geophysical Research Letters*, 46, pp. 1–9.

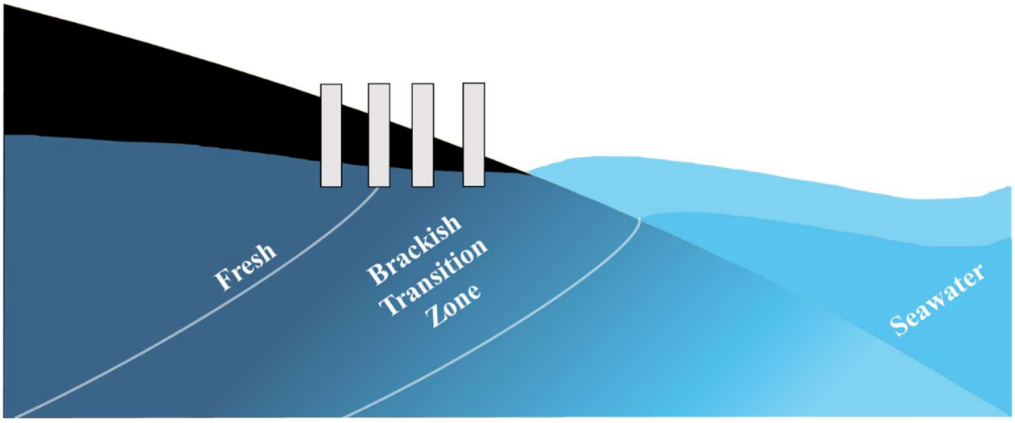

Figure 1. Conceptual diagram of the subterranean estuary and sampling scheme, where grey bars represent sampling across a salinity gradient.

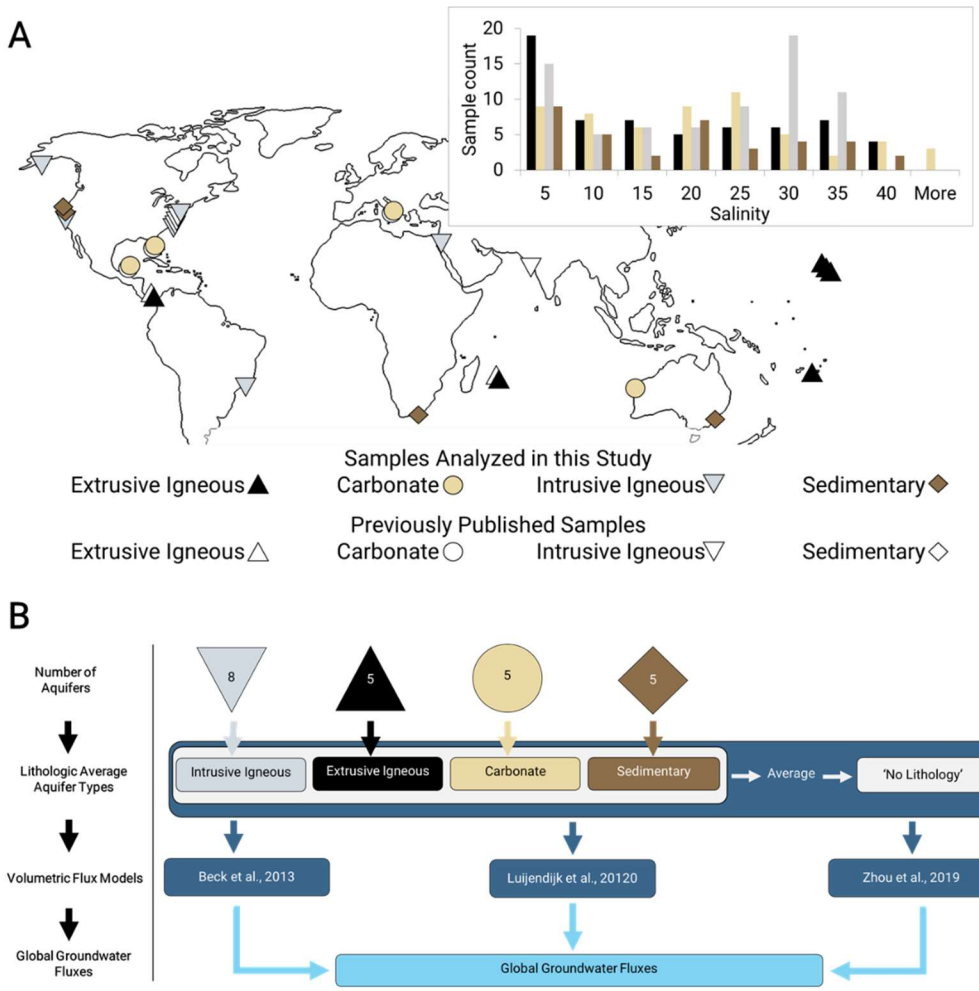

Figure 2. Overview of study design. a, map of aquifer locations (n = 27) from which data were utilized. **a (inset),** number of samples from each salinity range (n = 229; this study and previously published data). **b,** Flow diagram summarizing the calculation pathway to global SGD-derived solute fluxes.

Table 1. Sample Info

Aquifer (this study)	Geology	Aquifer Type	Associated Reference
Veraguas Province, Panama	Extrusive volcanics	Extrusive igneous	(Beck *et al.*, 2013)
Hawai`i Island, HI, USA	Modern basalt (<1 Ma)	Extrusive igneous	(Knee *et al.*, 2010)
Oahu, HI, USA	Quaternary basalt (<2 Ma)	Extrusive igneous	(Mayfield, 2013)
Maui, HI, USA	Quaternary basalt (<2 Ma)	Extrusive igneous	(Bishop *et al.*, 2017)
Moorea, French Polynesia	1.5 - 2.0 Ma volcanics	Extrusive igneous	(Knee *et al.*, 2016)
Flic-en-Flac Lagoon, Mauritius	< 2 Ma basalt	Extrusive igneous	(Povinec *et al.*, 2012)
Puerto Morelos, Yucatan, Mexico	Holocene (<12 ka) karstic limestone	Carbonate	(Null *et al.*, 2014)
Cape Coral, FL, USA	Pleistocene-Holocene sediments (<2 Ma)	Carbonate	(Liu *et al.*, 2017)
Rottnest Island, Australia	Pleistocene-Holocene limestone (<2 Ma)	Carbonate	(Bryan *et al.*, 2016)
Venice Lagoon, Venice, Italy	Modern carbonates	Carbonate	(Rapaglia *et al.*, 2010)
*Everglades, FL, USA	Modern carbonates with some evaporites	Carbonate	(Holmden *et al.*, 2012)
*Carbonate GROUNDWATER average (Florida, Yucatan average)	Modern carbonates with some evaporites	Carbonate	(Holmden *et al.*, 2012)
Waquoit Bay, MA, USA	Granitic Glacial Till	Intrusive Igneous	(Liu *et al.*, 2017)
Great South Bay, NY, USA	Granitic Glacial Till	Intrusive Igneous	(Beck *et al.*, 2008)
Monterey, CA, USA	Mesozoic granites (~180 Ma) and Cenozoic (<66 Ma) sediments	Intrusive Igneous	(Lecher, Fisher and Paytan, 2016)
Kasitsna Bay, AK, USA	Mesozoic metamorphic, volcanic, and igneous intrusive rocks	Intrusive Igneous	(Lecher *et al.*, 2016)
Eilat, Israel	Late Precambrian igneous and metamorphics (630 Ma granite, 790 Ma gneiss, 807 Ma Schists)	Intrusive Igneous	This Study
*Bay of Bengal, Bangladesh	Igneous granites and gneisses	Intrusive Igneous	(Beck *et al.*, 2013)
*Pamet River, MA, USA	Granitic Glacial Till	Intrusive Igneous	(Beck *et al.*, 2013)
*Staten Island, NY, USA	Granitic Glacial Till	Intrusive Igneous	(Hogan and Blum, 2003)
Seabright, CA, USA	Quaternary Sediments (<2.5 Ma)	Sedimentary	(Lecher, Fisher and Paytan, 2016)
Angel Island, CA, USA	Altered Graywacke (~100 Ma)	Sedimentary	(Null *et al.*, 2012)
St Lucia, South Africa	Mesozoic extrusive volcanics (~180 Ma) and Cretaceous (145-65 Ma) Sandstone	Sedimentary	(Moore *et al.*, 2019)
Coffs Harbour, Australia	Lower Permian base rock (slate, schistose sandstone/conglomerate, 250 - 298 Ma) with modern sands	Sedimentary	(Tucker *et al.*, 2019)
Patos Lagoon, Brazil	Pleistocene and Holocene (<2 Ma) sandy cap on an alluvial fan on Precambrian shield	Sedimentary	(Windom and Niencheski, 2003)

*Sampling sites for which only historical data is provided - no new analyses were conducted for this study. Associated reference refers to the study in which the data utilized were published

Table 2. Compilation of concentration data generated in this study

Sample ID	Location	Lithologic 'Aquifer Type'	Salinity	[Li] µg L^{-1}	[Mg] g L-1	[Ca] g L-1	[Sr] mg L-1	[Ba] µg L^{-1}
HBM4	Maui, HI	Extrusive Igneous	33.9	166	1.14	0.39	7.5	43
HBSP3	Maui, HI	Extrusive Igneous	3.5	16	0.07	0.03	0.4	1
Honokowai Well	Maui, HI	Extrusive Igneous	0.0	2	0.02	0.02	0.2	4
HONW	Maui, HI	Extrusive Igneous	0.1	0	0.01	0.01	0.1	1
KaBpiez1	Oahu, HI	Extrusive Igneous	24.2	112	0.93	0.31	5.9	10
KaBpiez2	Oahu, HI	Extrusive Igneous	27.5	137	0.94	0.31	5.9	7
KaBpiez3	Oahu, HI	Extrusive Igneous	27.6	141	0.89	0.27	5.5	7
KaBspring1	Oahu, HI	Extrusive Igneous	1.3	4	0.04	0.04	0.4	10
KaBWell	Oahu, HI	Extrusive Igneous	0.0	0	0.01	0.02	0.1	2
KONA_104	Kona, HI	Extrusive Igneous	24.8	136	0.95	0.31	5.8	16
KONA_300	Kona, HI	Extrusive Igneous	13.4	60	0.50	0.17	3.1	8
KONA_85	Kona, HI	Extrusive Igneous	24.1	143	0.91	0.28	5.4	12
KONA_92	Kona, HI	Extrusive Igneous	14.0	86	0.58	0.19	3.6	10
KONA_93	Kona, HI	Extrusive Igneous	14.0	73	0.52	0.18	3.3	9
M1	Mauritius	Extrusive Igneous	4.2	18	0.14	0.09	1.2	4
M13	Mauritius	Extrusive Igneous	8.3	46	0.27	0.13	2.0	2
M21	Mauritius	Extrusive Igneous	35.7	180	1.21	0.40	8.2	5
M22 3/24	Mauritius	Extrusive Igneous	34.9	168	1.19	0.41	8.3	6
M22 3/25	Mauritius	Extrusive Igneous	31.9	157	1.09	0.41	7.9	8
M24 3/24	Mauritius	Extrusive Igneous	32.3	152	1.10	0.38	7.3	8
M26 3/24	Mauritius	Extrusive Igneous	32.3	153	1.11	0.37	7.3	6
M4	Mauritius	Extrusive Igneous	36.8	173	1.24	0.43	8.5	8
M5	Mauritius	Extrusive Igneous	36.8	169	1.25	0.43	8.6	8
M6	Mauritius	Extrusive Igneous	5.4	28	0.17	0.10	1.3	5
M9	Mauritius	Extrusive Igneous	36.2	165	1.22	0.42	8.3	6
Th_12	Moorea, French Polynesia	Extrusive Igneous	2.8		0.22	0.13	2.0	58
Th_27	Moorea, French Polynesia	Extrusive Igneous	16.6	49	0.40	0.24	6.0	64
Th_42	Moorea, French Polynesia	Extrusive Igneous	15.1		0.00	0.00	0.0	
Th_47	Moorea, French Polynesia	Extrusive Igneous	16.4	46	0.42	0.25	7.3	21
Th_53	Moorea, French Polynesia	Extrusive Igneous	6.0	60	0.22	0.13	2.1	6
Th_60	Moorea, French Polynesia	Extrusive Igneous	14.2		0.55	0.25	5.5	76
Th_62	Moorea, French Polynesia	Extrusive Igneous	21.9		0.81	0.38	8.5	6
LJL227	West Panama	Extrusive Igneous	30.0	118	1.33	0.52	9.5	256
LJL228	West Panama	Extrusive Igneous	0.5	5	0.04	0.02	0.3	15
LJL229	West Panama	Extrusive Igneous	11.5	49	0.30	0.11	2.0	205
LJL230	West Panama	Extrusive Igneous	1.0	5	0.02	0.02	0.1	2
LJL250	West Panama	Extrusive Igneous	5.1	13	0.15	0.20	1.6	48
LJL251	West Panama	Extrusive Igneous	4.2	11	0.12	0.15	1.2	110

V Artisian Well	Venice, Italy	Carbonate	0.7	19	0.04	0.04	0.5	313
VP02	Venice, Italy	Carbonate	12.9	113	0.65	0.33	4.6	43
VP05	Venice, Italy	Carbonate	16.6	104	0.70	0.35	4.8	65
VP07	Venice, Italy	Carbonate	20.4	112	0.80	0.36	5.2	54
VP3	Venice, Italy	Carbonate	14.4	90	0.58	0.29	3.9	51
VP4	Venice, Italy	Carbonate	15.9	84	0.62	0.31	4.2	68
VP-6	Venice, Italy	Carbonate	18.9	111	0.76	0.37	5.3	56
VP8	Venice, Italy	Carbonate	21.3	128	0.93	0.43	6.1	72
Rott1	Rottnest Island, West Australia	Carbonate	24.4	110	0.83	0.34	0.0	62
Rott2	Rottnest Island, West Australia	Carbonate	37.9	184	1.28	0.43	8.4	7
Rott3	Rottnest Island, West Australia	Carbonate	8.0	65	0.25	0.19	0.0	19
Rott4	Rottnest Island, West Australia	Carbonate	0.3	4	0.04	0.05	2.3	2
Rott5	Rottnest Island, West Australia	Carbonate	19.0	74	0.69	0.34	5.0	30
CAL 212	Cape Coral, FL	Carbonate	20.4	21	0.67	1.27	9.3	117
CAL 213	Cape Coral, FL	Carbonate	25.9	36	0.96	0.67	8.9	261
CAL 215	Cape Coral, FL	Carbonate	8.3	49	0.28	0.15	2.2	13
GW 213	Cape Coral, FL	Carbonate	0.4	16	0.03	0.04	2.1	14
FIC_7	Yucatan, Mexico	Carbonate		5	0.32	0.20	4.4	26
FIC_17	Yucatan, Mexico	Carbonate	0.0	2	0.14	0.12	3.2	51
MEX_11	Yucatan, Mexico	Carbonate	39.5	179	1.34	0.46	9.5	19
MEX_63	Yucatan, Mexico	Carbonate	30.6	141	1.04	0.37	7.1	10
MEX_66	Yucatan, Mexico	Carbonate	42.4	191	1.42	0.50	10.2	22
SGD Eilat	Eilat, Israel	Intrusive Igneous	39.7	185	1.33	0.47	9.7	16
MB Academy 1	Monterey, CA	Intrusive Igneous	33.6	160	1.11	0.39	7.8	12
MB Academy 5	Monterey, CA	Intrusive Igneous	27.1	160	1.16	0.41	8.1	18
MB Hopkins 10	Monterey, CA	Intrusive Igneous		304	2.37	0.83	17.7	21
MB Hopkins 11	Monterey, CA	Intrusive Igneous	22.6	161	0.44	0.33	3.9	37
MB Hopkins 15	Monterey, CA	Intrusive Igneous	15.5	134	1.12	0.38	7.5	15
MB Hopkins 16	Monterey, CA	Intrusive Igneous	34.9	152	1.15	0.39	7.9	11
MB Hopkins 18	Monterey, CA	Intrusive Igneous	21.8	159	0.70	0.39	5.7	39
MB Hopkins 19	Monterey, CA	Intrusive Igneous	33.7	149	1.10	0.39	7.7	8
MB Hopkins 39	Monterey, CA	Intrusive Igneous	26.5	150	1.13	0.41	7.8	14
WP 10-5	Southern Brazil	Intrusive Igneous	26.3	206	1.34	0.40	6.4	13
WP 12-5	Southern Brazil	Intrusive Igneous	22.6	155	1.14	0.34	5.6	10
WP 1-5	Southern Brazil	Intrusive Igneous	25.8	166	1.31	0.39	5.9	11
WP 2-5	Southern Brazil	Intrusive Igneous	22.8	156	1.16	0.35	5.7	12
WP 3-S	Southern Brazil	Intrusive Igneous	24.8	172	1.25	0.38	6.0	11
WP 5-5	Southern Brazil	Intrusive Igneous	25.1	171	1.26	0.38	6.1	13
WP 6-5	Southern Brazil	Intrusive Igneous	28.1	201	1.42	0.44	6.8	9
DT1	Waquoit Bay, MA	Intrusive Igneous	0.3	1	0.01	0.01	0.1	1
DT2	Waquoit Bay, MA	Intrusive Igneous	7.6	40	0.27	0.11	1.9	106
DT3	Waquoit Bay, MA	Intrusive Igneous	10.1	40	0.41	0.15	2.7	55
DT4	Waquoit Bay, MA	Intrusive Igneous	17.8	76	0.66	0.22	4.2	31
DT8	Waquoit Bay, MA	Intrusive Igneous	25.6	109	0.95	0.31	6.2	44
DT9	Waquoit Bay, MA	Intrusive Igneous	1.6	8	0.04	0.02	0.3	4
GSB Ba peak	Great South Bay, NY	Intrusive Igneous	30.7	113	1.04	0.35	7.3	173
GSB Fresh	Great South Bay, NY	Intrusive Igneous	0.6	4	0.01	0.02	0.2	25
GSB Mid	Great South Bay, NY	Intrusive Igneous	20.0	102	0.69	0.23	4.4	24
GSB Mid2	Great South Bay, NY	Intrusive Igneous	29.5	140	0.99	0.32	6.5	40
GSB Saline	Great South Bay, NY	Intrusive Igneous	31.7	147	1.08	0.34	7.0	17
AK_102	Kasitsna, AK	Intrusive Igneous	26.2	110	0.92	0.32	6.0	15
AK_115	Kasitsna, AK	Intrusive Igneous	28.9	162	1.04	0.35	6.7	10
AK_131	Kasitsna, AK	Intrusive Igneous	30.2	156	1.06	0.35	7.0	9
AK_15	Kasitsna, AK	Intrusive Igneous	27.9	165	1.07	0.36	7.0	8
AK_38	Kasitsna, AK	Intrusive Igneous	6.3	57	0.17	0.06	1.0	2
AK_48	Kasitsna, AK	Intrusive Igneous	14.5	74	0.47	0.16	2.9	9
AK_49	Kasitsna, AK	Intrusive Igneous	30.4	118	0.85	0.30	5.5	20
AK_75	Kasitsna, AK	Intrusive Igneous	28.7	84	0.39	0.14	2.4	8

Aus 1	East Australia	Sedimentary	2.2	26	0.09	0.16	1.4	55
Aus 10	East Australia	Sedimentary	25.4	122	0.96	0.33	6.1	25
Aus 11	East Australia	Sedimentary	4.4	26	0.20	0.09	1.3	54
Aus 12	East Australia	Sedimentary	4.3	17	0.13	0.08	1.0	23
Aus 13	East Australia	Sedimentary	32.4	181	1.23	0.42	7.9	24
Aus 14	East Australia	Sedimentary	19.7	114	0.77	0.26	4.7	23
Aus 15	East Australia	Sedimentary	11.5	52	0.48	0.18	3.0	30
Aus 16	East Australia	Sedimentary	2.0	12	0.05	0.04	0.4	68
Aus 17	East Australia	Sedimentary	36.3	192	1.28	0.43	8.8	26
Aus 18	East Australia	Sedimentary	35.0	179	1.27	0.42	8.5	47
Aus 2	East Australia	Sedimentary	1.8	25	0.08	0.10	1.1	47
Aus 3	East Australia	Sedimentary	0.4	6	0.01	0.09	0.5	775
Aus 4	East Australia	Sedimentary	0.3	7	0.01	0.07	0.4	32
Aus 5	East Australia	Sedimentary	17.0	74	0.62	0.25	4.1	189
Aus 6	East Australia	Sedimentary	6.0	33	0.21	0.24	2.7	9
Aus 7	East Australia	Sedimentary	0.4	10	0.04	0.06	0.5	8
Aus 8	East Australia	Sedimentary	0.3	3	0.01	0.06	0.3	3
Aus 9	East Australia	Sedimentary	16.5	86	0.66	0.24	4.0	35
MB_31	Santa Cruz, CA	Sedimentary	30.7	178	1.30	0.43	8.7	27
MB_34	Santa Cruz, CA	Sedimentary	9.8	81	0.40	0.14	2.3	14
MB_38	Santa Cruz, CA	Sedimentary	33.6	163	1.25	0.41	8.3	12
MB_56	Santa Cruz, CA	Sedimentary	22.5	129	0.79	0.27	5.0	13
MB_78	Santa Cruz, CA	Sedimentary	10.2	80	0.36	0.12	2.1	8
S.A. ocn	South Africa	Sedimentary	37.0	170	1.24	0.41	8.6	7
SA Fresh	South Africa	Sedimentary	0.2	14	0.03	0.01	0.2	60
SA SL-EM-#3	South Africa	Sedimentary	8.0	57	0.29	0.14	2.1	26
SA SL-EM-#6	South Africa	Sedimentary	7.0	41	0.20	0.08	1.4	7
SFB AI 17 5/10	San Francisco, CA	Sedimentary	17.6	100	0.75	0.23	3.8	29
SFB_2	San Francisco, CA	Sedimentary	25.8	142	1.06	0.36	6.9	30
SFB_22	San Francisco, CA	Sedimentary	22.6	135	0.94	0.33	6.4	22
SFB_27	San Francisco, CA	Sedimentary	25.5	134	0.94	0.33	6.4	36
SFB_39	San Francisco, CA	Sedimentary	24.4	125	0.95	0.33	6.5	37
SFB_72	San Francisco, CA	Sedimentary	26.1	124	0.97	0.34	6.3	39
SFB_85	San Francisco, CA	Sedimentary	9.4	45	0.24	0.12	1.7	21
SFB17 5/10	San Francisco, CA	Sedimentary	17.6	110	0.73	0.25	4.6	30
SFB361009	San Francisco, CA	Sedimentary	17.5	138	0.97	0.35	6.4	31
SFBAI171009	San Francisco, CA	Sedimentary	17.6	132	0.93	0.34	6.2	33

Table 3. Compilation of isotope data generated in this study

Sample ID	δ^{7}Li	± 2 SD	$\delta^{26/24}$Mg	± 2 SD	$\delta^{44/42}$Ca	± 2 SD	$^{87}Sr/^{86}Sr$	$\delta^{88/86}$Sr	$\delta^{138/134}$Ba	± 2 SD
	‰	‰	‰	‰	‰	‰		‰	‰	‰
HBM4			-0.75	0.09			0.70931	0.411		
HBSP3	29.7	0.2	-0.99	0.05	0.87	0.07	0.70929	0.421		
Honokowai Well			-1.10	0.03	0.49	0.05	0.70637	0.317		
HONW	26.4	0.1	-0.61	0.04	0.43	0.04	0.70443	0.319		
KaBpiez1	31.7	0.4	-0.88	0.01			0.70928	0.421	0.40	0.04
KaBpiez2					0.87	0.06	0.70929	0.434		
KaBpiez3					0.86	0.06	0.70932	0.432		
KaBspring1			-0.86	0.09	0.55	0.07	0.70727	0.345		
KaBWell	31.4	0.3			0.50	0.03	0.70554	0.390	0.16	0.03
KONA_104			-0.77	0.03	0.99	0.08			0.08	
KONA_300	30.9	0.3	-0.88	0.04	0.92	0.06	0.70922	0.353	0.02	
KONA_85	30.3	0.1	-0.87	0.06	1.01				0.11	
KONA_92			-0.85	0.00	0.88				-0.03	
KONA_93			-0.83	0.01	0.87				0.03	
M1	30.8	0.2	-1.06	0.05	0.62	0.04	0.70901	0.359	-0.18	0.08
M13			-0.89	0.01	0.82	0.09	0.70917	0.368		
M21			-1.08	0.02	0.91	0.05	0.70931	0.398		
M22 3/24			-0.98	0.06	0.89	0.09	0.70931	0.401		
M22 3/25			-0.92	0.08	0.76	0.04	0.70930	0.399		
M24 3/24					0.83	0.10				
M26 3/24			-0.90	0.18	0.84	0.06	0.70931	0.416		
M4					0.87	0.08	0.70933	0.442		
M5			-0.89	0.09	0.84	0.10	0.70931	0.402		
M6					0.74	0.07	0.70904	0.335		
M9	30.0	0.2	-0.94	0.07	0.82	0.09	0.70931	0.397	0.42	0.03
Th_12	29.1	0.2	-1.00	0.04					0.11	
Th_27			-0.83	0.09						
Th_42			-0.72	0.29						
Th_47			-0.83	0.09						
Th_53	28.9	0.1	-0.85	0.09			0.70915	0.385	0.19	
Th_60			-1.02	0.07					0.13	
Th_62										
LJL227			-0.84	0.02	0.78	0.05				
LJL228	27.6	0.1			0.63	0.08	0.70909	0.403	0.36	0.03
LJL229	27.9	0.1	-0.81	0.12	0.83	0.12	0.70908	0.426	0.33	0.03
LJL230			-0.71	0.04						
LJL250			-0.77	0.04			0.70818	0.306		
LJL251			-0.83	0.04			0.70822	0.313		

V Artisian Well	20.7 0.2	-1.43	0.09	0.50	0.01	0.70843	0.267	0.04	0.03
VP02				0.73	0.07	0.70930	0.398		
VP05		-0.79	0.09	0.80	0.10	0.70930	0.405		
VP07		-0.87	0.09	0.78	0.04	0.70930	0.413		
VP3		-0.88	0.09	0.70	0.04	0.70929	0.407		
VP4	27.4 0.2	-0.87	0.09	0.68	0.09	0.70929	0.399	0.10	0.03
VP-6		-0.80	0.09	0.75	0.02	0.70929	0.400		
VP8				0.68	0.08	0.70929	0.399		
Rott1		-0.85	0.10	0.49	0.05	0.70928	0.236		
Rott2				0.91	0.08	0.70933	0.385		
Rott3		-1.51	0.17	0.53	0.08	0.70927	0.215		
Rott4	28.1 0.3	-1.91	0.03	0.53	0.06	0.70926	0.262	0.24	0.06
Rott5	30.3 0.1	-0.85	0.02	0.70	0.05	0.70932	0.313	0.09	0.04
CAL 212	18.2	-0.97	0.09	0.37	0.03	0.70917	0.318	-0.13	0.03
CAL 213		-0.92	0.12	0.52	0.06	0.70915	0.334	0.09	0.03
CAL 215	34.1	-0.86	0.09	0.75	0.05	0.70914	0.352		
GW 213	23.1 0.0	-1.99	0.04	0.43	0.06	0.70869	0.236	0.46	0.03
FIC_7									
FIC_17								0.24	0.04
MEX_11								0.43	
MEX_63	30.1 0.1	-0.78	0.05	0.93	0.11			0.30	
MEX_66				0.93	0.07			0.30	
SGD Eilat	28.5 0.2			0.94	0.07			0.49	0.03
MB Academy 1				0.93	0.08				
MB Academy 5		-0.79	0.09	0.95	0.09				
MB Hopkins 10		-0.86	0.09	0.88	0.05	0.70934	0.462		
MB Hopkins 11	19.9 0.3	-0.60	0.09	0.71	0.16	0.70932	0.395	0.23	0.03
MB Hopkins 15	17.1 0.1	-0.91		0.69	0.08	0.70935	0.447		
MB Hopkins 16	31.5 0.1	-0.89	0.09						
MB Hopkins 18		-0.83	0.09					0.39	0.03
MB Hopkins 19		-0.77	0.09	0.92	0.04				
MB Hopkins 39				0.82	0.09				
WP 10-5	29.5 0.1			0.93	0.06				
WP 12-5	30.3 0.3			0.91	0.04				
WP 1-5	30.7 0.3			0.88	0.06	0.70936	0.440		
WP 2-5	31.1 0.2			0.97	0.09	0.70936	0.477		
WP 3-S	30.1 0.2			0.86	0.09			0.25	0.05
WP 5-5	30.6 0.4	-1.01	0.03	0.78	0.05			0.04	0.05
WP 6-5	30.2 0.2	-0.86	0.09	0.87	0.11			0.07	0.06
DT1	23.6 0.1	-0.95	0.09	0.57	0.08			0.04	0.04
DT2	49.4 0.3	-0.90	0.09	0.82	0.10	0.70934	0.411	-0.28	0.03
DT3	43.2 0.2	-0.87	0.05	0.83	0.03	0.70935	0.430		
DT4	39.7 0.2	-1.13	0.09	0.90	0.01				
DT8	32.5 0.4	-0.80	0.09	0.87	0.09				
DT9	28.2 0.1	-0.79	0.02	0.88	0.18				

GSB Ba peak	34.40.1	-0.85	0.09	0.93	0.04	0.70931	0.376	0.07	0.03
GSB Fresh	33.30.0	-1.23	0.03	0.49	0.04			-0.01	0.07
GSB Mid	30.40.4	-0.83	0.09	0.85	0.10	0.70933	0.413		
GSB Mid2	30.30.0	-0.83	0.07	0.87	0.08	0.70933	0.415		
GSB Saline	29.80.3	-0.78	0.06	0.82	0.06	0.70930	0.387		
AK_102	29.30.4	-0.82	0.09					0.28	
AK_115		-0.82	0.09	1.05				0.39	
AK_131		-0.82	0.09	0.99				0.40	
AK_15		-0.81	0.09	1.01				0.37	
AK_38	30.50.1	-0.85	0.09						
AK_48	29.70.1	-0.91	0.16	0.95				0.30	
AK_49								0.22	
AK_75		-0.86	0.09	0.94		0.70923	0.358	0.25	
Aus 1	16.9	-0.89	0.09	0.52	0.02	0.70927	0.270		
Aus 10	30.90.2	-0.87	0.09	0.80	0.08				
Aus 11	16.6			0.67	0.06	0.70933	0.367		
Aus 12	16.6	-0.88	0.09	0.39	0.10	0.70929	0.288		
Aus 13		-0.95	0.09	0.86	0.04	0.70932	0.388		
Aus 14				0.85	0.07				
Aus 15	30.80.3	-1.15	0.09	0.76	0.10	0.70932	0.390		
Aus 16		-0.94	0.09			0.70929	0.298		
Aus 17		-0.98	0.09	0.98	0.00				
Aus 18		-0.99	0.09	0.89	0.01				
Aus 2		-0.98	0.09	0.52	0.06	0.70929	0.340		
Aus 3	18.40.1	-1.40	0.09	0.46	0.09	0.70931	0.343	-0.01	0.04
Aus 4		-1.19	0.09	0.41	0.01	0.70929	0.293		
Aus 5	30.10.2	-0.48	0.09	0.79	0.11	0.70931	0.391		
Aus 6		-1.16	0.09	0.49	0.06	0.70927	0.275		
Aus 7	21.20.2	-0.87	0.09	0.53	0.02	0.70930	0.310		
Aus 8	19.30.2	-1.13	0.09	0.75	0.05				
Aus 9		-0.83	0.09			0.70931	0.369		
MB_31	30.70.3			0.93	0.03			0.26	
MB_34		-0.81	0.09	0.87	0.06			0.28	
MB_38	31.40.2			0.85	0.09	0.70932	0.388	0.36	
MB_56				0.94	0.08			0.25	
MB_78		-0.93	0.09	0.89	0.09	0.70938	0.423	0.29	
S.A. ocn	30.60.2			0.93	0.07	0.70932	0.423		
SA Fresh	17.50.0	-0.81	0.09	0.95	0.08			0.25	0.03
SA SL-EM-#3	35.50.2	-0.79	0.09	0.75	0.19	0.70936	0.461	0.15	0.03
SA SL-EM-#6	30.50.2	-0.86	0.06	0.85	0.06	0.70932	0.398		
SFB AI 17 5/10	30.30.4	-0.84	0.09	0.85	0.07				
SFB_2	30.70.6	-0.92	0.09	0.72		0.70929	0.345	0.09	
SFB_22		-0.81	0.09	0.85	0.10	0.70928	0.365	0.25	
SFB_27		-0.83	0.09	0.95				0.14	
SFB_39		-1.00	0.09	0.88	0.07	0.70914		0.18	
SFB_72	31.00.4			0.83		0.70914	0.391	0.08	
SFB_85	30.00.2	-1.00	0.02	0.84	0.11	0.70921	0.348		
SFB17 5/10		-0.50	0.09			0.70922	0.323		
SFB361009		-0.82	0.02	0.91	0.05				
SFBAI171009				0.86	0.05				

Table 4. GLiM endmember classification

va	Extrusive Igneous
vb	
vi	
pa	Intrusive Igneous
pb	
pi	
ig	
mt	
ev	Carbonate
sc	
sm	Sedimentary
ss	
su	
wb	
py	
Nolitho	"No Lithology"
nd	

Grouping of geologic end-members from Luijendijk et al. (2020) for this study.

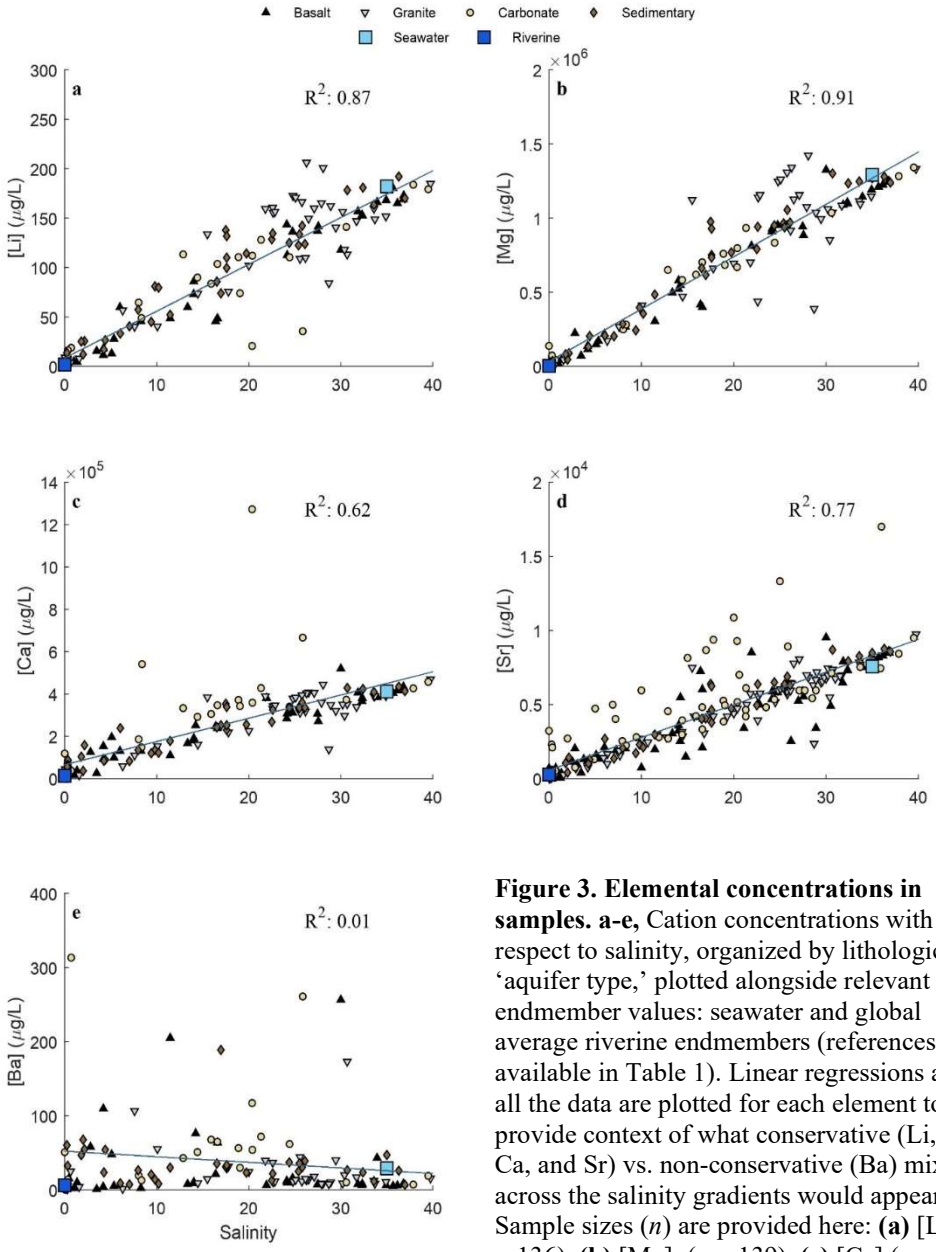

Figure 3. Elemental concentrations in samples. a-e, Cation concentrations with respect to salinity, organized by lithologic 'aquifer type,' plotted alongside relevant endmember values: seawater and global average riverine endmembers (references available in Table 1). Linear regressions across all the data are plotted for each element to provide context of what conservative (Li, Mg, Ca, and Sr) vs. non-conservative (Ba) mixing across the salinity gradients would appear as. Sample sizes (*n*) are provided here: **(a)** [Li]: (*n* = 136), **(b)** [Mg]: (*n* = 139), **(c)** [Ca] (*n* = 140), **(d)** [Sr] (*n* = 225), **(e)** [Ba] (*n* = 56).

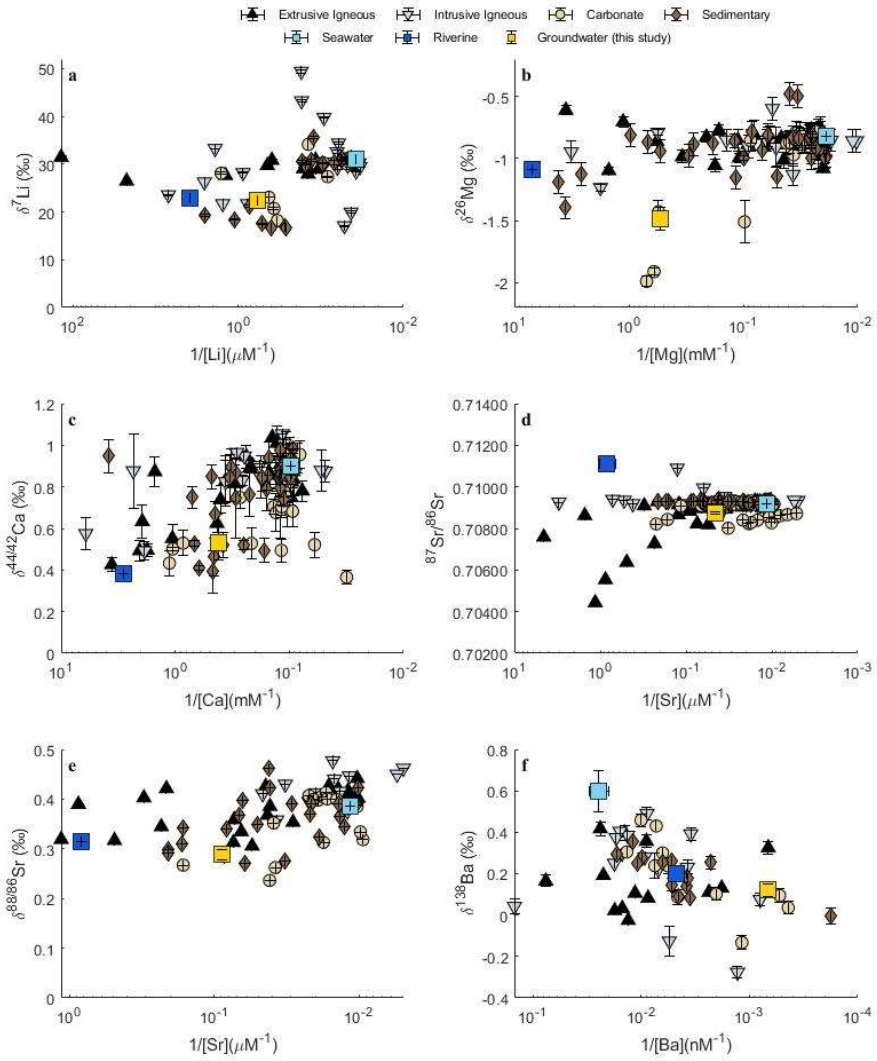

Figure 4. Isotopic composition of samples. a-e, Isotopic compositions with respect to the inverse of cation concentrations, organized by lithologic 'aquifer type,' plotted alongside relevant endmember values: seawater and global average riverine endmembers (references available in Table 1), as well as the average global groundwater composition calculated in this study. Error bars represent the greater of 2SD for each sample's analysis or the long-term uncertainty (2SD) of relevant standard reference materials discussed in the SI. Sample size (*n*) values are provided here: **(a)** $\delta^{7}Li$ (*n* = 67), **(b)** $\delta^{26}Mg$ (*n* = 105), **(c)** $\delta^{44/42}Ca_{915a}$ (*n* = 114), **(d)** $^{87}Sr/^{86}Sr$ (*n* = 168), **(e)** $\delta^{88/86}Sr$ (*n* = 79). **f,** $\delta^{138}Ba$ (*n* = 56).

Table 5. Geologic 'aquifer type' endmember compositions and model outputs of global groundwater chemistry

Parameter	[Li]	$\delta^{7}Li$	[Mg]	$\delta^{26}Mg$	[Ca]	$\delta^{44/42}Ca$	[Sr]	$^{87}Sr/^{86}Sr$	$\delta^{88/86}Sr$	[Ba]	$\delta^{138/134}Ba$
Aquifer Type	(μM)	(‰)	(mM)	(‰)	(mM)	(‰)	(μM)		(‰)	(μM)	(‰)
Extrusive Igneous	0.04	28.6	0.1	-0.85	1.1	0.51	3	0.70695	0.357	0.8	0.10
Carbonate	2.42	24.0	3.3	-1.78	4.3	0.49	15	0.70862	0.255	1.5	0.11
Intrusive Igneous	1.81	28.4	2.1	-1.09	0.8	0.53	2	0.71253	0.411	1.0	0.01
Sedimentary	1.52	19.1	0.7	-1.08	1.5	0.62	2	0.70931	0.354	1.6	0.15
No Lithology	1.45	25.0	1.6	-1.20	2.0	0.54	5	0.70935	0.344	1.3	0.10

No Lithology' represents the 'Complex'/'No Litho' classification units used in the Beck et al., 2013 and Luijendijk et al., 2020, respectively. It is represented by a concentration-weighted average of all four lithologic average 'aquifer type' endmembers.

Table 6. Chemical Composition and Fluxes

Model	Beck et al, 2013	Zhou et al., 2019	Luijendijk et al., 2020	Riverine	Ref.
Volumetric Flux ($km^3\ yr^{-1}$)	2,400	489	286	39,000	(Peucker-Ehrenbrink, 2018)
[Li] (μM)	1.8	1.7	1.7	0.26	
Li (gigamoles yr^{-1})	4.2	0.85	0.49	10	(Misra and Froelich, 2012)
% of riverine flux	42%	9%	5%	-	
$\delta^{7}Li$ (‰)	22.7	22.3	22.0	23	
[Mg] (mM)	1.7	1.9	2.0	0.14	
Mg (teramoles yr^{-1})	4.90	0.91	0.56	5.6	(Tipper *et al.*, 2006)
% of riverine flux	88%	16%	10%	-	
$\delta^{26}Mg$ (‰)	-1.47	-1.48	-1.50	-1.09	
[Ca] (mM)	2.20	2.40	2.60	0.36	
Ca (teramoles yr^{-1})	5.33	1.17	0.73	13.7	(Fantle and Tipper, 2014)
% of riverine flux	39%	9%	5%	-	
$\delta^{44/42}Ca$ (‰)	0.52	0.53	0.54	0.39	
[Sr] (μM)	10.1	11.4	12.6	3.21	
Sr (gigamoles yr^{-1})	24.3	5.6	3.6	47	
% of riverine flux	52%	12%	8%	-	(Krabbenhöft *et al.*, 2010)
$^{87}Sr/^{86}Sr$	0.70876	0.70874	0.70873	0.71106	
$\delta^{88/86}Sr$ (‰)	0.290	0.289	0.287	0.315	
[Ba] (μM)	1.6	1.5	1.5	0.2	
Ba (gigamoles yr^{-1})	3.72	0.74	0.42	8.2	(Cao *et al.*, 2016)
% of riverine flux	45%	9%	5%	-	
$\delta^{138/134}Ba$ (‰)	0.12	0.12	0.12	0.20	

Model outputs for the chemical composition of global average groundwater discharge, given the same geologic aquifer endmember values. Uncertainties represent ranges reported for each model, where available. Riverine values from the denoted literature are reported for context and relevant references for each riverine flux characterization are provided in the final column. *$\delta^{44/42}Ca$ values can be converted to conventional $\delta^{44/40}Ca$ values by multiplying by 2.05 (Heuser *et al.*, 2002).

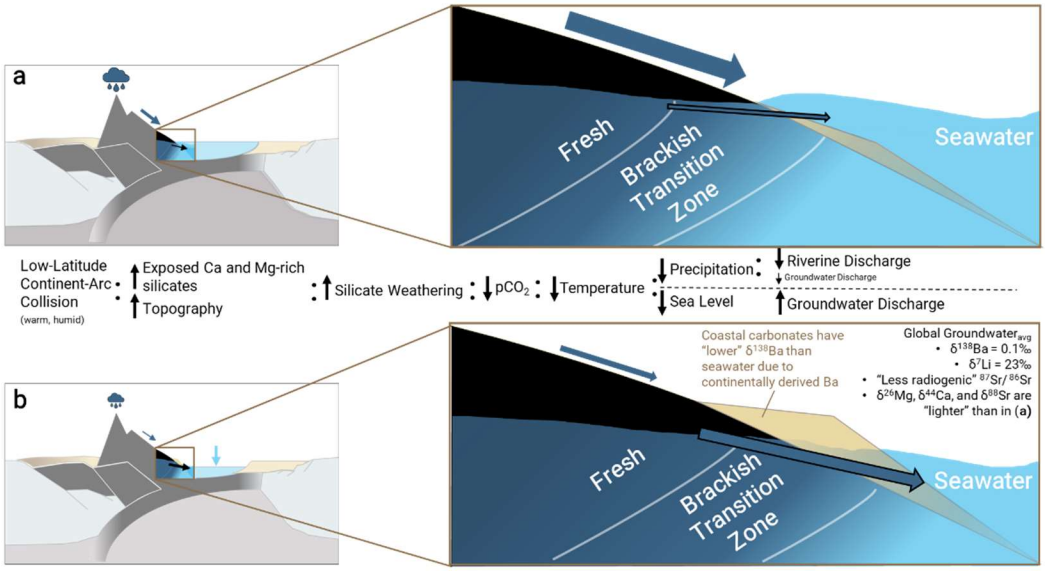

Figure 5 | Illustration of a STE during a shift to glacial conditions. a, interglacial stage steady-state conditions with the subterranean estuary magnified on the right. **(middle),** conceptual outline of the feedback outlined by Macdonald et al. (2019), where a low-latitude island arc collision instigates the onset of global cooling. **b,** glacial conditions with less precipitation and falling sea level with the subterranean estuary magnified on the right and a description of the chemical changes that might occur to the isotopic composition of global groundwater-derived solute fluxes. The tan triangle represents coastal carbonate deposits, whose $\delta^{138}Ba$ composition may be "lighter" than seawater values if previously exposed to terrestrial (groundwater and river water) runoff.

Chapter 3

Isotopic Co-Variation of Dissolved Weathering Products in the Fraser River, Canada

Abstract

Non-traditional stable isotope systematics of rivers and seawater are being scrutinized for their potential as tracers of silicate weathering, a process that helps regulate atmospheric CO_2 on geologic time scales. These systems include $\delta^{7}Li$, $\delta^{26}Mg$, $\delta^{41}K$, $\delta^{44/42}Ca$, and $\delta^{88/86}Sr$. The extent to which these stable isotope compositions are determined by river basin lithology rather than the isotopes' propensity to biotic or abiotic fractionation during processes associated with weathering, such as secondary clay mineral formation, is not well known. Here, I examine the dissolved concentrations and isotopic compositions of Li, Mg, K, Ca, and Sr in the Fraser River (B.C., Canada) to test, by means of an isotope mixing model, whether the effects of source signatures can be isolated from in-stream fractionation processes. The Fraser River watershed is characterized by a pronounced contrasts in bedrock geology and climate that cause the composition of the dissolved load to shift seasonally between more dominant contributions from the geologically younger, volcanically active Coast Range and the geologically older sedimentary units in the Rocky Mountains, as shown by previous studies of $^{87}Sr/^{86}Sr$ (Cameron *et al.*, 1995; Voss *et al.*, 2014) and $\delta^{34}S$ (Burke *et al.*, 2018). This setting can be viewed as a microcosm of what has happened globally in the past when surficial processes shifted from a regime dominated by young, volcanic bedrock along active margins or large igneous provinces to one dominated by cratonic bedrock. The shift in the chemistry of Fraser River water from a more Coast Range to a stronger Rocky Mountain influence is associated with decreases in $\delta^{7}Li$ and $\delta^{26}Mg$, as well as an increases in $^{87}Sr/^{86}Sr$, $\delta^{34}S$ and $\delta^{41}K$. Of the stable isotope systems analysed in this study, $\delta^{7}Li$ correlates most significantly with silicate weathering-derived cation fluxes. Notably, this

correlation is stronger than that for $^{87}Sr/^{86}Sr$, which confirms that $\delta^{7}Li$ is a useful proxy for silicate weathering fluxes. However, most temporal changes in non-traditional stable isotope records of seawater cannot be primarily driven by changes in continental input if isotope co-variations observed in the dissolved load of the Fraser River are representative of continental runoff.

Introduction

The primary mechanisms through which atmospheric CO_2 is sequestered on geologic timescales is the weathering of silicate minerals rich in Ca and Mg, in conjunction with the balance between the global production and respiration of organic matter (Urey, 1952; Berner *et al*., 1983; Berner, 1994). Changes in the flux of global weathering products to the ocean are reflected as changes in the concentration and isotopic composition of elements in seawater that integrate global processes. Elements with residence times longer than the ocean mixing time (e.g. Li, Mg, K, Ca, Sr, Os) record global processes and leave records of isotope variations in marine archives (e.g. Broecker and Peng, 1982). The radiogenic isotope systems $^{87}Sr/^{86}Sr$ (e.g. Veizer, 1989; Berner, 1994; Mcarthur *et al.*, 2001) and $^{187}Os/^{188}Os$ (e.g. Pegram *et al.*, 1992; Peucker-Ehrenbrink and Ravizza, 2000) have been utilized to infer changes in silicate weathering over geologic timescales. The utility of these radiogenic systems stems from the large contrast between the isotopic composition of old continental crust with large parent/daughter element ratios and young mantle sources with small time-integrated parent/daughter ratios. Trends toward more radiogenic $^{87}Sr/^{86}Sr$ and $^{187}Os/^{188}Os$ values in marine archives have, therefore, been interpreted to indicate increased release of radiogenic Sr and Os from the continents, which has been assumed to reflect increased silicate weathering (e.g. Raymo *et al*., 1988; Berner, 1994; Ravizza *et al*., 2000). However, the response of the marine $^{87}Sr/^{86}Sr$ isotope system is strongly buffered by carbonate weathering (Veizer, 1989), whereas the marine $^{187}Os/^{188}Os$ record is strongly influenced by the cycling of sedimentary organic matter (Ravizza and Esser, 1993; Bickle *et al.*, 2005; Dubin and Peucker-Ehrenbrink, 2015). The inherent limitations of both systems to

track changes in silicate weathering-derived fluxes motivates the search for new proxy records that more directly reflect changes in the global flux of silicate weathering products to the ocean.

A promising avenue of research, made possible by advances in high-precision mass spectrometry, is the use of non-traditional stable isotopes of weathering products, such as $\delta^{7}Li$, $\delta^{26}Mg$, $\delta^{41}K$, $\delta^{44/42}Ca$, and $\delta^{88/86}Sr$. In contrast to the radiogenic systems, whose utility is based on provenance differences, the utility of these stable isotope systems is based on the combination of provenance and low-temperature fractionation processes that include changes in chemical weathering regimes (Gussone *et al.*, 2003; Halicz *et al.*, 2008; Wimpenny *et al.*, 2010; Li *et al.*, 2019). Marine records of these isotopes are being reconstructed and interpreted with the aim of understanding changes in weathering fluxes over geologic timescales (De La Rocha and DePaolo, 2000; Farkas *et al.*, 2007; Misra and Froelich, 2012; Vollstaedt *et al.*, 2014; Higgins and Schrag, 2015). Lithium and K hold particular promise as they are primarily associated with silicate minerals. In contrast, Mg, Ca, and Sr are also sensitive to carbonate weathering. While Li isotopes have long been used as a proxy for weathering conditions in river basins (Huh *et al.*, 1998; Pistiner and Henderson, 2003; Kisakurek *et al.*, 2005; Vigier *et al.*, 2009; Millot, Vigier and Gaillardet, 2010; Tipper *et al.*, 2012; Dellinger *et al.*, 2014; Pogge von Strandmann, Frings and Murphy, 2017), our knowledge of processes, such as mineral surface reactions, clay formation, and biological utilization, that lead to fractionation in the other isotope systems is still too limited to confidently interpret their marine isotope records.

With many compounding biotic and abiotic fractionation processes at play, I investigate this suite of isotope systems and their response to gradients in bedrock geology, hydrology, climate and ecozones in the well-characterized drainage basin of the Fraser River to improve our ability to interpret isotope signals in continental runoff. Rivers integrate fractionation processes at the drainage basin scale and are the dominant transport vector for weathering products to the ocean. Insights gleaned from variations in $\delta^{7}Li$, $\delta^{26/24}Mg$, $\delta^{44/42}Ca$, $\delta^{41}K$, and $\delta^{88/86}Sr$ of river water are, therefore, directly applicable to the interpretation of marine isotope records. The Fraser River basin in British Columbia, Canada, experiences large seasonal shifts in the sources of its dissolved load that are driven by a pronounced

spring freshet (Cameron and Hattori, 1997; Voss *et al.*, 2014). The freshet is characterized by a shift to radiogenic $^{87}Sr/^{86}Sr$, large $\delta^{34}S$ values and light stable water isotope compositions, which reflect input from old marine sedimentary sequences in the Rocky Mountains. During base flow conditions from late fall to early spring, input from the volcanically active young Coast Range delivers less radiogenic Sr, S of magmatic pedigree (low $\delta^{34}S$), and stable water isotopes characteristic of low-altitude precipitation from the Pacific Ocean. By observing how non-traditional stable isotope systems co-vary with well-understood radiogenic ($^{87}Sr/^{86}Sr$) and traditional stable (δ D, $\delta^{18}O$, $\delta^{34}S$) isotope signatures, I hope to gain insights into the utility of non-traditional isotope systems for understanding surficial processes that contribute to temporal changes in the isotopic composition of these elements in seawater. The geotectonic contrast between the active Coast Range and the sedimentary units along the North American craton that formed the Rocky Mountains could be significant for interpreting marine isotope records in the context of supercontinent cycles, during which continental runoff shifts from being dominated by young active to older passive margins.

Methods

Study Area and Sample Description

The Fraser River drains (Fig. 1) a mid-size watershed (220,000 km^2) in western Canada with stark contrast in bedrock geology that range from young igneous bedrock of the Coast Range on the western side of the basin to Paleozoic/Precambrian metamorphosed sedimentary/carbonate substrate of the Rocky Mountains in the east. This contrasting regional geology, combined with hydrologic seasonality, imparts large shifts in the chemistry of its dissolved load (Cameron and Hattori, 1996; Voss *et al.*, 2014). The Fraser River hydrology is characterized by three distinct regimes: base flow conditions (December – March) when river discharge is low and precipitation accumulates as snow in the Coast Range and Rocky Mountains, a spring freshet (April – July) during which the river is fed by a mixture of snowmelt and rainfall, and sporadic discharge events in the fall (August – November) that

are driven by storms off the Pacific Ocean (Cameron *et al.*, 1995; Voss *et al.*, 2014). During base flow and fall storm conditions the chemistry of the dissolved load of the Fraser River has a less radiogenic $^{87}Sr/^{86}Sr$ and lower $\delta^{34}S$ composition relative to the spring freshet – indicative of a greater influence of the young, volcanically active Coast Range on the dissolved load (Figs. 2 and 3; Cameron *et al.*, 1995; Voss *et al.*, 2014; Burke *et al.*, 2018). During the spring freshet, when the snowpack melts and the discharge of the Fraser River is high, the $^{87}Sr/^{86}Sr$ of the dissolved load becomes much more radiogenic and the $\delta^{34}S$ composition increases, indicating that the dissolved load is more strongly influenced by the older, predominantly marine sedimentary units of the Intermontane Belt, Omineca Fold Belt, and Rocky Mountains (Figs. 2 and 3; Cameron *et al.*, 1995; Voss *et al.*, 2014).

These chemical variations are observed at the time-series monitoring station at Fort Langley in the lower Fraser River floodplain (Fig. 3) where sampling has occurred nearly bi-weekly since 2009. Additionally, eight of the Fraser tributaries were sampled under different flow conditions from 2009 - 2011. These tributaries include four that represent the more radiogenic ($^{87}Sr/^{86}Sr > 0.71$) Rocky Mountain and interior fold belt endmembers (McBride, McGregor, Quesnel, and Thompson) and four of the less-radiogenic ($^{87}Sr/^{86}Sr < 0.71$) Coast Range endmember (Nechako, Blackwater, Chilcotin, and Harrison). The distinct seasonality in the chemistry of the dissolved load of the Fraser River main stem, in conjunction with the sampling of the geologically less-diverse tributaries that drain distinct geologic lithologies, presents a unique opportunity to investigate isotopic co-variability between $\delta^{7}Li$, $\delta^{26/24}Mg$, $\delta^{44/42}Ca$, $\delta^{41}K$, $\delta^{88/86}Sr$, as well as $^{87}Sr/^{86}Sr$ and $\delta^{34}S$ sourced from two distinct geologic provenances.

Materials

Twenty four filtered (0.45µm) surface water samples from the Fraser River main stem at Fort Langley, three from the Fraser main stem at Fitzwilliam in the Rocky Mountain headwaters, and three from the Chilcotin tributary, which drains the Coast Range to the East, were analyzed for their $\delta^{7}Li$, $\delta^{26/24}Mg$, $\delta^{41}K$, $\delta^{44/42}Ca$, $^{87}Sr/^{86}Sr$, and $\delta^{88/86}Sr$ compositions (Fig. 1; Table 1; Table 2). $\delta^{41}K$ data for the

Fraser main stem was obtained from Wang *et al.* (in review) and $\delta^{34}S$ time series data for the Fraser main stem and select tributaries were reported by Burke *et al.* (2018) and Cameron *et al.* (1995), respectively (Table 1). Elemental concentration and $^{87}Sr/^{86}Sr$ data for the Fraser River main stem have been published by Voss *et al.* (2014). Discharge data for the Fraser and its gauged tributaries were obtained from the Environment Canada Water Office (http://www.wateroffice.ec.gc.ca).

Analytical Methods

Laboratory Analyses

Lithium concentrations were analyzed at the Czech Geological Survey (CGS) with an Agilent 5110 ICP-optical emission spectrometer (OES). Chemical and analytical methods for the preparation and analysis of $\delta^{7}Li$, $\delta^{26/24}Mg$, $\delta^{44/42}Ca$, $^{87}Sr/^{86}Sr$, and $\delta^{88/86}Sr$ by multi-collector ICPMS or TIMS are identical to those described in Chapter 2.

Modeling Methods

In an attempt to separate endmember isotope signatures from in-stream fractionation processes, I expand a hydrochemical mixing model optimized for $^{87}Sr/^{86}Sr$ (Voss *et al.,* 2014) to include concentrations and stable isotope compositions. By comparing measured and modeled isotope compositions and concentrations I test whether physical mixing of endmembers needs to be complemented by additional fractionation processes during river transport in order to fully explain observed element concentrations and isotope compositions.

Model Description

Voss *et al.* (2014) mix volumetric contributions from eight tributaries (McBride on the upper Fraser River as well as the McGregor, Blackwater [aka: Westroad], Quesnel, Nechako, Chilcotin, Thompson, and Harrison rivers) by time-lagging volumetric discharges (Q) of each tributary according

to the distance from the tributary inflow to the Fort Langley station, according to average water flow velocities. Time-delays range from six days for the McBride gauging station to no delay for the Harrison River. Strontium concentrations ([Sr]) and $^{87}Sr/^{86}Sr$ compositions of each tributary were equal to the average of three data points representative of different flow stages of tributaries between 2009 – 2011. Tributary Sr fluxes (F_{Sr}) on any given day are the product of the tributary discharge on that day (Q) and a static [Sr] for that tributary. For each model day, all eight tributary values were summed (Σ), yielding a predicted Sr concentration value at the Fort Langley station. The $^{87}Sr/^{86}Sr$ composition of the dissolved load at Fort Langley was calculated using an isotope mixing equation for elemental fluxes (F) and isotope ratios (I) for the eight tributaries. Small variations in the atomic mass of Sr were neglected.

As not all sampled tributaries in the Fraser River basin are gauged and not all gauged tributaries were sampled for their chemistry, hence some tributary fluxes could not be constrained with data (Fig. 4). Voss *et al.* (2014) account for the 'missing' Sr flux by calculating the difference between the expected Sr flux (F_{Sr}) (F_{Sr} = Σ F_{Sr} for all eight tributaries) and the observed F_{Sr} at Fort Langley on each model day. This 'missing' Sr flux was attributed to contributions from the ungauged tributaries and, possibly, groundwater inputs. The $^{87}Sr/^{86}Sr$ composition of this 'missing' F_{Sr} was estimated by minimizing the sum of residual squares:

$$\sum_{i=1}^{n} \left(y_i - \hat{f}(\mathrm{x_i}) \right)^2$$

where y_i denotes the observed isotopic compositions and $\hat{f}(x_i)$ symbolizes the modeled output of the isotopic composition on any given day (i), for the duration of the model (n) = 800 days. The $^{87}Sr/^{86}Sr$ composition of the missing F_{Sr} was continuously adjusted until the offset between the observed and modeled $^{87}Sr/^{86}Sr$ was minimized at $^{87}Sr/^{86}Sr_{missing}$ = 0.708. Based on the endmember values for the Rocky Mountain tributaries ($^{87}Sr/^{86}Sr$ = 0.720) and Coast Range tributaries ($^{87}Sr/^{86}Sr$ = 0.7046), the fraction of the 'missing flux' with Coast Range characteristics was estimated at 78%, with the remaining 22% having Rocky Mountains characteristics. The 'missing flux' of Sr was then included in

the model as a virtual 'tributary'. Finally, a three-day running mean was computed to smooth the model output. Modeled $^{87}Sr/^{86}Sr$ values were in close agreement with observations at the Fort Langley Fraser station, though trends in Sr concentrations ([Sr]) were not well captured (Fig 3).

Voss *et al.* (2014) quantify a mean residual ($\bar{e}$) value for the observed (y_i) and modeled ($\hat{f}(\mathrm{x_i})$) [Sr] and $^{87}Sr/^{86}Sr$ values on each day (i) of the original model for which observational data existed (d) via the following equations:

$$e_i = \left(y_i - \hat{f}(\mathrm{x_i})\right)$$

$$\bar{e} = \frac{1}{d}\sum_{i=1}^{d} e_i$$

This mean residual value ($\bar{e}$) for each of the solutes and their isotopes was then normalized to the average of observed values ($\bar{y}$) to create a 'normalized mean residual' ($\bar{e}_n$).

$$\bar{y} = \frac{1}{d}\sum_{i=1}^{d} y_i$$

$$\bar{e}_n = \frac{\bar{e}}{\bar{y}}$$

This normalization permits comparing model fits of the different solutes and their isotopes irrespective of the magnitude of the range in isotope values. The [Sr] model had an $\bar{e}_n$ of 0.35, indicating higher observed [Sr] at Fort Langley on every occasion. In contrast, the $^{87}Sr/^{86}Sr$ model had an $\bar{e}_n$ of -0.0014, indicative of slightly less radiogenic observed values compared to the model output.

Model Refinements

I adopt the above model with a few modifications in order to describe the concentrations and isotope compositions of the non-traditional stable isotope systems I measured in the Fraser River solely by physical mixing of endmembers. The modifications include incorporation of historical hydrochemical data, discharge-dependent solute concentrations in the tributaries, and a re-calculation of the chemical composition of the 'missing flux' component. By incorporating historical

concentration data for the tributaries (Cameron *et al.,* 1995), the number of data points for each solute concentration in the tributaries increased from three to five, thereby improving constraints on the range of concentrations observed. In addition, rather than assuming a static solute concentration for each tributary, I account for dilution effects in each tributary as a function of discharge. The flux of each element in a tributary ($F_{tributary}$) on any given model day is calculated as:

$$F_{tributary} = Q_{tributary} * 10^{\beta_0 + \beta_1 log(Q_{tributary})}$$

where $Q_{tributary}$ symbolizes the discharge of a tributary on that day ($m^3\ s^{-1}$), β_1 represents the Type II linear relationship between Log (Q) vs. Log (X) at Fort Langley (X = solute concentration; Fig. 2), and β_0 stands for the intercept of the Log (Q) vs. Log (X) relationship for that specific tributary. I use slopes that are based on the Fort Langley time series data and intercepts specific to each tributary because the Fort Langley dataset for Q and X is data-rich (n = 26 for Li, n = 60 for other elements), whereas the tributary datasets are data-poor (n = 5), yet highly variable in in absolute concentrations, and thus intercept values.

Concentration data for all constituents (Mg, Ca, K, SO_4), except Li, are available for all eight tributaries (Cameron *et al.*, 1995; Voss *et al.*, 2014). Only two data points were available for Li in each tributary from Cameron *et al.* (1995). To expand the data set, I analyzed Li concentrations in the upper Fraser River gauging station at Fitzwilliam and the Chilcotin tributary. Isotope data for $^{87}Sr/^{86}Sr$ and $\delta^{34}S$ are also available for all seven tributaries; all other isotopic data ($\delta^{7}Li$, $\delta^{26/24}Mg$, $\delta^{41}K$, $\delta^{44/42}Ca$, $\delta^{88/86}Sr$) were generated in this study for the Fitzwilliam station and Chilcotin tributary. In the mixing model, the hydrochemistries of the McBride, McGregor, Quesnel, and Thompson rivers were all approximated to have the same isotopic composition as the Fitzwilliam gauging station on the upper Fraser River, which represents the headwater tributaries in the Rocky Mountains and the interior fold belts. The isotopic compositions of Nechako, Blackwater, Chilcotin, and Harrison rivers that drain the Coast Range were approximated with the Chilcotin composition. This binary 'binning' scheme for the tributaries is based on the $^{87}Sr/^{86}Sr$ data with a cut-off value of 0.710.

I constrain the chemistry of the 'missing flux' with a similar residual sum of squares approach as the original model. However, the daily Sr fluxes calculated for the 'missing flux' changes due to the new discharge-weighted concentration relationships described above. Furthermore, while the $^{87}Sr/^{86}Sr$ composition of the Coast Range remains unchanged (0.7046), the Rocky Mountains endmember is now more radiogenic (0.7317) than in the original model (0.7200), because I included the highly radiogenic value (~0.74) for the upper Fraser River at Fitzwilliam. Consequently, the 'missing flux' component calculated using the residual sum of squares approach for $^{87}Sr/^{86}Sr$ is comprised of 81% Coast Range and 19% Rocky Mountain contributions (compared to 78% and 22% in the original model). To examine if the mixing proportions of the model are consistent for the another quasi-conservative isotope system, the residual sum of squares appraoch was independently determined for the $\delta^{34}S$ dataset, which has endmember isotope values for the Rocky Mountain and Coast Range endmembers of 10.7‰ and -0.85‰, respectively. This yields a mixture of 85% Coast Range and 15% Rocky Mountain contributions for the 'missing flux'. I use the average of these two independently calculated mixing proportions (87% and 13%) to estimate the isotopic composition of the 'missing flux' component for $\delta^{7}Li$, $\delta^{26/24}Mg$, $\delta^{41}K$, $\delta^{44/42}Ca$, and $\delta^{88/86}Sr$ (Table 1).

Silicate Weathering-Derived Cation Fluxes

Fluxes of Mg and Ca derived from silicate weathering impact the carbon cycle on geologic time scales, whereas fluxes of Mg and Ca from the dissolution of carbonates do not, at least not on long timescales (Beaulieu *et al.*, 2012). An isotope proxy that correlates specifically with silicate weathering-derived cation fluxes in river discharge may therefore prove useful for long-term paleoclimate reconstructions. To asses which, if any, of these six isotope systems is a promising proxy for silicate weathering fluxes, I calculated daily silicate weathering-derived cation fluxes ($\mu mol\ s^{-1}$) using the forward modeling approach of Li *et al.* (2019).

The model necessitates four assumptions. First, the concentration of chlorine [Cl^-] in every sample is derived from a combination of precipitation and evaporite inputs. Second, both precipitation and

evaporite inputs have static molar concentration ratios (k) of [Cl^-] to other cations (Li, Na, Mg, K, Ca, and Sr) that are identical to seawater. Third, the remaining [Li^+], [Na^+], and [K^+] in the samples, after accounting for precipitation and evaporite input, are entirely derived from silicate (i.e. not carbonate) weathering. Fourth, the ratios (c) of [Na^+] to [Mg^{2+}], [Ca^{2+}], and [Sr^{2+}] in silicate weathering are static. Then, silicate weathering-derived cation concentrations $[X]_S$ can be written as:

$$[X]_{pe} = [X]_0 - k\,[Cl^-]$$

For [Li^+], [Na^+], and [K^+]: $[X]_S = [X]_{pe}$

For [Mg^{2+}], [Ca^{2+}], and [Sr^{2+}]: $[X]_S = c\,[Na^+]_S$

where the subscript *pe* denotes precipitation and evaporation-corrected concentration values. The molar concentration ratios (k) of [Cl^-] to Na, Ca, Mg, K, Sr, and Li used in the calculation of $[X]_{pe}$ are 0.87, 0.02, 0.11, 0.02, 0.00028, and 0.000028, respectively, representative of the average seawater values used in Gaillardet *et al.* (1999). The molar concentration ratios (c) of [Na^+] to Ca, Mg, and Sr, used in the calculation of $[X]_S$ are 0.54, 0.2, and 0.002, representative of the average silicate values used in Gaillardet *et al.* (1999). Then, silicate weathering-derived cation fluxes (F_S, in μmol s^{-1}) are the product of the concentration $[X]_S$ and the discharge (Q) for the day of sample collection (Table 2).

$$F_S = [X]_S * Q$$

Results

Cation Concentrations

The relative molar abundance of dissolved cations in the Fraser River measured in this study are Ca (79%), Mg (17%), K (3.5%), Sr (0.4%), and Li (0.004%) (Table 1). As SO_4 concentrations are approximately equal to 2/3 of the Ca concentration, SO_4 is the major anion (see also Cameron and Hattori, 1997; Voss *et al.*, 2014). Over the course of two seasons, Sr and Ca concentrations decreased by a factor of ~1.5, Mg by a factor of ~2, SO_4 and K by ~2.5, and Li by ~3 with increasing discharge

during the spring freshet, indicative of significant ($R^2 > 0.4$, with the exception of Li with an $R^2 = 0.2$) negative correlations between the Log of discharge ($m^3\ s^{-1}$) (Log[Q]) and the Log of cation concentrations (Log[X]) (Fig. 2).

Isotope Tracers

Isotope ratios of four systems (Li, Mg, S, and Sr) were significantly correlated with discharge in the Fraser main stem. $^{87}Sr/^{86}Sr$ and $\delta^{34}S$ are positively correlated with the Log(Q) ($R^2 \geq 0.2$), while $\delta^{7}Li$ and $\delta^{26}Mg$ show negative correlations ($R^2 \geq 0.2$) (Fig. 2). $\delta^{41}K$, $\delta^{44/42}Ca$, and $\delta^{88/86}Sr$ do not correlate with discharge; in fact, $\delta^{44/42}Ca$ values do not vary outside of analytical uncertainty (Fig. 3). There are two options to determine the $\delta^{7}Li$, $\delta^{26}Mg$, and $\delta^{41}K$ endmember values for the study site. The first is based on the endmember values of the dissolved load at the Chilcotin River and the upper Fraser River at Fitzwilliam, which is what I do in this study. However, because these ratios are significantly ($R^2 \geq 0.45$) correlated with $^{87}Sr/^{86}Sr$, I could also use the $^{87}Sr/^{86}Sr$ endmember values, for which more data is available from the Fort Langley time series, to constrain the endmember values by extrapolation of their correlations. Both approaches yield similar endmember values within the uncertainties of the slopes of the Type II linear correlations (Fig. 5), supporting the robustness of my approach. For instances when the isotopic composition of the endmembers could not be observationally constrained ($\delta^{26}Mg$ of Fitzwilliam and $\delta^{41}K$ of both endmembers), the extrapolated value is used. Amongst the isotope data from the main stem, the most significant correlations emerged between $\delta^{7}Li$, $\delta^{26}Mg$, and $\delta^{41}K$ ($R^2 \geq 0.1$) (Fig. 6).

Model Comparison to Data

The normalized mean residuals ($\bar{e}_n$) for [Sr] and $^{87}Sr/^{86}Sr$ decreased compared to the original model, suggesting better agreement between the revised model and the data. Specifically, the residuals for [Sr] decreased from +0.35 to -0.34, indicating that observed Sr concentrations are significantly

lower than predicted by the new model, by about the same amount that the original model underestimated them. While my expanded model (solid lines in Fig. 3) captures the general trends in the concentration data (triangles in Fig. 3), significant offsets between modeled and observed concentrations point to the need for future model adjustments.

The fact that residuals for $^{87}Sr/^{86}Sr$ decreased by an order of magnitude from 0.0014 in the original model to 0.0001 in the expanded model indicates that my new model more accurately captures the $^{87}Sr/^{86}Sr$ variability observed at Fort Langley. General trends in $\delta^{7}Li$, $\delta^{26}Mg$, and $\delta^{34}S$, such as lower $\delta^{7}Li$ and $\delta^{26}Mg$, as well as higher $\delta^{34}S$ values during the spring freshet, are also reproduced by this expanded model. As the $\delta^{44/42}Ca$ and $\delta^{88/86}Sr$ values of the two endmembers (Fitzwilliam station and Chilcotin tributary) are identical within analytical uncertainty, the model cannot capture temporal variations. Due to the lack of $\delta^{41}K$ data for the tributaries and for dominant lithologies in the basin, I had to use the $\delta^{41}K$ values that the Type II linear regression with $^{87}Sr/^{86}Sr$ yielded (Fig. 5). Interestingly, the $\delta^{41}K$ chemistries of these two endmembers converged on the bulk silicate Earth value in the calculation of the 'missing' composition (Fig. 5; Table 2) (Morgan *et al.*, 2018; Santiago Ramos *et al.*, 2018).

Silicate Weathering-Derived Cation Flux Calculations

Average silicate weathering-derived cation fluxes (F_S) for the Fraser River main stem at Fort Langley are ~2 μmol s^{-1} for Li, ~50 μmol s^{-1} for Sr, ~2.5 mmol s^{-1} for Mg and K, and ~5.0 mmol s^{-1} for Ca (Table 3), equivalent to annual dissolved fluxes of approximately 0.1, 2, 75, 75, and 150 gigamoles of Li, Sr, Mg, K, and Ca, respectively. Lithium is the only isotope system that correlates with F_S ($\delta^{7}Li$, $R^2 = 0.2 – 0.4$; Fig. 10), and the relationship between $\delta^{7}Li$ and F_S is negative. Interestingly, $\delta^{7}Li$ and F_S display contrasting correlations in the two endmember tributary basins: negative in the Chilcotin tributary (Coast Range) and positive in the Fraser headwaters (Fitzwilliam in the Rocky Mountains) (Fig. 7). Though intriguing, I consider this finding preliminary because of the small sample size (n = 3).

Discussion

Model Efficacy

The output of the revised model overlaps with observational data and mimics trends in Li and SO_4 concentrations as well as δ^7Li, δ^{26}Mg, ^{87}Sr/^{86}Sr, and δ^{34}S compositions. This indicates that rapid shifts in hydrochemistry can be captured by simply summing contributions from hydrologic endmembers in this system. An obvious shortcoming of the model, however, is that it systematically overestimates dissolved Mg, Ca, and Sr concentrations, while underestimating K concentrations. This is likely caused by using Log (Q) vs. Log (X) slopes that are derived from Fort Langley main stem data, rather than individual tributaries for which I had few data (n=5). Additional data on tributary chemistry, particularly for solute concentrations at extreme flow conditions, could significantly improve the definition of Log (Q) vs. Log (X) slopes and, thus, improve modeled dissolved concentrations in the main stem. Additional δ^{41}K data for endmember tributaries might help bring the model output into better agreement with observed δ^{41}K variations in the Fraser River. My expanded model also cannot capture the observed, subtle temporal changes in the $\delta^{44/42}$Ca and $\delta^{88/86}$Sr composition of the dissolved load because endmember values are identical within analytical uncertainty. This observation is surprising, as I expected $\delta^{88/86}$Sr of Rocky Mountain tributaries to carry the signature of isotopically light marine carbonates (Krabbenhöft *et al.*, 2010) compared to the isotopically heavier "bulk silicate earth"-like composition of the Coast Range (Table 2).

Silicate Weathering: δ^7Li, δ^{26}Mg, and δ^{41}K

Of all the isotopes analyzed, δ^7Li has the most significant, yet site-specific, correlation with silicate weathering-derived cation fluxes (F_S) (Fig. 7). While δ^7Li is negatively correlated with silicate weathering-derived cation fluxes in the Fraser River main stem and in the Chilcotin tributary, it is positively correlated with F_S at the Fitzwilliam station in the Fraser headwaters. The former can be

explained by the interaction of Li with secondary clay minerals formed during the alteration of silicate minerals. In the laboratory experiments conducted by Millot and Girard (2007), as well as Wimpenny *et al.* (2010), ^{6}Li is preferentially, yet with variable preference, incorporated into secondary silicates, rendering the residual Li in the leachates isotopically heavy. Clay minerals analyzed in those studies included smectite, kaolinite, illite, chlorite, and chrysotile. While both experimental studies found that ^{6}Li was preferentially adsorbed by clay minerals, the effect this had on the dissolved load varied, owing to varying fractionation factors for the different clay minerals (Millot and Girard, 2007). Similarly, field studies of δ^{7}Li in rivers have reported that data cannot be explained by a single fractionation factor related to clay mineral formation (e.g. Kisakurek *et al.*, 2005; Millot *et al.*, 2010; Yoon, 2010; Pogge von Strandmann *et al.*, 2017) (Fig. 8). As weathering reactions approach congruency and more cations are released into the dissolved phase, the fluid becomes increasingly enriched in ^{6}Li, resulting in negative correlations between silicate weathering fluxes and the δ^{7}Li composition of dissolved loads. Such correlations have been documented in numerous studies of rivers (e.g. Kisakurek *et al.*, 2005; Vigier *et al.*, 2009; Millot *et al.*, 2010; Hindshaw *et al.*, 2019), including the neighboring Mackenzie River, tributaries draining the Rocky Mountains, the Canadian Shield, and the Western Cordillera (Millot *et al*., 2010).

It is also possible that an unconstrained endmember contributes to the dissolved load of the upper Fraser at Fitzwilliam during periods of higher discharge, which is characterized by increasing dissolved Li fluxes and heavier δ^{7}Li composition (Fig. 2; Fig. 7). Interestingly, increasing dissolved Li fluxes with heavier δ^{7}Li signatures were observed during high discharge conditions in the McMurdo Dry Valley in Antarctica by Witherow *et al.* (2010). The authors of that study concluded that isotopically heavier Li was released from terminal glacial lakes only during periods of high discharge, when such lakes were reconnected to perennial streams. The headwaters of the Fraser River near Fitzwilliam are dotted with numerous terminal lakes, such as Icefall Lake (52°40'02"N, 118°21'36"W), Jade Lake (52°39'45"N, 118°23'40"W) and many unnamed smaller lakes. Unfortunately, I did not

analyze any samples from lakes in the Fraser headwater region and inputs from such lakes were not explicitly included as a separate endmember in the isotope mixing model.

The observed negative correlation ($R^2 > 0.3$) between $\delta^{26}Mg$ and $\delta^{41}K$ in the Fraser River main stem at Fort Langley (Fig. 6) is reminiscent of experimental studies that report preferential adsorption of isotopically heavier Mg (Wimpenny, *et al.*, 2010; Santiago Ramos *et al.*, 2016) and lighter K (Li *et al.*, 2019) onto clay minerals. Finding confirmation of these experimental results in a natural setting is reassuring. As neither isotope system shows correlations with F_S, I conclude that neither appears suitable to reliably trace silicate weathering fluxes.

Carbonate Weathering: $\delta^{26}Mg$, $\delta^{44/42}Ca$, and $\delta^{88/86}Sr$

The Rocky Mountains contain accreted terranes rich in marine carbonate and clastic sediment deposits (Fig. 1). Of the isotopes examined in this study, $\delta^{26}Mg$, $\delta^{44/42}Ca$, and $\delta^{88/86}Sr$ are the ones most relevant to carbonate weathering (e.g. Fantle and Tipper, 2014; Vollstaedt *et al.*, 2014; Higgins and Schrag, 2015). These previous studies demonstrate that modern biogenic carbonates preferentially incorporate the lighter isotopes of Mg, Ca, and Sr. I therefore expected, but did not consistently find, runoff intercepted at Fitzwilliam in the Rocky Mountain headwater region to be isotopically lighter than the Chilcotin tributary in the Coast Range.

Consistent with expectations, the inferred $\delta^{26}Mg$ composition of the Fraser River at Fitzwilliam (-1.68‰) is lower than that of the Chilcotin (-0.56‰). The more negative value was inferred from one preliminary unpublished data point for the Fraser at Fitzwilliam, but was corroborated by the close agreement between modeled and observed $\delta^{26}Mg$ data in the main stem, where the preliminary value of -1.68‰ was used to represent the Fitzwilliam (Rocky Mountain) endmember. Further corroboration is provided by the relationship between Ca/Na and $\delta^{26}Mg$ (Fig. 9), which indicates that the Fraser River can be modeled as a mixture of more silicate-like Coast Range values (heavier $\delta^{26}Mg$, lower Ca/Na) with a more strongly carbonate-dominated Rocky Mountain endmember (lighter $\delta^{26}Mg$, higher Ca/Na).

In contrast, the $\delta^{44/42}$Ca and $\delta^{88/86}$Sr values observed at Fitzwilliam are within analytical uncertainty identical to those of the Chilcotin (Table 1; Table2). This observation can be rationalized by the effect of carbonate metamorphism during orogeny. Discussed by Blättler and Higgins (2017), $\delta^{44/42}$Ca values of Precambrian carbonates (0.39‰) are identical within analytical uncertainty (±0.08‰, long-term 2SD of IAPSO seawater standard) to those of Bulk Silicate Earth (0.46 ± 0.14‰). This is to be expected because, over long (>100 Myr) timescales, riverine "sources" of Ca have to be in balance with global carbonate "sinks" (see Urey, 1952). It is, therefore, no surprise that all $\delta^{44/42}$Ca values measured in this study cover a similar range (0.29 – 0.48‰).

I hypothesize that a similar argument can be made for $\delta^{88/86}$Sr. At the outset of my study, I had expected the headwaters (Fitzwilliam), which are more strongly influenced by carbonate weathering, to carry the light stable Sr isotope signature of marine biogenic carbonates. In contrast, I expected the stable Sr isotope composition of runoff from the Coast Range (Chilcotin) to be similar to Bulk Silicate Earth. However, both regions are characterized by nearly identical $\delta^{88/86}$Sr values (0.29 – 0.36‰), which are similar to those of Bulk Silicate Earth (0.25 – 0.31‰; Krabbenhöft *et al.*, 2010; Moynier *et al.*, 2010). Stevenson *et al.* (2018) found that $\delta^{88/86}$Sr values in eastern Canadian streams only ranged between 0.26 – 0.39‰, despite large differences in bedrock geology. I interpret this finding as independent support of my hypothesis that $\delta^{44/42}$Ca and $\delta^{88/86}$Sr in continental runoff are controlled by similar processes.

Conclusions

Observed trends towards more radiogenic dissolved Sr during the spring freshet are accompanied by trends to lower δ^{7}Li and δ^{26}Mg, and – possibly – slightly higher $\delta^{44/42}$Ca isotope values. With the possible exception of Mg, these correlations are very different from reconstructions of marine isotope values over the past ~30 Myr, a period of densest data coverage. Over this period, seawater has acquired an isotopic composition more radiogenic in Sr (McArthur *et al.*, 2010), heavier in Li isotope ratios (Misra and Froelich, 2012; Sun *et al.*, 2018)Misra and Froelich, 2012; Sun *et al.*, 2018), and

slightly lighter in Ca isotope ratios ((De La Rocha and DePaolo, 2000). Depending on the reconstructions, the stable Mg isotope composition of seawater has either remained relatively constant over the past 30 Myr (Higgins and Schrag, 2015; Gothmann *et al.*, 2017) or has shifted to lower $\delta^{26}Mg$ over the past 20 Myr (Pogge Von Strandmann *et al.*, 2014), making it difficult to draw conclusions regarding its relation to the Fraser River record. Despite the ambiguity in the reconstructions and interpretation of the marine Mg isotope record, temporal changes in the composition of stable isotope systems I investigated cannot be primarily driven by variations in dissolved riverine inputs associated with silicate weathering, if the chemical composition of the Fraser River is representative of dissolved riverine input in general. Instead, temporal changes in stable isotope compositions of seawater must primarily be determined by intra-oceanic processes, such as biogenic carbonate precipitation (Krabbenhöft *et al.*, 2010), hydrothermal exchange reactions (Voigt *et al.*, 2020), diagenetic processes including reverse weathering (Dunlea *et al.*, 2017), as well as changes in temperature (Marriott *et al.*, 2004), reaction rate and saturation state (Lemarchand *et al.*, 2010; Böhm *et al.*, 2012; Alkhatib and Eisenhauer, 2017). It remains to be seen whether the co-variations in isotope composition seen in the Fraser River time series characterize continental runoff in general. Only additional studies of multiple isotope systems of runoff from different geotectonic settings will help clarify whether and how the stable isotope composition of global continental runoff undergoes shifts from being dominated by young active to older passive margins on the timescale of supercontinent cycles.

References

- Alkhatib, M. and Eisenhauer, A. (2017) 'Calcium and strontium isotope fractionation in aqueous solutions as a function of temperature and reaction rate', *Geochimica et Cosmochimica Acta*, 209, pp. 296–319.
- Beaulieu, E. *et al.* (2012) 'High sensitivity of the continental-weathering carbon dioxide sink to future climate change', *Nature Climate Change*, 2(5), pp. 346–349.
- Berner, R. a. (1994) 'GEOCARB II; a revised model of atmospheric CO_2 over Phanerozoic

time', *American Journal of Science*, 294(1), pp. 56–91.

- Bickle, M. J. *et al.* (2005) 'Relative contributions of silicate and carbonate rocks to riverine Sr fluxes in the headwaters of the Ganges', *Geochimica et Cosmochimica Acta*, 69(9), pp. 2221–2240.
- Blättler, C. L. and Higgins, J. A. (2017) 'Testing Urey's carbonate–silicate cycle using the calcium isotopic composition of sedimentary carbonates', *Earth and Planetary Science Letters*, 479, pp. 241–251.
- Böhm, F. *et al.* (2012) 'Strontium isotope fractionation of planktic foraminifera and inorganic calcite', *Geochimica et Cosmochimica Acta*, 93, pp. 300–314.
- Broecker, W. S. and Peng, T. H. (1982) 'Tracers in the Sea', *Lamont-Doherty Geol. Obs., Palisades, NY*.
- Burke, A. *et al.* (2018) 'Sulfur isotopes in rivers: Insights into global weathering budgets, pyrite oxidation, and the modern sulfur cycle', *Earth and Planetary Science Letters*, 496, pp. 168–177.
- Cameron, E. M. *et al.* (1995) 'Isotopic and elemental hydrogeochemistry of a major river system: Fraser River, British Columbia, Canada', *Chemical Geology*, 122(1–4), pp. 149–169.
- Cameron, E. M. and Hattori, K. (1997) 'Strontium and neodymium isotope ratios in the Fraser River, British Columbia: A riverine transect across the Cordilleran orogen', *Chemical Geology*, 137(3–4), pp. 243–253.
- Dellinger, M. *et al.* (2014) 'Lithium isotopes in large rivers reveal the cannibalistic nature of modern continental weathering and erosion', *Earth and Planetary Science Letters*, 401, pp. 359–372.
- Dunlea, A. G. *et al.* (2017) 'Mg/Ca via reduced reverse weathering', *Nature Communications*, 8(844), pp. 1–6.
- Fantle, M. S. and Tipper, E. T. (2014) 'Calcium isotopes in the global biogeochemical Ca cycle: Implications for development of a Ca isotope proxy', *Earth-Science Reviews*, 129, pp.

148–177.

- Farkas, J. *et al.* (2007) 'Calcium isotope record of Phanerozoic oceans: Implications for chemical evolution of seawater and its causative mechanisms', *Geochimica et Cosmochimica Acta*, 71(21), pp. 5117–5134.
- Gaillardet, J. *et al.* (1999) 'Global silicate weathering and CO_2 consumption rates deduced2 from the chemistry of large rivers', *Chemical Geology*, 159(1–4), pp. 3–30. doi: http://dx.doi.org/10.1016/S0009-2541(99)00031-5.
- Gothmann, A. M. *et al.* (2017) 'A Cenozoic record of seawater Mg isotopes in well-preserved fossil corals', *Geology*, 45(11), pp. 1039–1042.
- Gussone, N. *et al.* (2003) 'Model for kinetic effects on calcium isotope fractionation ($\delta^{44}Ca$) in inorganic aragonite and cultured planktonic foraminifera', *Geochimica et Cosmochimica Acta*, 67(7), pp. 1375–1382.
- Halicz, L. *et al.* (2008) 'Strontium stable isotopes fractionate in the soil environments?', *Earth and Planetary Science Letters*, 272(1–2), pp. 406–411.
- Higgins, J. A. and Schrag, D. P. (2015) 'The Mg isotopic composition of Cenozoic seawater - evidence for a link between Mg-clays, seawater Mg/Ca, and climate', *Earth and Planetary Science Letters*, 416, pp. 73–81.
- Huh, Y. *et al.* (1998) 'Lithium and its isotopes in major world rivers: implications for weathering and the oceanic budget', *Geochimica et Cosmochimica Acta*, 62(12), pp. 2039–2051.
- Kisakurek, B., James, R. H. and Harris, N. B. W. (2005) 'Li and δ^7Li in Himalayan rivers: Proxies for silicate weathering?', *Earth and Planetary Science Letters*, 237(3–4), pp. 387–401.
- Krabbenhöft, A. *et al.* (2010) 'Constraining the marine strontium budget with natural strontium isotope fractionations ($^{87}Sr/^{86}Sr^*$, $\delta^{88/86}Sr$) of carbonates, hydrothermal solutions and river waters', *Geochimica et Cosmochimica Acta*, 74(14), pp. 4097–4109.

- De La Rocha, C. L. and DePaolo, D. J. (2000) 'Isotopic evidence for variations in the marine calcium cycle over the Cenozoic', *Science*. American Association for the Advancement of Science, 289(5482), pp. 1176–1178.
- Lemarchand, E. *et al.* (2010) 'Lithium isotope systematics in a forested granitic catchment (Strengbach, Vosges Mountains, France)', *Geochimica et Cosmochimica Acta*, 74(16), pp. 4612–4628.
- Li, S. *et al.* (2019) 'K isotopes as a tracer for continental weathering and geological K cycling', *Proceedings of the National Academy of Sciences of the United States of America*, 116(18), pp. 8740–8745.
- Marriott, C. S. *et al.* (2004) 'Temperature dependence of δ^{7}Li , δ^{44}Ca and Li / Ca during growth of calcium carbonate', *Earth and Planetary Science Letters*, 222, pp. 615–624.
- Mcarthur, A. J. M. *et al.* (2001) 'Strontium Isotope Stratigraphy : LOWESS Version 3 : Best Fit to the Marine Sr - Isotope Curve for 0 – 509 Ma and Accompanying Look - up Table for Deriving Numerical Age', *Journal of Geology*, 109(2), pp. 155–170.
- Millot, R. and Girard, J. P. (2007) 'Lithium isotope fractionation during adsorption onto mineral surfaces', in *International Meeting on Clays in Natural & Engineered Barriers for Radioactive Waste Confinement*.
- Millot, R., Vigier, N. and Gaillardet, J. (2010) 'Behaviour of lithium and its isotopes during weathering in the Mackenzie Basin, Canada', *Geochimica et Cosmochimica Acta*, 74(14), pp. 3897–3912.
- Misra, S. and Froelich, P. N. (2012) 'Lithium isotope history of cenozoic seawater: Changes in silicate weathering and reverse weathering', *Science*, 335(6070), pp. 818–823.
- Morgan, L. E. *et al.* (2018) 'High-precision ^{41}K/^{39}K measurements by MC-ICP-MS indicate terrestrial variability of: δ 41K', *Journal of Analytical Atomic Spectrometry*. Royal Society of Chemistry, 33(2), pp. 175–186.
- Moynier, F. *et al.* (2010) 'Sr stable isotope composition of Earth, the Moon, Mars, Vesta and

meteorites', *Earth and Planetary Science Letters*, 300(3–4), pp. 359–366.

- Pegram, W. J. *et al.* (1992) 'The record of sea water $^{187}Os/^{186}Os$ variation through the Cenozoic', *Earth and Planetary Science Letters*, 113(4), pp. 569–576.
- Peucker-Ehrenbrink, B. and Ravizza, G. (2000) 'The marine osmium isotope record', *Terra Nova*, 12(5), pp. 205–219.
- Pistiner, J. S. and Henderson, G. M. (2003) 'Lithium-isotope fractionation during continental weathering processes', *Earth and Planetary Science Letters*, 214(1–2), pp. 327–339.
- Pogge Von Strandmann, P. A. E., Forshaw, J. and Schmidt, D. N. (2014) 'Modern and Cenozoic records of seawater magnesium from foraminiferal Mg isotopes', *Biogeosciences*, 11(18), pp. 5155–5168.
- Pogge von Strandmann, P. A. E., Frings, P. J. and Murphy, M. J. (2017) 'Lithium isotope behaviour during weathering in the Ganges Alluvial Plain', *Geochimica et Cosmochimica Acta*, 198, pp. 17–31.
- Raymo, M. E., Ruddiman, W. F. and Froelich, P. N. (1988) 'Influence of late Cenozoic mountain building on ocean geochemical cycles', *Geology*, 16(7), pp. 649–653.
- Santiago Ramos, D. P. *et al.* (2018) 'Reverse weathering in marine sediments and the geochemical cycle of potassium in seawater: Insights from the K isotopic composition ($^{41}K/^{39}K$) of deep-sea pore-fluids', *Geochimica et Cosmochimica Acta*, 236, pp. 99–120.
- Santiago Ramos, D. P., Dunlea, A. G. and Higgins, J. A. (2016) 'Paired measurements of K and Mg isotopes and clay authigenesis in marine sediments', in *American Geophysical Union: Fall Meeting*.
- Stevenson, R. *et al.* (2018) 'Weathering processes, catchment geology and river management impacts on radiogenic ($^{87}Sr/^{86}Sr$) and stable ($\delta^{88/86}Sr$) strontium isotope compositions of Canadian boreal rivers', *Chemical Geology*, 486(April), pp. 50–60.
- Sun, H. *et al.* (2018) 'Rapid enhancement of chemical weathering recorded by extremely light seawater lithium isotopes at the Permian-Triassic boundary', *Proceedings of the National*

Academy of Sciences of the United States of America, 115(15), pp. 3782–3787.

- Tipper, E. T. *et al.* (2012) 'Positive correlation between Li and Mg isotope ratios in the river waters of the Mackenzie Basin challenges the interpretation of apparent isotopic fractionation during weathering', *Earth and Planetary Science Letters*, 333–334, pp. 35–45.
- Urey, H. C. (1952) 'On the Early Chemical History of the Earth and the Origin of Life', *Proceedings of the National Academy of Sciences of the United States of America*, 38(4), p. 351.
- Veizer, J. (1989) 'Strontium isotopes in seawater through time', *Annual Reviews in Earth and Planetary Science*, 17, pp. 141–167.
- Vigier, N. *et al.* (2009) 'The relationship between riverine lithium isotope composition and silicate weathering rates in Iceland', *Earth and Planetary Science Letters*, 287(3–4), pp. 434–441.
- Voigt, M. *et al.* (2020) 'Magnesium isotope fractionation during hydrothermal seawater-basalt interaction', *Geochimica et Cosmochimica Acta*, 272, pp. 21–35.
- Vollstaedt, H. *et al.* (2014) 'The Phanerozoic $\delta^{88/86}$Sr record of seawater: New constraints on past changes in oceanic carbonate fluxes', *Geochimica et Cosmochimica Acta*, 128(May), pp. 249–265.
- Voss, B. M. *et al.* (2014) 'Tracing river chemistry in space and time: Dissolved inorganic constituents of the Fraser River, Canada', *Geochimica et Cosmochimica Acta*, 124, pp. 283–308.
- Wang, K. *et al.* (In Review) 'Potassium isotopes in major world rivers: Implications for weathering and oceanic budget', *Earth and Planetary Science Letters*.
- Wimpenny, J. *et al.* (2010) 'The behaviour of Li and Mg isotopes during primary phase dissolution and secondary mineral formation in basalt', *Geochimica et Cosmochimica Acta*, 74(18), pp. 5259–5279.
- Witherow, R. A., Lyons, W. B. and Henderson, G. M. (2010) 'Lithium isotopic composition

of the McMurdo Dry Valleys aquatic systems', *Chemical Geology*, 275(3–4), pp. 139–147.

- Yoon, J. (2010) 'Lithium as a silicate weathering proxy: Problems and perspectives', *Aquatic Geochemistry*, 16(1), pp. 189–206.

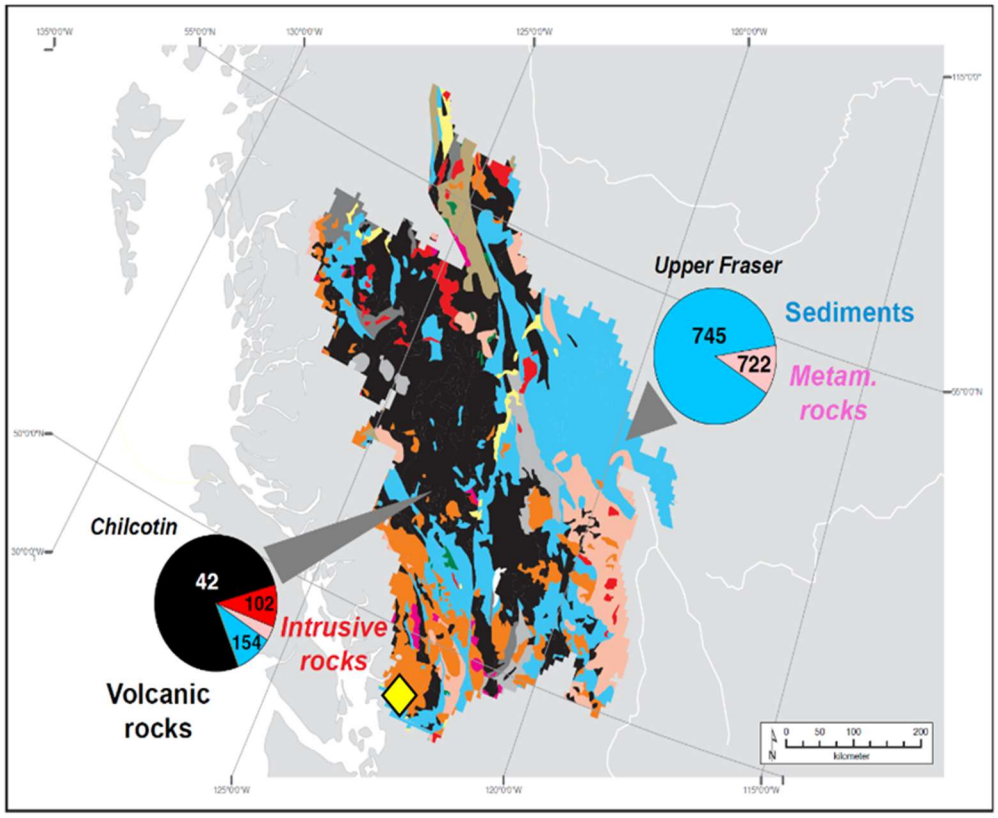

Figure 1 | Watershed map of the Fraser River, adapted from Voss *et al.* (2014). The two (nearly) monolithic endmember tributary basins are labeled with color-coded circles. Average bedrock ages (in Myr) of the various lithologies are shown as numbers in the pie diagrams. The time series monitoring station is shows as a yellow diamond.

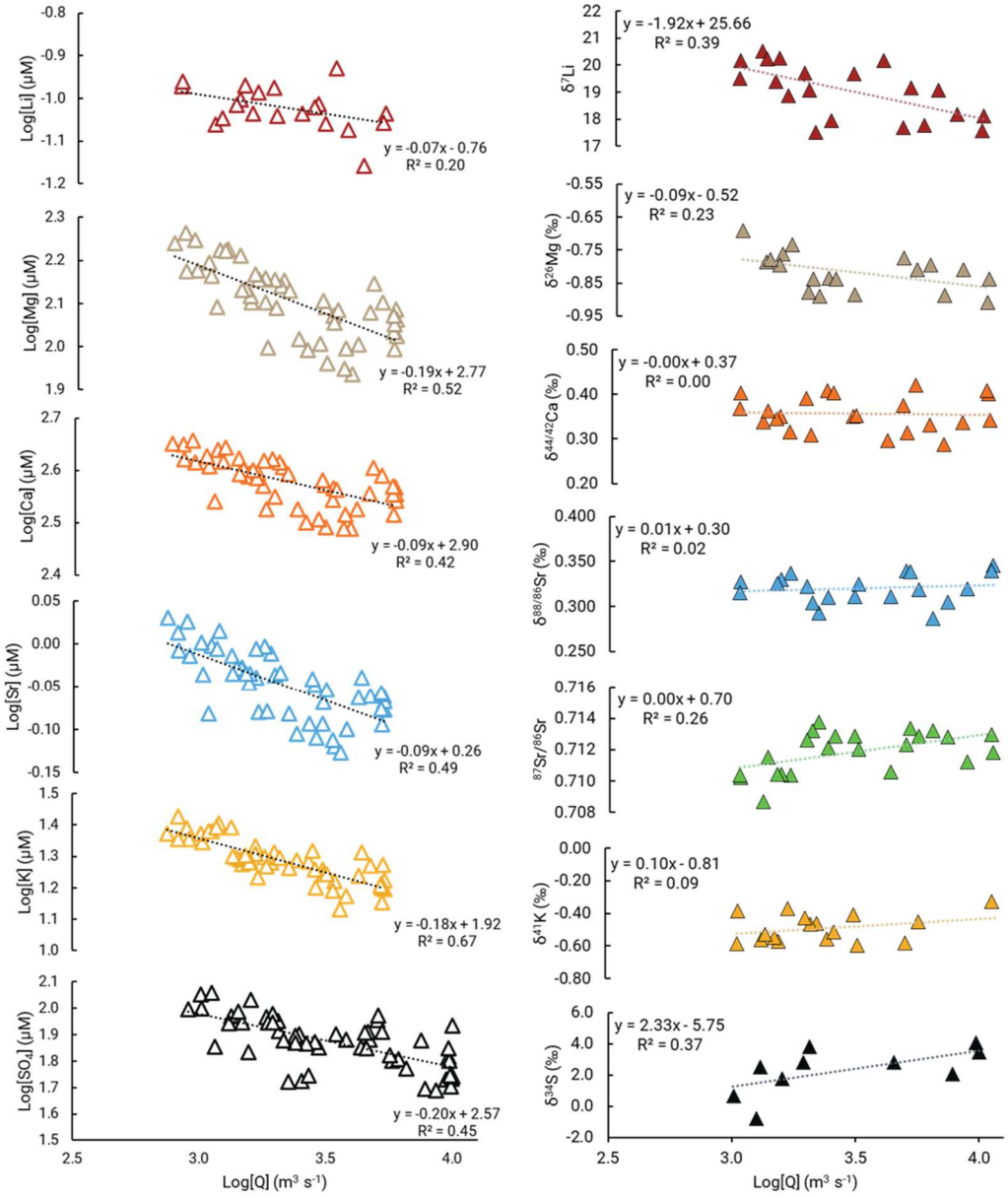

Figure 2 | (left) The log of major and trace solute concentrations in the dissolved load in the Fraser River time series at Fort Langley, plotted against the log of discharge, where the dashed lines represent Type I linear regressions through the data. **(right)** Isotopic composition of the dissolved load in the Fraser River time series at Fort Langley, plotted against the log of discharge, where the dashed lines represent Type I linear regressions through the data.

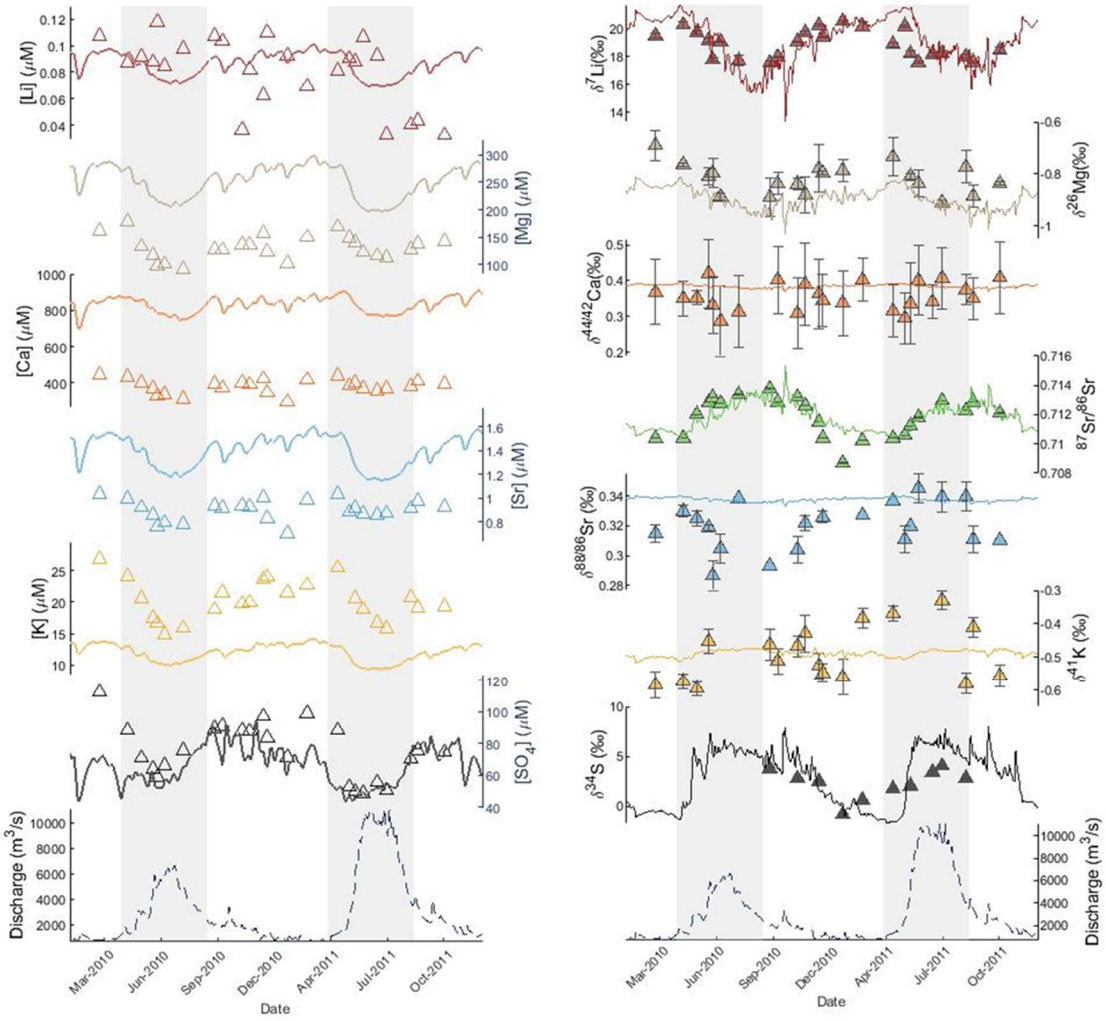

Figure 3 | (left) Major and trace chemistry of the dissolved load in the Fraser River time series at Fort Langley, where the solid lines represent model outputs, triangles represent observations, and the dashed line represents discharge at the Mission gauging station (the closest gauging station to Fort Langley). From top to bottom: Li, Mg, Ca, Sr, K, SO_4, and volumetric discharge at Mission – the final monitoring station of Fraser River, whose discharge was discussed at length in Voss *et al*. (2014). Shaded grey bars approximate the 'spring freshet'. **(right)** Isotopic composition of the dissolved load in the Fraser River time series at Fort Langley, where the solid lines represent model outputs, triangles represent observations, and the dashed line represents discharge. From top to bottom: $\delta^{7}Li$, $\delta^{26/24}Mg$, $\delta^{44/42}Ca$, $^{87}Sr/^{86}Sr$, $\delta^{88/86}Sr$, $\delta^{41}K$, $\delta^{34}S$, and volumetric discharge at the nearby Mission gauging station.

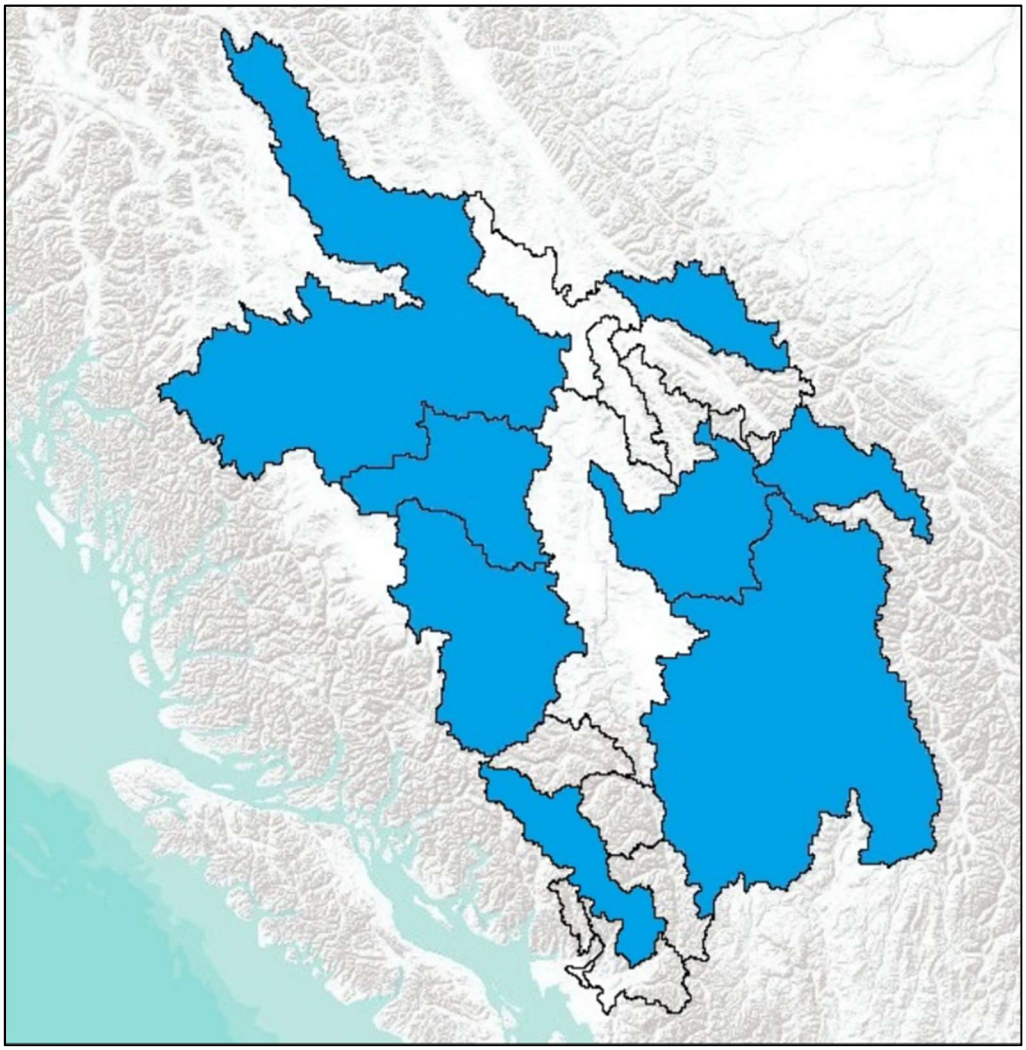

Figure 4 | Map of tributary drainage basins in the Fraser River watershed. Blue represents monitored basins that are characterized with respect to discharge. Those with no coloration are unmonitored and not sampled. Figure adapted from Voss *et al.* (2014).

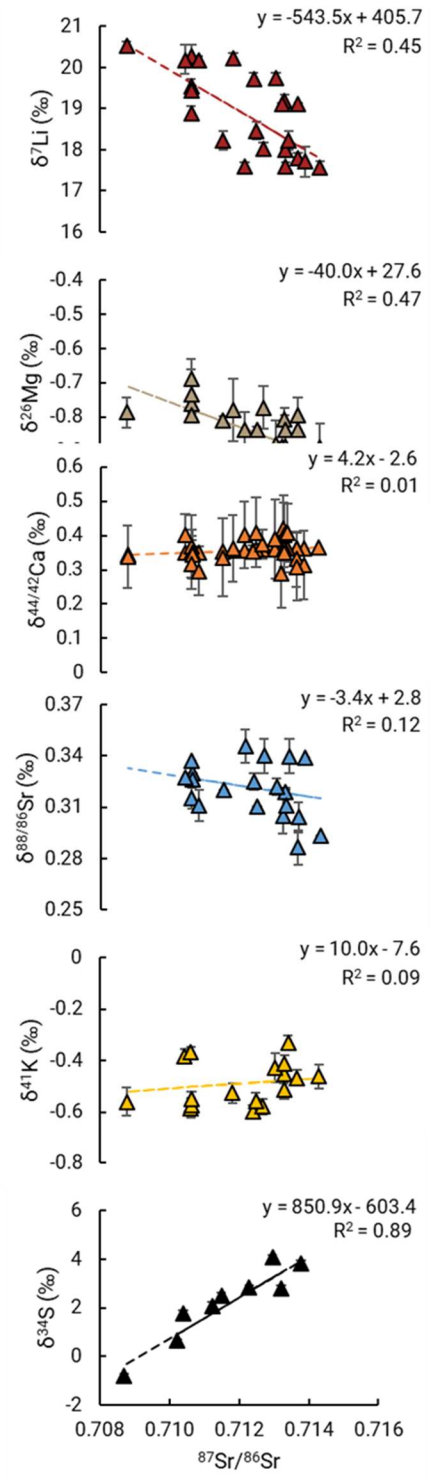

Figure 5 | Non-traditional stable isotope data relative to $^{87}Sr/^{86}Sr$ in the Fraser River main stem at Fort Langley. Error bars represent analytical uncertainty (2SD) and trendlines represent Type II linear regressions.

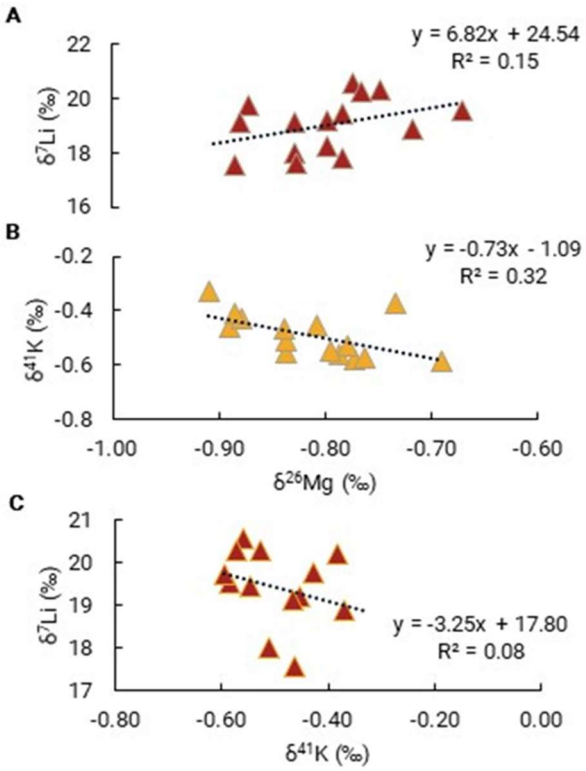

Figure 6 | Relationships between the non-traditional stable isotopes in the Fraser main stem (A) δ^{7}Li vs. δ^{26}Mg **(B)** δ^{41}K vs. δ^{26}Mg **(C)** δ^{41}K vs. δ^{7}Li. Trendlines are Type I linear regressions.

Table 1. Element concentrations and isotopic compositions in Fraser River water samples

Date mm/dd/yyy	Original Sample ID	Standardized Sample ID	Discharge m^3s^{-1}	Li $\mu mol\ L^{-1}$	Mg $\mu mol\ L^{-1}$	K $\mu mol\ L^{-1}$	Ca $\mu mol\ L^{-1}$	Sr $\mu mol\ L^{-1}$	SO_4 $\mu mol\ L^{-1}$	δ^7Li ‰	2SD	$\delta^{25}Mg$ ‰	2SD	$\delta^{44/42}Ca$ ‰	2SD	$\delta^{88/86}Sr$ ‰	2SD	$^{87}Sr/^{86}Sr$ Voss et al., 2014 & This Study	$\delta^{34}S$ ‰	2SD	$\delta^{41}K$ ‰	2SD
			Environment Canada	This Study	Voss et al., 2014					This Study									Burke et al., 2018		Wang et al., 2020	
02/23/2010	TSFRA004	GRO000082	1015	0.11	161	26.9	447	1.03	112	19.5	0.18	-0.69	0.06	0.37	0.09	0.315	0.006	0.71040	-	-	-0.58	0.04
04/13/2010	TSFRA007	GRO000085	1474	0.09	179	24.0	435	1.00	88	20.3	0.26	-0.76	0.01	0.35	0.05	0.330	0.004	0.71042	-	-	-0.57	0.02
05/07/2010	TSFRA009	GRO000086	2958	0.09	133	20.5	403	0.92	71	19.7	0.13	-	-	0.35	0.02	0.325	0.005	0.71203	-	-	-0.60	0.02
05/28/2010	TSFRA023	GRO000089	5089	0.09	116	17.5	368	0.85	64	19.2	0.14	-0.81	0.03	0.42	0.10	0.319	0.002	0.71285	-	-	-0.45	0.04
06/04/2010	TSFRA025	GRO000090	5769	0.12	97	16.6	327	0.76	59	17.8	0.12	-0.80	0.05	0.33	0.09	0.287	0.010	0.71319	-	-	-	-
06/18/2010	TSFRA031	GRO000094	6593	0.08	101	14.9	335	0.79	66	19.1	0.04	-0.89	0.01	0.29	0.10	0.305	0.0100	0.71279	-	-	-	-
07/20/2010	TSFRA038	GRO000100	4700	0.10	91	15.9	310	0.78	76	17.7	0.37	-	-	0.31	0.10	0.339	0.0100	0.71338	-	-	-	-
09/13/2010	TSFRA046	GRO000108	2068	0.11	127	18.8	393	0.94	90	17.6	0.17	-0.89	0.07	-	-	0.293	0.0100	0.71377	3.90	0.13	-0.46	0.05
09/27/2010	TSFRA047	GRO000109	2402	0.10	126	21.5	372	0.91	91	18.0	0.02	-0.84	0.04	0.40	0.09	-	-	0.71286	-	-	-0.51	0.04
11/01/2010	TSFRA049	GRO000112	1949	0.04	136	19.8	399	0.94	88	19.1	0.04	-0.84	0.02	0.31	0.10	0.304	0.009	0.71320	2.90	0.11	-0.47	0.03
11/15/2010	TSFRA050	GRO000114	1865	0.08	135	19.9	392	0.92	88	19.7	0.11	-0.88	0.07	0.39	0.12	0.322	0.005	0.71262	-	-	-0.43	0.06
12/09/2010	TSFRA051	GRO000115	1310	0.06	157	23.6	423	1.00	97	20.3	0.09	-0.78	0.09	0.36	0.10	-	-	0.71150	2.51	0.10	-0.53	0.04
12/16/2010	TSFRA052	GRO000116	1423	0.11	124	24.0	347	0.83	84	19.4	0.03	-0.80	0.01	0.34	0.07	0.326	0.004	0.71042	-	-	-0.55	0.03
01/20/2011	TSFRA053	GRO000118	1258	0.09	101	21.4	295	0.70	71	20.6	0.07	-0.79	0.04	0.34	0.09	-	-	0.70870	-0.81	0.11	-0.56	0.05
02/24/2011	TSFRA055	GRO000123	1022	0.07	150	22.7	418	0.98	99	20.2	0.36	-	-	0.40	0.06	0.327	0.0100	0.71023	0.64	0.07	-0.38	0.03
04/19/2011	TSFRA097	GRO000127	1601	0.08	168	25.4	440	1.04	88	18.9	0.17	-0.73	0.07	0.32	0.07	0.337	0.0100	0.71040	1.77	0.11	-0.37	0.02
05/10/2011	TSFRA083	GRO000130	3929	0.09	149	-	385	0.88	53	20.2	0.07	-	-	0.30	0.07	0.311	0.009	0.71059	-	-	-	-
05/20/2011	TSFRA085	GRO000132	7819	0.09	140	20.6	402	0.91	50	18.2	0.23	-0.81	0.01	0.34	0.11	0.320	0.0100	0.71123	2.06	0.16	-	-
06/03/2011	TSFRA090	GRO000135	9904	0.11	122	18.8	369	0.87	49	17.6	0.09	-0.84	0.05	0.40	0.10	0.346	0.0100	0.71180	-	-	-	-
06/28/2011	TSFRA128	GRO000140	10020	0.09	115	16.8	357	0.86	56	18.2	0.16			0.34	0.05		0.0100		3.45	0.17	-	-
07/15/2011	TSFRA100	GRO000143	9750	0.03	112	15.9	370	0.87	51	18.22	0.23	-0.91	0.01	0.41	0.09	0.340	0.010	0.71296	4.06	0.10	-0.33	0.03
08/26/2011	TSFRA105	GRO000150	4521	0.04	127	20.9	381	0.91	70	18.02	0.14	-0.77	0.06	0.37	0.04	0.340	0.010	0.71229	2.92	0.09	-0.58	0.03
09/09/2011	TSFRA106	GRO000152	2855	0.04	138	19.0	412	0.97	76	17.60	0.09	-0.89	0.04	0.35	0.06	0.311	0.009	0.71287	-	-	-0.41	0.03
10/25/2011	TSFRA111	GRO000157	2255	0.03	143	19.3	395	0.92	75	18.46	0.21	-0.84	0.01	0.41	0.10	0.310	0.0100	0.71211	-	-	-0.56	0.03
08/09/2009	09FRA21CHIL	GRO000021	251	2.8	58	18	218	0.54	63	24.16	0.22	-0.70	0.02	0.37	0.08	0.361	0.0100	0.70431	-	-	-	-
10/20/2010	CHIL GRO00043	GRO000043	98	2.4	99	19	227	0.66	70	23.0	0.18	-0.53	0.06	0.36	0.07	0.341	0.0100	0.70439	-	-	-	-
05/29/2011	11FRA07CHIL	GRO000059	217	5.0	349	56	392	1.01	48	22.2	0.20	-0.43	0.04	0.48	0.09	0.341	0.0100	0.70454	-	-	-	-
08/03/2009	09FRA09	GRO000009	85.3	10.6	211	5	229	0.55	176	13.24	0.08	-	-	0.45	0.05	0.318	0.0100	0.75155	-	-	-	-
10/14/2010	10FRA02	GRO000027	35.8	14.4	308	6	362	0.79	255	12.37	0.45	-	-	0.37	0.04	0.326	0.0100	0.74553	-	-	-	-
06/03/2011	11FRA21	GRO000073	169	9.7	209	4	256	0.54	148	13.60	0.40	-	-	0.40	0.10	0.346	0.0100	0.71180	-	-	-	-

Data compilation from this study, where the bulk of data are for the Fraser main stem at Fort Langley and lower sections of data ($n = 3$) are for the Chilcotin and Fraser at Fitzwilliam sampling sites, respectively. 'Standardized Sample ID' refers to the sample identification number in the SESAR catalog, available at: https://www.geosamples.org/search.

Table 2. Endmember Characterizations

Parameter	Coast Range	Rocky Mountains	'Missing'
[Li] (μM)	0.1 ± 0.1	0.2 ± 0.1	0.1
$\delta^{7}Li$ (‰)	23 ± 2	13 ± 1	20
[Mg] (μM)	186 [+273, -186]	193 ± 107	187
$\delta^{26}Mg$ (‰)	-0.56 ± 0.27	*-1.68	-0.75
[Ca] (mM)	0.3 ± 0.2	0.4 ± 0.3	321
$\delta^{44/42}Ca$ (‰)	0.40 ± 0.13	0.40 ± 0.08	0.40
[Sr] (μM)	0.7 ± 0.5	0.85 ± 0.7	1
$^{87}Sr/^{86}Sr$	0.7046 ± 0.0007	0.732 ± 0.027	0.70975
$\delta^{88/86}Sr$ (‰)	0.35 ± 0.01	0.32 ± 0.01	0.343
[K] (μM)	31 ± 36	7 ± 7	27
$\delta^{41}K$ (‰)	*-0.56	*-0.29	-0.55
[SO_4] (μM)	39 ± 38	118 ± 141	53
$\delta^{34}S$ (‰)	**-0.9 ± 3.9	**10.7 ± 4.5	0.86

Characterizations of the Coast Range and Rocky Mountain endmembers, with uncertainties representative of 2SD in the tributary values that were averaged to produce these endmember values. The composition of the 'missing' is based on 83% Coast Range and 17% Rocky Mountains contributions.
* $\delta^{26}Mg$ and $\delta^{41}K$ values calculated from Type II linear regressions (Fig. 4) with $^{87}Sr/^{86}Sr$, since no observational data were available
**Values from Cameron *et al.* (1995)

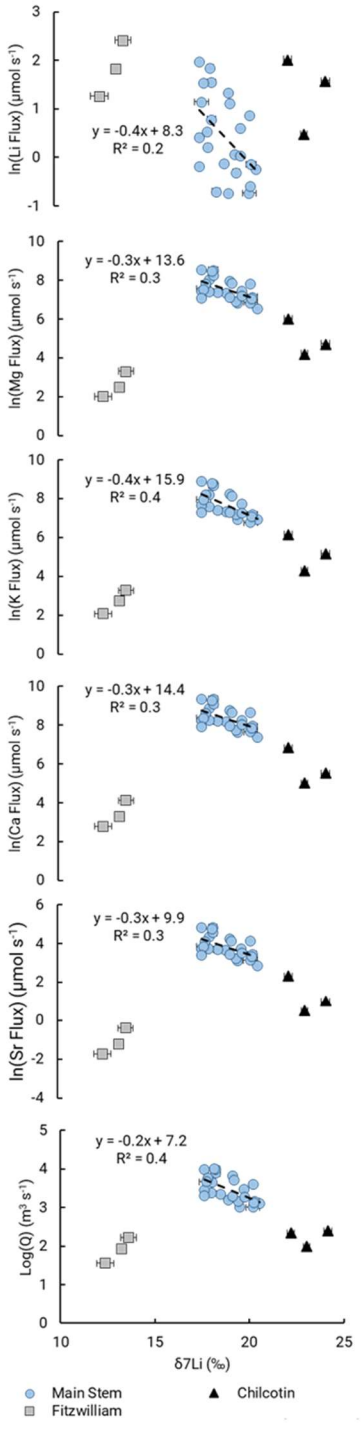

Figure 7 | Relationships between δ^7Li and the natural log of silicate weathering-derived solute fluxes for (top to bottom) Li, Mg, K, Ca, and Sr, as well as the Log of discharge (Q) in the Fraser River main stem, upper Fraser River at Fitzwilliam, and Chilcotin tributary. Trendlines represent Type I linear regressions.

Table 3. Silicate weathering-derived cation fluxes

Date	Discharge	Li	Mg	Ca	Sr	K
mm/dd/yyyy	$m^3 s^{-1}$	$\mu mol\ s^{-1}$	$mmol\ s^{-1}$	$mmol\ s^{-1}$	$\mu mol\ s^{-1}$	$mmol\ s^{-1}$
01/20/2011	1258	0.8	0.72	1.57	17	1.01
02/24/2011	1022	0.5	0.97	2.13	23	0.87
02/23/2010	1015	0.7	0.94	2.07	23	1.02
04/19/2011	1601	0.9	1.61	3.54	39	1.54
04/13/2010	1474	0.9	1.29	2.83	31	1.33
12/16/2010	1423	1.1	1.04	2.29	25	1.30
05/10/2011	3929	2.4	2.59	5.70	62	-
05/20/2011	7819	4.7	5.18	11.38	124	6.21
12/09/2010	1310	0.6	1.17	2.57	28	1.16
06/03/2011	9904	7.2	5.24	11.52	126	7.14
05/07/2010	2958	1.8	1.76	3.87	42	2.30
10/25/2011	2255	0.5	1.67	3.67	40	1.65
08/26/2011	4521	1.2	3.19	7.01	77	3.62
11/15/2010	1865	1.0	1.38	3.04	33	1.42
06/18/2010	6583	3.8	2.93	6.43	70	3.77
05/28/2010	5089	3.1	2.60	5.71	62	3.40
09/27/2010	2402	1.7	1.71	3.75	41	1.98
09/08/2011	2855	0.8	1.76	3.88	42	2.08
07/15/2011	9750	2.2	3.94	8.67	95	5.94
06/04/2010	5769	4.7	2.51	5.52	60	3.68
11/01/2010	1949	0.5	1.28	2.80	31	1.46
07/20/2010	4700	3.1	1.93	4.23	46	2.86
09/13/2010	2068	1.5	1.23	2.70	30	1.48
06/28/2011	10020	6.4	4.85	10.65	116	6.45

Silicate weathering-derived cation fluxes calculated using a forward modeling approach.

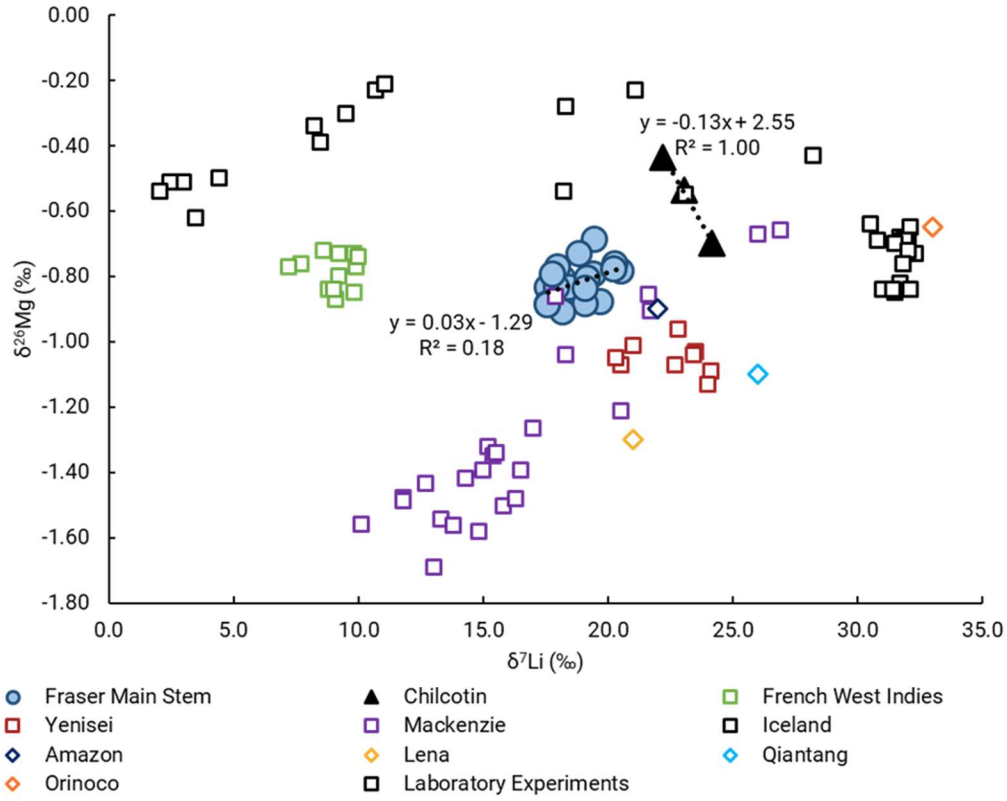

Figure 8 | The Fraser River main stem and Chilcotin tributary samples in a global context. Fraser River basin data is plotted relative to samples from the French West Indies (Fries *et al*., 2019), Yenisei (Hindshaw *et al.*, 2019), Mackenzie River (Millot *et al.*, 2010; Tipper *et al*., 2012), and four other major world rivers (Amazon, Qiantag, Lena, and Orinoco; Tipper *et al*., 2012). Also shown are the results of solutions from laboratory experiments on basalts and forsterite (Wimpenny *et al*., 2010). Linear trendlines represent Type I regressions.

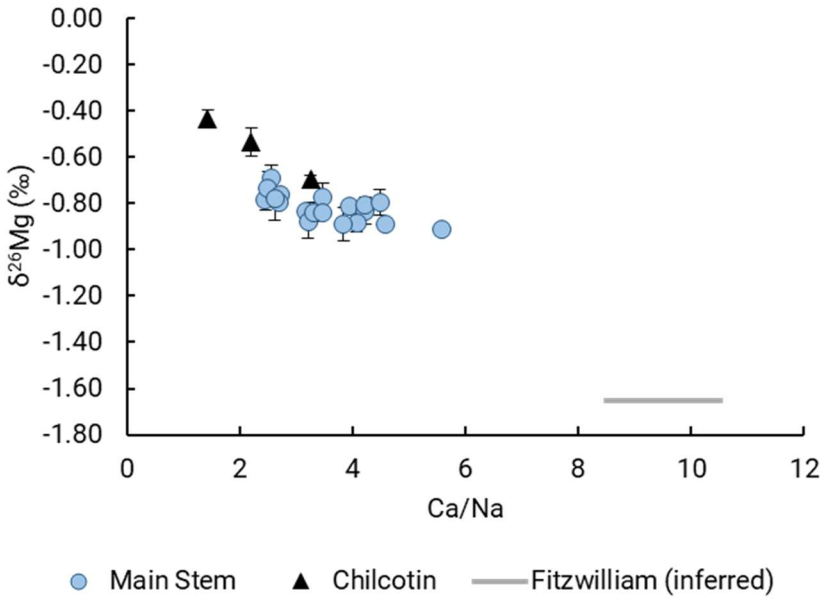

Figure 9 | δ^{26}Mg and Ca/Na ratios observed in the Fraser River main stem values fall between values of the isotopically "heavier", less carbonate-influenced Chilcotin tributary and the more carbonate-influenced Rocky Mountains-draining upper Fraser River at Fitzwilliam. The Fitzwilliam value is estimated to be -1.65‰ based on the Type II linear regression results presented in Fig. 4. This value was also used in the isotope mixing model to represent the Fitzwilliam endmember.

Chapter 4

Barium Cycling in the Gulf of Aqaba:

An Exceptionally Undersaturated Marine Basin for Barite

Abstract

Stable Ba isotopes ($\delta^{138}Ba$) are a novel proxy in oceanography thought to improve our understanding of deep-ocean circulation, water mass provenance, and the oceanic Ba cycle. The $\delta^{138}Ba$ signatures of Ba inputs to the ocean and the formation of barite ($BaSO_4$) in seawater, a major Ba sink, control the $\delta^{138}Ba$ of seawater and, hence, it is crucial to understand the processes that affect these source and sink signatures. In this study, I investigated the influence of export productivity, barite saturation state (Ω_{barite}), and terrigenous inputs (e.g. aerosols) on the $\delta^{138/134}Ba$ composition of suspended particulates. I use sinking particulate matter and seawater samples collected seasonally in the world's most undersaturated marine basin with respect to barite – the Gulf of Aqaba. The $\delta^{138}Ba$ of particles exported to depth was invariant in this sample set (+0.09 ± 0.06 ‰, 2 SD; n=26), despite changes in P and Al fluxes, which are used to represent changes in productivity and dust fluxes. The offset between suspended particulates and seawater ($\Delta^{138}Ba_{particle\text{-}seawater}$) in the Gulf of Aqaba is -0.5 ± 0.1 ‰, consistent with observations from other sites and studies, corresponding to a wide range of barite saturation states, where Ω_{barite} ranges from 0.02 – 1. I interpret these results to indicate that $\Delta^{138}Ba_{particle\text{-}SW}$ is insensitive to barite saturation state and is solely driven by the $\delta^{138}Ba$ composition of the surficial water mass from whence the barite formed. Aerosol $\delta^{138}Ba$ analysis yielded a $\delta^{138}Ba$ composition of 0.01 ± 0.03 ‰, while recent and preindustrial bottom sediments have a uniform $\delta^{138}Ba$ signature of 0.34 ± 0.03 ‰. This relatively heavy $\delta^{138}Ba$ composition of the sediments, compared to both aerosols and the sinking particulate load, indicates that some post deposition diagenetic process that involves

isotopic fractionation or a yet unconstrained source of isotopically heavy Ba is affecting the sedimentary δ^{138}Ba signature.

Introduction

Ba isotopes have been proposed as a valuable oceanographic proxy for water mass provenance and deep-ocean circulation (Bates et al. 2017; Geyman et al. 2019; Horner et al. 2017). This application is based on the observed distribution of δ^{138}Ba in seawater, which is affected by the precipitation of barite ($BaSO_4$) in seawater and the isotopic fractionation involved in the process (e.g. Bates et al. 2017; Horner, Kinsley, and Nielsen 2015; Hsieh and Henderson 2017). Specifically, it has been suggested that the longer a water mass remains in the upper ocean (~200 – 700 m) before it is downwelled, the longer it has for isotopically lighter Ba to be removed by barite formation/export, rendering the dissolved δ^{138}Ba composition of the water mass proportionately heavier. The δ^{138}Ba composition of the surficial water mass, which is controlled by the duration of time at the surface and the intensity of barite formation, is purported to control the δ^{138}Ba composition of sediments (Bates et al. 2017; Horner et al. 2017). However, the effect of different factors that influence barite accumulation in sediments – namely, export productivity, barite saturation state (Ω_{BaSO4}), and inputs of terrigenous material (e.g. aerosols) on the bulk δ^{138}Ba of marine sediments or on δ^{138}Ba of barite in sediments are currently unknown.

To date, the natural Ba isotopic variability of the ocean has been measured in the Atlantic (Bates et al. 2017; Horner, Kinsley, and Nielsen 2015; Hsieh and Henderson 2017), Pacific (Geyman et al. 2019; Hsieh and Henderson 2017), China Sea (Cao et al. 2020), and Southern Ocean (Hsieh and Henderson 2017). All marine studies have documented that Ba has a nutrient-like profile with barite precipitation in upper ocean (~200-700 m) micro-environments driving its isotope fractionation within the oceanic water column. The prevailing hypothesis is that, as heterotrophic microbes remineralize sinking organic matter, the lighter isotopes of Ba (Von Allmen, et al., 2010; Horner, et al., 2015) are preferentially incorporated into the mineral $BaSO_4$. This process renders meso-pelagic waters

relatively depleted in Ba concentrations and isotopically "heavier" than the water masses above and below (Bates et al. 2017; Horner, Kinsley, and Nielsen 2015; Hsieh and Henderson 2017). Water masses that form at these depths and circulate throughout the ocean likely preserve their pre-formed Ba isotopic composition (Bates et al. 2017). It is assumed that barite dissolution during sinking minimally affects the dissolved δ^{138}Ba composition of seawater, although Ba concentrations increase with water mass age along the oceanic conveyor belt (Bates et al. 2017; Horner, Kinsley, and Nielsen 2015; Hsieh and Henderson 2017). Thus, the dissolved Ba isotopic values in seawater and, potentially, in marine sediments are predominantly controlled by ocean circulation patterns, which are an integration of the Ba isotopic composition of surface waters and the intensity of barite formation in the region where the water mass originated (Bates et al. 2017; Bridgestock et al. 2018).

Barite accumulation rates in marine sediment records depend primarily on export production, which depends on climatic changes that effect nutrient supply and is the basis for its application as a paleo-proxy for export productivity (Eagle et al. 2003; Paytan, A & Kastner 1996). However, barite accumulation rates in marine sediments are also sensitive to preservation in marine sediments, which is a function of the Ω_{BaSO4} in overlying seawater/porewaters (Eagle et al. 2003), and inputs of insoluble terrigenous material (Anderson and Winckler 2005). The introduction of insoluble material is problematic for estimation of barite accumulation rates for two reasons; first, since the sequential leaching process used to quantify barite accumulation assumes that the mass of a residual fraction is barite, the presence of insoluble terrigenous detritus can artificially increase the remnant mass in the 'barite fraction' of the sediment, unless accounted for by electron microscopic observations or by measuring the Ba in the residual fraction (Eagle et al. 2003; Ma et al. 2015). Furthermore, inconsistent terrigenous inputs can affect the sediment accumulation rates and, consequently, the age model upon which barite accumulation rates are based (Anderson and Winckler 2005). The effect that these variables – specifically, export productivity, Ω_{BaSO4} of seawater, and terrigenous inputs – may have on Ba isotopes in marine sediments, however, is unconstrained. Thus, to test the Ba isotope system in a marine environment that experiences a range of these environmental conditions, this study was conducted in the Gulf of Aqaba (GOA).

Geographic and geologic setting

Terrigenous inputs of Ba to the ocean can be categorized into dissolved and solid forms. The GOA is surrounded by arid deserts and lacks riverine discharge; hence, dissolved sources of Ba are confined to limited groundwater discharge (Shellenbarger et al., 2006) and occasional (< 5 per year) flash flood events, which do not noticeably impact the water column chemistry (Katz et al. 2015). Solid terrigenous sources include atmospheric dust deposition and flash flood-transported sediments. The origin of dust inputs to the GOA vary seasonally, but are generally derived from desert regions surrounding the gulf, such as the Sahara, Negev, and Arabian deserts (Chen et al. 2007; 2008). Relative to annual dust fluxes (~28 g m^{-2} yr^{-1}), which are some of the highest in the world, flash flood events transport an order of magnitude more solid mass to the GOA (~830 g m^{-2} yr^{-1}), but the material arrives in discrete events and is quickly deposited, not lingering in the water column (Katz et al. 2015; Torfstein and Kienast 2018). In this study, I assume that mineral dust and flash flood-transported sediments have a common chemical composition, since the flash floods essentially transport surficial sediments of aeolian origin from the surrounding region to the GOA (Katz et al. 2015).

Oceanographic setting

The GOA is the northernmost extension of the Red Sea (Fig. 1), which is the most undersaturated marine basin in the world with respect to barite ($\Omega_{barite} < 0.3$) (Monnin et al. 1999). This undersaturation is driven by warm sea surface temperatures (20 – 29°C; Fig. 2) and a lack of fluvial Ba inputs. The only marine source of dissolved Ba to the GOA is the narrow Straits of Tiran, through which surface water from the Red Sea waters enter the GOA and deeper waters leave the basin. The GOA is ~180 km long and ~800 m deep, with an average water residence time of ~7 years (Silverman and Gildor 2008). Its oceanographic seasonality can be parsed into two distinct seasons: highly stratified, summer months (April – September) and well-mixed, winter months (October – March) (Fig. 2) (Silverman and Gildor 2008). During the summer, hot sea surface temperatures lead to intense stratification, which minimizes mixing and causes photic zone waters to become oligotrophic (NO_3^- < 200 nM and PO_4^{-3} < 60 nM), thereby minimizing Chl-*a* concentrations (Chl-*a* ~0.1 μg/L) (Labiosa et al. 2003; Lindell and Post 1995). As temperatures cool, however, deep mixing (~300 – 400 m) is

facilitated, bringing nutrients to the surface and Chl-*a* increases by approximately an order of magnitude (Chl-*a* > 1 µg/L) (Labiosa et al. 2003; Lindell and Post 1995). Primary productivity rates between these two seasons can vary by a factor greater than five, between 200 – 1120 mg C m^{-2} d^{-1} (Levanon-Spanier, Padan, and Reiss 1979).

Nutrient inputs to the GOA have increased over the recent past (~70 y) as humans continue to populate the region surrounding the GOA (Lazar et al. 2008). These changes have led to increased regional primary production rates due to wastewater and fish farm-derived N inputs (Lazar et al. 2008), which is further supported by observed organic C increases in sediment archives from the GOA (Steiner et al. 2017). However, conventional Ba-based paleo-productivity proxies (e.g. sedimentary Ba or $BaSO_4$ accumulation rates or Ba/Al ratios) were not found to correlate with trends in organic C burial (Steiner et al. 2017). This was due, in part, to the abundance of detrital aeolian inputs, which complicate estimates of the biogenic Ba fraction (Anderson and Winckler 2005; Steiner et al. 2017).

The low barite saturation state, range in primary productivity rates, and complications in the use of traditional Ba-based productivity proxies make the GOA an ideal natural laboratory for evaluating the utility or potential limitations of Ba isotopes as a proxy for Ba sources and cycling in the ocean. In this study, I examine the Ba isotopic composition of GOA seawater (dissolved and particulate), in conjunction with aerosol, groundwater, and sediment samples, to determine what controls the δ^{138}Ba composition of GOA sediments.

Materials and Methods

This study builds upon the Israel National Monitoring Program for the Gulf of Eilat (Shaked and Genin 2018) and the Red Sea Dust, Marine Particulates and Seawater Time Series (REDMAST) sampling campaign (Torfstein et al. *in revision*), which consists of coeval seawater and sediment trap profiles at 'Station A' (29° 28.95' N, 34° 56.22' E), as well as aerosol collection at the Interuniversity Institute (IUI) for Marine Sciences in Eilat (Fig. 1). Sampling is conducted on an approximately weekly basis for all three parameters, which makes this basin especially well-monitored. Seawater

profiles for dissolved constituents are sampled according to the 'GEOTRACES Cookbook' protocols – an internationally agreed-upon protocol for sampling seawater for trace element analyses (Cutter et al. 2010). Seawater samples were collected acid cleaned Teflon coated GO-Flo bottles (General Oceanics) and transported to the IUI clean lab facility within 1 – 2 hours. At the lab, samples were filtered through an acid cleaned Acropak 500 0.8/0.2 μm Supor sterile cartridge, acidified using trace metal clean 6N HCl to a pH of <2, and stored refrigerated in polypropylene vials.

Sediment trap profiles were collected using the collection and processing methods detailed in Chernihovsky et al. (2018). In brief, the sediment traps were deployed between January 2014 and February 2016 at Station A (Fig. 1). The traps (KC Denmark A/S) were deployed at five depths: 120, 220, 340, 450 and 570 m. To minimize sample degradation during deployment, the traps were filled with a poisoned ($HgCl_2$), saturated brine. Post-retrieval, suspended particles were settled and effluent was partially decanted before sieving through a 1 mm sieve to remove large organisms. The residue (<1 mm) was rinsed three times with Milli-Q (ultrapure) water to remove salts, freeze-dried, and weighed. A split of the sample was wet sieved through a series of stainless-steel sieves (500, 125 and 63 μm mesh) and freeze-dried again. The size fraction utilized in this study was the <63 μm, since barite (the primary phase of particulate Ba in the water column) is generally less than 3 μm in size (Griffith and Paytan 2012; Horner et al. 2015).

Subsampling for this study was designed to include samples that span the largest N isotope range – an identifier of primary production shifts in the Gulf (Wankel et al. 2010). This subsampling strategy is expected to maximize the range of biologically driven seasonality in Ba cycling. In addition to marine samples, two aerosol and one coastal groundwater sample were collected as a means of characterizing terrigenous inputs to the system. The aerosol samples were from August of 2015 and January of 2016, collected as a part of studies conducted by Hartman et al. (2020) and Chien et al. (2019), respectively. The 2015 aerosol sample was collected using a total suspended particulate sampler attached to a five-meter-long pole on the roof of the IUI. The 2016 aerosol sample was collected during a dust storm from an air filter at the IUI. The groundwater sample was collected in August of 2017 from a coastal well on the IUI campus, approximately 3 m from the high tide line and

approximately 1.5 m deep, as a part of this study. The salinity of the groundwater sample was, however, indistinguishable from local seawater and its δ^{138}Ba ratio was reported in Mayfield *et al.* (2020).

Finally, a sediment core was retrieved at Station A (Fig. 1), using a MC-400 four-barrel multi-corer (Ocean Instruments, San Diego, CA) from a depth of ~720 m. Two core samples were analyzed, from depths of 2 – 5 cm and from 31 cm. A well-dated sediment core from the same location (Steiner et al., 2017) constrains the age of these samples to have been deposited during the years ~1970-2000 and the mid-18th century, respectively. Thus, these samples represent the anthropogenic and pre-industrial sedimentary endmembers, respectively.

Chemical Preparation

All sample preparation was conducted at the IUI clean lab (1000 class with 100 class workstations) using double-distilled acids. The seawater particulate and aerosol samples were prepared identically to one another, where ~5 mg of material was dissolved in bulk with 1 mL of aqua regia at 120°C overnight, dried down, then further dissolved in 2 mL of a HF + HNO_3 mixture at 120°C overnight, and dried down again. Dried down samples were reconstituted with 1 mL of 1M HNO_3 and transported, alongside the groundwater and seawater samples, to Woods Hole Oceanographic Institution, where they were analyzed for Ba concentration and δ^{138}Ba composition. Suspended particulate samples were also analyzed for their P and Al concentrations, which I use as qualitative proxies for organic matter and terrigenous dust inputs, respectively.

The sediment core samples were processed via a sequential leaching procedure designed to quantitatively separate barite from the sediment, described in Paytan and Kastner (1996). This sequential leaching procedure was performed on ~15 g of sediment for each sample and includes reactions with acetic acid, sodium hypochlorite, hydroxylamine, and an HF-HNO_3 mixture. Each of these leaching steps was intended to dissolve specific sedimentary fractions, namely the carbonate, organic matter, Fe-Mn oxyhydroxide, and silicate fractions, respectively. The final residue was expected to be comprised of barite and other refractory minerals. However, due to high inputs of insoluble terrigenous material (e.g. aeolian dust and flood deposits) in the GOA, relative to open ocean

sediments, the non-barite component constituted a large fraction of the samples. Scanning electron microscopy showed that the sediment samples had an abundance of minerals that were not digested (Fig. 3). To remove at least some of this detrital terrigenous material, the post-leaching sediment fraction was wet sieved to collect the < 20µm size fraction. The < 20µm size fraction was assumed to have contain all the barite, whose crystals are generally < 3 µm. This < 20µm 'barite containing fraction' of sediment was analyzed in this study and is assumed to represent the primarily the barite signature as this is the mineral where much of the Ba resides.

Barium Analyses

Post preparation at IUI, all samples were transferred to the NIRVANA Labs at Woods Hole Oceanographic Institution (WHOI). Reagents used in the chemical and analytical procedures were distilled to Optima-grade standards. All samples were analyzed for their Ba, Al, and P concentrations on a Thermo Scientific iCAP Qc quadrupole inductively coupled plasma mass spectrometer (ICPMS). Samples were then prepared for Ba isotope analysis using the method described by Mayfield *et al.* (2020). In brief, all samples were spiked with a ^{135}Ba–^{136}Ba double spike solution, aqueous samples were co-precipitated with Ba-free 1 M Na_2CO_3 solution, Ba was separated from sample matrices using gravimetric column chemistry, and the purified samples were analyzed in low resolution mode at the WHOI Plasma Facility using a Thermo Finnigan Neptune MC-ICP-MS. A spiked standard—NIST SRM 3104a—was measured every fifth samples and sample isotopic data are reported relative to the nearest four analyses of NIST SRM 3104a using the δ notation:

$$\delta^{138}Ba\ (‰) = [(^{138}Ba/^{134}Ba)_{sample} / (^{138}Ba/^{134}Ba)_{SRM\text{-}3104a} - 1]$$

Analytical precision is reported as the greater of either long-term 2 SD reproducibility (± 0.03 ‰; Horner et al., 2015) or the measured 2 SE obtained from replicate analyses (i.e., where *n* was between 2–8).

Results

Seawater Ba Profiles

Dissolved seawater Ba concentrations [Ba] span a narrow range between 44 – 56 nM, with δ^{138}Ba values between +0.46 and +0.63 ‰ (Fig. 4; Table 1). The [Ba] and δ^{138}Ba trends observed in the GOA seawater overlap with results from other oligotrophic, open ocean basins (Fig. 5). Samples representing the two seasons analyzed in this study were similar, with an average δ^{138}Ba composition of +0.56 ± 0.08 ‰ (2SD) (Fig. 4).

Particulate Profiles

Particulate fluxes of Ba, P, and Al varied considerably between months in the time series, ranging from 0.2, 1.6, and 16 mg d^{-1} m^{-2} to 1.5, 12.5, and 256 mg d^{-1} m^{-2}, respectively (Fig. 6; Fig. 7; Table 2). The highest fluxes of Al and P were observed between November of 2015 and March of 2016, coincident with the highest flux of particulate Ba. The Ba isotopic composition of the particulates in the sediment trap, however, did not differ significantly across the time series (Fig. 6). The average δ^{138}Ba composition of the particulate matter was +0.09 ± 0.06 ‰ (2SD) (Fig. 6; Table 2). This isotopic composition displayed no discernable relationship to the Ba flux. Furthermore, the isotopic compositions of all sinking particulate samples analyzed in this study were consistently lighter than the isotopic signature of the dissolved Ba in seawater by ~0.5 ‰ (Fig. 8).

Terrigenous Inputs

In this study, I define terrigenous inputs of Ba as those associated with groundwater discharge and aeolian inputs. The groundwater sample analyzed had a salinity similar to the local seawater (39). Its δ^{138}Ba composition (+0.49 ‰) was also within the range measured for seawater samples, but at the low end of the seawater range (Fig. 8; Table 1). The groundwater Ba concentration, however, was higher than seawater (113 nM, relative to ~45 nM). The August 2015 aerosol samples had been previously characterized in Chien et al. (2019), who reported that bulk Ba concentrations in the aerosol were ~140 ppm, 16-26% of which was soluble (Chien *et al*., 2019). This 140 ppm Ba value is within the range of 0 – 200 ppm Ba that most dust samples collected over a four year time series exhibited

(Torfstein et al. 2017). The isotopic compositions of both dust samples, despite their difference in collection date, were within analytical uncertainty of each other and had an average composition was +0.01 ‰ (Table 2).

Marine Sediments

The $\delta^{138}Ba$ compositions of two marine sediment samples, deposited at Station A during the late 20th and mid-18th centuries, were within analytical uncertainty of each other. Their average isotopic composition was +0.34 ± 0.04 ‰ (2SD) (Table 2; Fig. 8). This isotopic composition was distinctly heavier than all suspended particulates and aerosol samples analyzed in this study (Fig. 8).

Discussion

Water Mass Effects

Relative to deeper, open ocean basins with numerous water masses of vastly different ages layering atop one another, the water column of the GOA is more uniform. This uniformity can be attributed to two key variables: its physical circulation, with a singular inflow source and deep seasonal mixing (Biton and Gildor 2011; Silverman and Gildor 2008), as well as its relatively low productivity rates due to oligotrophy (Chernihovsky, et al. 2018; Foster, Paytan, and Zehr 2009; Labiosa et al. 2003). This homogeneous chemical composition with respect to Ba simplifies the calculation of a single $\delta^{138}Ba_{seawater}$ value (+0.56 ‰), which is necessary for the calculation of an isotopic offset between seawater and suspended particulates ($\Delta^{138}Ba$).

Chemistry of the Ba Export Flux

The particulate P and Al fluxes reported in this study are intended to qualitatively represent fluxes of organic matter and terrigenous particulate matter, respectively. Particulate P fluxes were high during late winter – early spring months (January, February, and March), which corresponds to elevated Chl-a concentrations in Station A surface waters and expected higher productivity from increased nutrient availability, driven by enhanced vertical mixing (Fig. 3) (Labiosa et al., 2003; Lindell and Post, 1995). Particulate Al fluxes were high during the same early months of 2016,

overlapping with high dust inputs during that time period, reported in Torfstein and Kienast (2018). While high Ba fluxes coincided with both Al and P high fluxes (Fig. 7a, b), the δ^{138}Ba isotopic composition of the exported particulate load was invariant over time and did not correspond to the total particulate Ba flux (Fig. 7c). The δ^{138}Ba composition of the export load remained consistent throughout the time series, with an average δ^{138}Ba composition of +0.09 ‰ ± 0.06 ‰ (2SD).

To calculate an isotopic offset of the particulate load from dissolved seawater in the GOA, the average seawater value was subtracted from the average particulate value, which yielded a Δ^{138}Ba ($\delta^{138}Ba_{particulate}$ - $\delta^{138}Ba_{seawater}$) of -0.47 ‰ ± 0.08 ‰. This value is comparable to previously reported Δ^{138}Ba offsets in Bates et al. (2017), Horner et al. (2017), and Middleton et al. (*In Prep*) (Fig. 8), suggesting that like at other sites, Ba in the particulate load is dominated by barite. The three previous estimates of Δ^{138}Ba are derived from observations in the Atlantic ($\Omega_{barite} \approx 0.5$), Lake Superior ($\Omega_{barite} \approx 0.02$), and laboratory experiments ($\Omega_{barite} \approx 1$), which span a wide range of settings and barite saturation states. The Δ^{138}Ba calculated in this study, -0.47 ‰, represents the least-saturated marine endmember on this spectrum. The similarity amongst these locations suggest that the isotopic composition of particulate Ba is dominated by barite formation with a constant fractionation factor that is not strongly depended on environmental parameters, such as salinity, temperature, ecosystem structure or saturation levels. This information is important for the potential application of barite δ^{138}Ba for reconstructing ocean processes, since the recorded values in barite could be converted to seawater δ^{138}Ba values by adding the fixed offset.

Barium in Marine Sediments

Given the consistency of the δ^{138}Ba composition in the exported particulate load across the time series, it was expected that the sediments underlying the location of the sediment trap would have the same isotopic composition as the particulates. However, this was not observed; the sediments were isotopically heavier than any of the suspended particulates and aerosol samples analyzed in this study and, therefore, could not be explained solely by a mixture of these two sources. I interpret this to indicate that there is a loss of isotopically lighter Ba from the sediments to the porewater reservoir, likely due to the dissolution of barite after deposition. Porewaters from the core were not analyzed as a

part of this study; however, in a previous study by Steiner et al. (2017), porewaters from a GOA sediment core were analyzed and the upper 2 cm was found to be undersaturated with respect to barite. The porewaters of this undersaturated zone ($\Omega_{barite} < 1$) had Ba concentrations between 200 – 250 nM, while the porewaters below 2 cm had ~250 – 500 nM Ba, which is at or above saturation ($\Omega_{barite} > 1$) (Steiner et al. 2017). It is possible that the increase in barite saturation with depth in the porewaters is driven by the partial or complete dissolution of sedimentary barite and other Ba carrying phases, such as iron and manganese oxides in undersaturated conditions, as previously reported by Paytan & Kastner (1996). In the absence of any Ba isotope data from the porewaters, I consider the coastal groundwater sample to be a first approximation for the chemical composition of marine porewaters, while fully recognizing that porewater $\delta^{138}Ba$ values are the only values that could directly test this hypothesis. The basis for this first-order approximation of groundwater ≈ porewater chemistry is based on the identical salinity to local seawater, combined with the high Ba concentration of the groundwater sample (113 nM), which falls between the seawater (48 nM) and porewater values from Steiner et al. (2017) (Fig. 8). The $\delta^{138}Ba$ composition of coastal groundwater in this study (+0.49 ‰) was isotopically heavier than the sediments, but lighter than the average seawater value (+0.56 ‰) (Fig. 7). If this approximation is accurate, then this supports the hypothesis that there is some release of Ba from partial dissolution of barite and other Ba carrying phases in the sediments, which contributes Ba with isotope values lower than seawater into solution. Previous studies have shown that barite can partially dissolve in the sediments when overlying seawater is undersaturated with respect to barite (e.g. Paytan and Kastner 1996; Riedinger, *et al.*, 2006) and, given that the Red Sea is exceptionally undersaturated with respect to barite (Monnin et al. 1999), this is a likely explanation for the observed offset between the marine sedimentary pool and the exported particulate load. The isotopic offset observed for the marine sediments and groundwater composition, $\Delta^{138}Ba_{sediment\text{-}groundwater}$, was ≈ -0.2 ‰, which is smaller than the fractionation between seawater and the Ba in sinking particulate matter, suggesting that the porewaters constitute a mixture of Ba from the overlying seawater (due to irrigation and bioturbation) and some fraction of the sedimentary Ba pool, whether from barite or from another source, like Fe-Mn oxides. Given that the sinking particulate $\delta^{138}Ba$ depth profiles did not increase

with depth, it is likely that the dissolution process I speculate is occurring in the sediment does not occur while the particles are sinking. Therefore, this partial dissolution process would be occurring over timescales longer than the time it takes for particles to sink from the surface to the sediments in the GOA. These results suggest that the exported particulate load is isotopically controlled by the composition of sub-surface waters where barite forms, and that this signature is delivered with barite to the sediment. However, due to selective preservation of barite as a result of exposure to undersaturated seawater at the sediment-water interface, measuring sedimentary Ba isotopes may not represent the sinking particulate barite signature. In paleoceanographic applications, care must be taken to ensure that barite is the major Ba-carrying phase in analyzed sediments and, when attempting to interpret changes in δ^{138}Ba records, the potential for isotopically fractionating partial dissolution should be assessed before interpreting changes in the sediments equivocal to changes in dissolved Ba in seawater.

Conclusions

I report the first seawater δ^{138}Ba values for the GOA, the least saturated marine basin in the world with respect to barite (Monnin et al. 1999), which are vertically uniform at +0.56 ‰ ± 0.08 ‰. This value is significantly offset from the particulate flux, which displays a uniform value of +0.09 ‰ ± 0.06 ‰. Limited variability was observed between the two dissolved seawater profiles, despite considerable differences in hydrography, with one profile collected during water column stratification (October) and the other during deep mixing (January) times. This suggests that barite formation in this basin is not large enough to impact the water column Ba isotope values and, hence, that the Ba isotopes in the export load have a constant offset from seawater year-round (Δ^{138}Ba ≈ -0.47 ‰). The δ^{138}Ba composition of the sediments, however, is not similar to that of the sinking particulate load, which I suggest is likely due to partial or complete dissolution of barite and possibly other Ba carrying phases, which distorts the δ^{138}Ba composition of the sediments. This result cautions that future studies of δ^{138}Ba in marine archives ought to consider the Ω_{barite} of porewaters and overlying seawater when

interpreting changes in a record and that further research be conducted to directly constrain the potential for isotopic fractionation during partial dissolution of barite in sediments.

References

- von Allmen, K., Böttcher, M. E., Samankassou, E., & Nägler, T. F. 2010. "Minerals and Precipitation Experiments." *Chemical Geology,* 277(1): 70–77.
- Anderson, R. F., and Winckler, G. 2005. "Problems with Paleoproductivity Proxies." *Paleoceanography,* 20(3): 1–7.
- Bates, S. L et al. 2017. "Barium Isotopes Reveal Role of Ocean Circulation on Barium Cycling in the Atlantic." *Geochimica et Cosmochimica Acta,* 204: 286–99.
- Benaltabet, T., Lapid, G., and Torfstein, A. (In Review) "Seawater Pb Concentration and Isotopic Composition Response to Daily Time Scale Dust Storms in the Gulf of Aqaba, Red Sea." *Marine Chemistry*
- Biton, E. and Gildor, H., 2011. "The General Circulation of the Gulf of Aqaba (Gulf of Eilat) Revisited: The Interplay between the Exchange Flow through the Straits of Tiran and Surface Fluxes." *Journal of Geophysical Research: Oceans,* 116(8): 1–15.
- Bridgestock, L. et al. 2018. "Controls on the Barium Isotope Compositions of Marine Sediments." *Earth and Planetary Science Letters,* 481: 101–10.
- Cao, Z. et al. 2020. "Corrigendum to 'Constraining the Oceanic Barium Cycle with Stable Barium Isotopes'" *Earth and Planetary Science Letters* 530: 116003.
- Chen, Y. et al. 2007. "Estimates of Atmospheric Dry Deposition and Associated Input of Nutrients to Gulf of Aqaba Seawater." *Journal of Geophysical Research Atmospheres* 112(4): 1–14.
- Chen, Y. et al. 2008. "Sources and Fluxes of Atmospheric Trace Elements to the Gulf of Aqaba, Red Sea." *Journal of Geophysical Research Atmospheres* 113(5): 1–13.

- Chernihovsky, N., Torfstein A., and Almogi-Labin, A. 2018. “Seasonal Flux Patterns of Planktonic Foraminifera in a Deep, Oligotrophic, Marginal Sea: Sediment Trap Time Series from the Gulf of Aqaba, Northern Red Sea.” *Deep-Sea Research Part I: Oceanographic Research Papers* 140: 78–94.
- Chien, C., Benaltabet, T., Torfstein, A., and Paytan, A., 2019. “Contributions of Atmospheric Deposition to Pb Concentration and Isotopic Composition in Seawater and Particulate Matters in the Gulf of Aqaba, Red Sea.” *Environmental Science and Technology* 53(11): 6162–70.
- Cutter, G. A. et al. 2010. “Sampling and Sample-Handling Protocols for GEOTRACES Cruises.” (December).
- Eagle, M. et al. 2003. “A Comparison between Excess Barium and Barite as Indicators of Carbon Export.” *Paleoceanography* 18(1): 1021.
- Foster, R A, Paytan, A., and Zehr, J. P. 2009. “Seasonality of N 2 Fixation and NifH Gene Diversity in the Gulf of Aqaba (Red Sea).” *Limnology & Oceanography* 54(1): 219–33.
- Geyman, B. M., Ptacek, J. L., LaVigne, M., and Horner, T. J. 2019. “Barium in Deep-Sea Bamboo Corals: Phase Associations, Barium Stable Isotopes, & Prospects for Paleoceanography.” *Earth and Planetary Science Letters* 525: 115751.
- Griffith, E. M., and Paytan, A. 2012. “Barite in the Ocean - Occurrence, Geochemistry and Palaeoceanographic Applications.” *Sedimentology* 59(6): 1817–35.
- Hartman, A., Torfstein, A., and Almogi-labin, A. 2020. “Climate Swings in the Northern Red Sea over the Last 150,000 Years from εNd and Mg/Ca of Marine Sediments.” *Quaternary Science Reviews* 231: 106205.
- Horner, T. J. et al. 2017. “Pelagic Barite Precipitation at Micromolar Ambient Sulfate.” *Nature Communications* 8(1): 1–11.
- Horner, T. J., Kinsley, C. W., and Nielsen, S. G. 2015. “Barium-Isotopic Fractionation in Seawater Mediated by Barite Cycling and Oceanic Circulation.” *Earth and Planetary Science Letters* 430: 511–22.

- Hsieh, Y., and Henderson, G. M. 2017. “Barium Stable Isotopes in the Global Ocean: Tracer of Ba Inputs and Utilization.” *Earth and Planetary Science Letters* 473: 269–78.
- Katz, T. et al. 2015. “Desert Flash Floods Form Hyperpycnal Flows in the Coral-Rich Gulf of Aqaba, Red Sea.” *Earth and Planetary Science Letters* 417: 87–98.
- Labiosa, R. G. et al. 2003. “The Interplay between Upwelling and Deep Convective Mixing in Determining the Seasonal Phytoplankton Dynamics in the Gulf of Aqaba: Evidence from SeaWiFS and MODIS.” *Limnology and Oceanography* 48(6): 2355–68.
- Lazar, B., et al. 2008. "Recent environmental changes in the chemical-biological oceanography of the Gulf of Aqaba (Eilat)." *Aqaba-Eilat, the improbable gulf. Environment, biodiversity and preservation. Magnes Press, Jerusalem* (2008): 49-61.
- Levanon-Spanier, I., Padan, E., and Reiss, Z. 1979. “Primary Production in a Desert-Enclosed Sea- the Gulf of Eilat (Aqaba), Red Sea.” *Deep Sea Research Part A, Oceanographic Research Papers* 26(6): 673–85.
- Lindell, D., and Post, A. F. 1995. “Ultraphytoplankton Succession Is Triggered by Deep Winter Mixing in the Gulf of Aqaba (Eilat), Red Sea.” *Limnology and Oceanography* 40(6): 1130–41.
- Ma, Z. et al. 2015. “Export Production Fluctuations in the Eastern Equatorial Pacific during the Pliocene-Pleistocene: Reconstruction Using Barite Accumulation Rates.”: 1455–69.
- Mayfield, K. K. et al. In Review. “The Importance of Groundwater Discharge in the Marine Isotope Budgets of Li, Mg, Ca, Sr, and Ba.” *Nature Communications*
- Monnin, C., Jeandel, C., Cattaldo, T., and Dehairs, F. 1999. “The Marine Barite Saturation State of the World’s Oceans.” *Marine Chemistry* 65(3–4): 253–61.
- Paytan, A. and Kastner, M. 1996. “Benthic Ba Fluxes in the Central Equatorial Pacific, Implications for the Oceanic Ba Cycle.” *Earth and Planetary Science Letters* 142(3–4): 439–50.

- Riedinger, N, Kasten, S., and Gro, J. 2006. "Active and Buried Authigenic Barite Fronts in Sediments from the Eastern Cape Basin." *Earth and Planetary Science Letters* 241: 876–87.
- Shaked, Y., and Genin, A. 2018. *Israel National Monitoring Program at the Gulf of Eilat Annual Report*.
- Shellenbarger, G. G., Monismith, S. G., and Paytan, A. 2006. "The Importance of Submarine Groundwater Discharge to the Nearshore Nutrient Supply in the Gulf of Aqaba (Israel)." *Limnology & Oceanography* 51(4): 1876–86.
- Silverman, J., and Gildor, H. 2008. "The Residence Time of an Active versus a Passive Tracer in the Gulf of Aqaba: A Box Model Approach." *Journal of Marine Systems* 71: 159–70.
- Steiner, Z., Lazar, B., Torfstein, A., and Erez, J. 2017. "Testing the Utility of Geochemical Proxies for Paleoproductivity in Oxic Sedimentary Marine Settings of the Gulf of Aqaba, Red Sea." *Chemical Geology* 473(March): 40–49.
- Torfstein, A., and Kienast, S. S. 2018. "No Correlation Between Atmospheric Dust and Surface Ocean Chlorophyll-a in the Oligotrophic Gulf of Aqaba, Northern Red Sea." *Journal of Geophysical Research: Biogeosciences* 123(2): 391–405.
- Torfstein, A. et al. 2017. "Chemical Characterization of Atmospheric Dust from a Weekly Time Series in the North Red Sea between 2006-2010." *Geochimica et Cosmochimica Acta*. 211: 373-393.
- Torfstein, A. et al. In Review. "Bulk and Export Production Fluxes in the Gulf of Aqaba, Northern Red Sea." *ACS Earth and Space Chemistry*.
- Wankel, S. D. et al. 2010. "Sources of Aerosol Nitrate to the Gulf of Aqaba: Evidence from $\Delta^{15}N$ and $\Delta^{18}O$ of Nitrate and Trace Metal Chemistry." *Marine Chemistry* 120(1–4): 90–99.

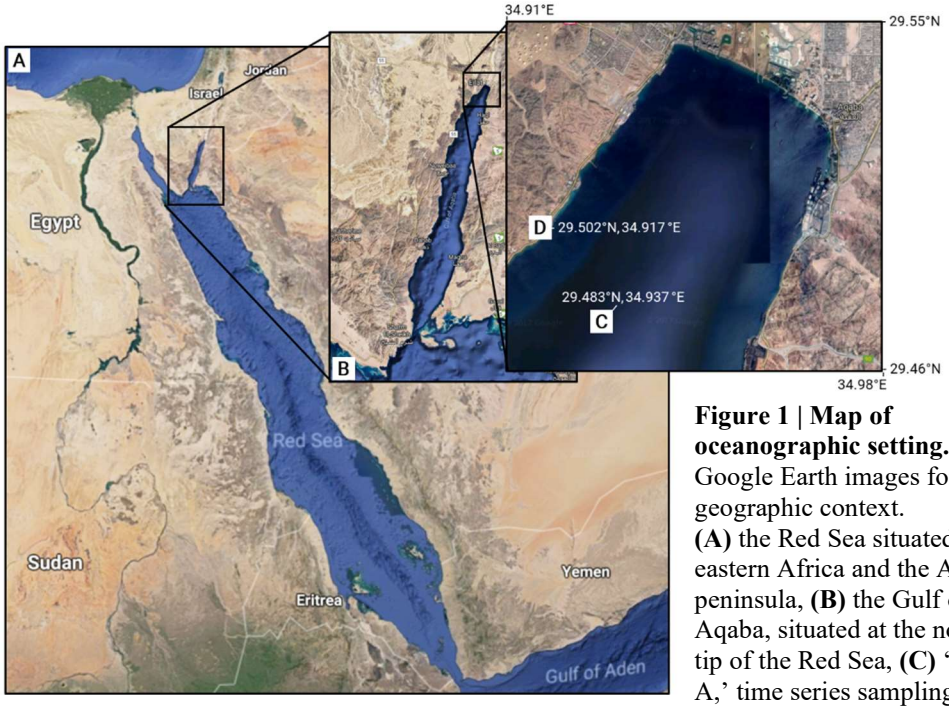

Figure 1 | Map of oceanographic setting. a-b, Google Earth images for relevant geographic context. **(A)** the Red Sea situated between eastern Africa and the Arabian peninsula, **(B)** the Gulf of Aqaba, situated at the northern tip of the Red Sea, **(C)** 'Station A,' time series sampling location for seawater and particulate time series, **(D)** Interuniversity Institute of Marine Science campus location, where groundwater and aerosol samples were collected (Eilat, Israel).

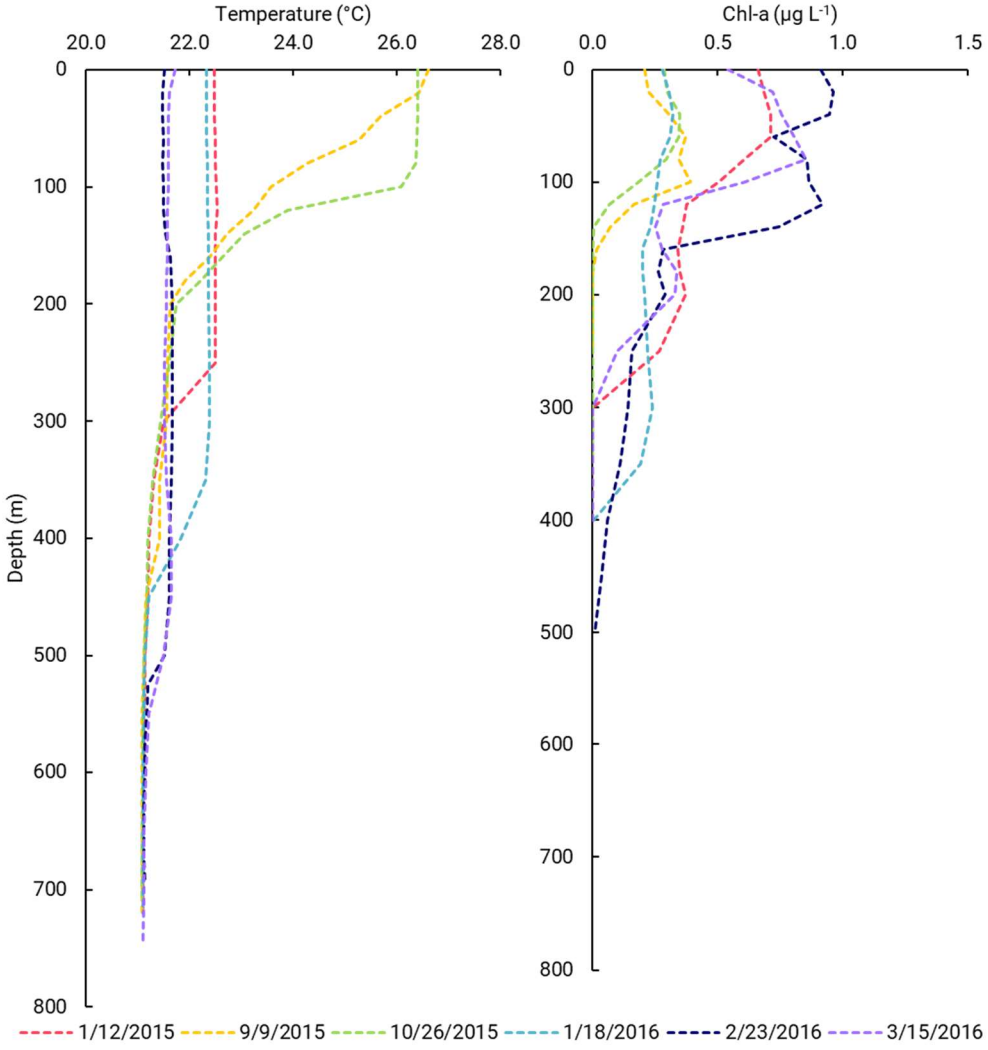

Figure 2 | Temperature and chlorophyll concentration depth profiles at Station A, 2015 - 2016. Data were sourced from Israel's National Monitoring Program (Shaked & Genin, 2018) and are color-coded to most closely match profiles to sampling dates relevant to this study.

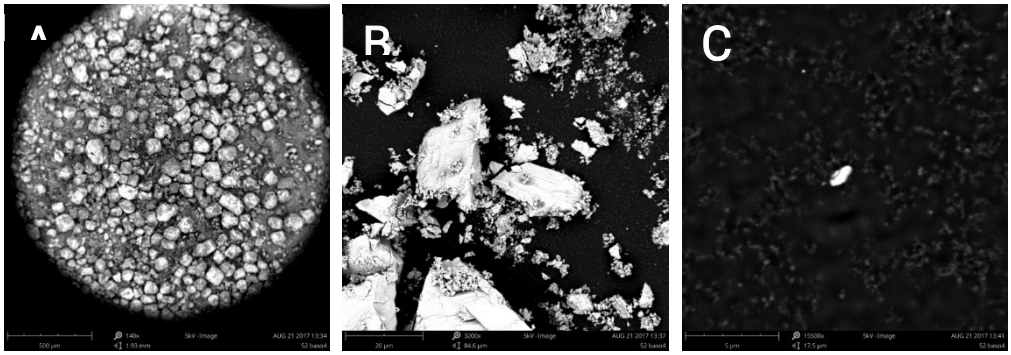

Figure 3 | Scanning electron microscope images of 'barite fraction' of sediment. (a) an overview of the residual fraction post-leaching at a 500 µm scale (pre-sieving), **(b)** a magnified view of the remaining sample at a 20 µm scale, and **(c)** a highly refractory mineral, which I suggest was likely barite, at the 5µm scale.

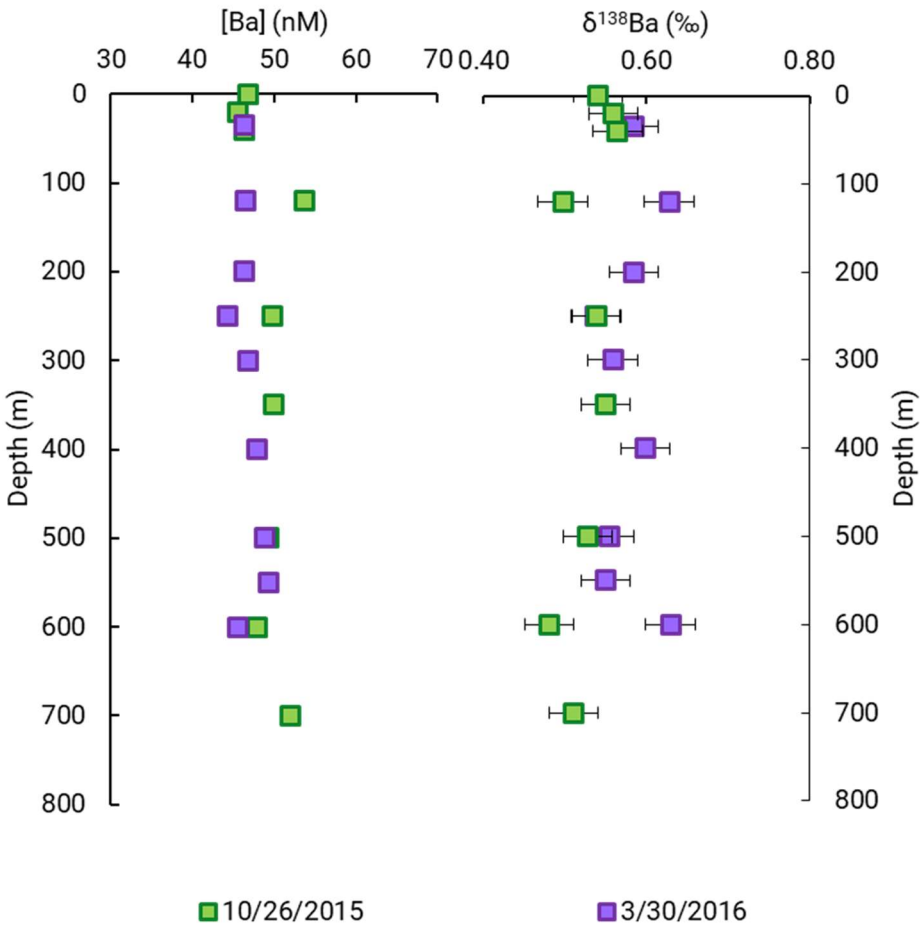

Figure 4 | Dissolved barium concentration and isotopic data in dissolved seawater of the GOA. The two profiles represent fall of 2015 and spring of 2016 **(A)** dissolved [Ba] in seawater, expressed in nM. Error bars represent the standard deviation of all blanks analyzed as a part of this sample set (n = 5), but are smaller than the symbol size. **(B)** δ^{138}Ba composition of the dissolved Ba load of seawater, where error bars represent the long-term analytical uncertainty of seawater standards (0.03 ‰).

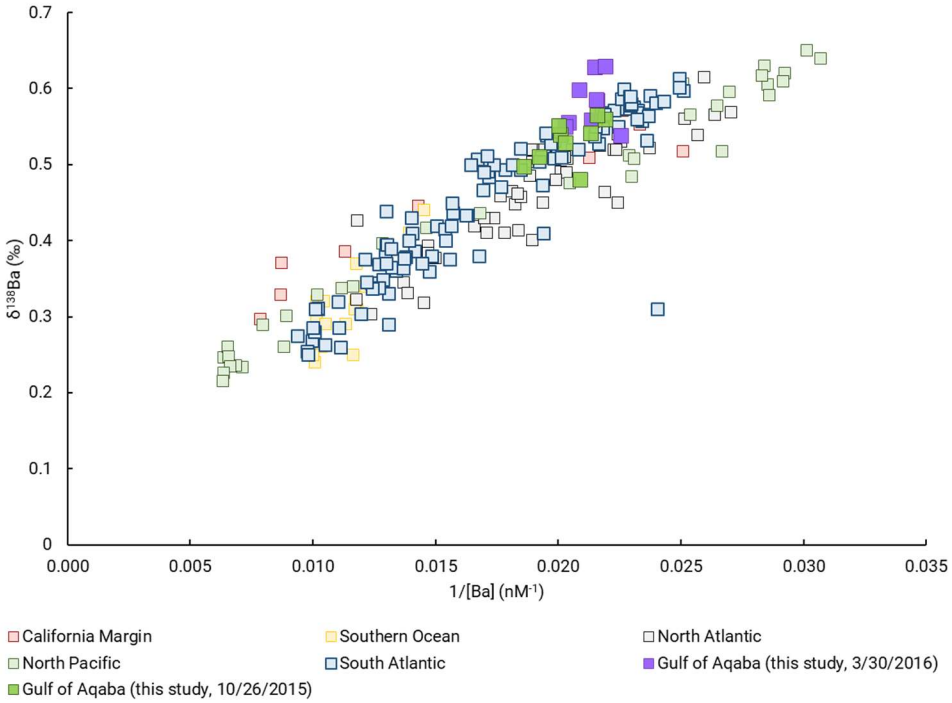

Figure 5 | Dissolved barium concentration and isotopic data from Gulf of Aqaba seawater, in a global context. 1/[Ba] vs. δ^{138}Ba, relative to other ocean basins. The results of this study in the Gulf of Aqaba are denoted in green and purple, which represent the two seasonal profiles. California Margin data are from Geyman et al. (2019). North Atlantic data are from Bates *et al.* (2017), Hemsing *et al.* (2018), and Hsieh and Henderson (2017). North Pacific data are from Hsieh and Henderson (2017) and Geyman *et al.* (2019). South Atlantic data are from Bates *et al.* (2017), Bridgestock *et al.* (2018), Hemsing *et al.* (2018), Hsieh and Henderson (2017), and Horner *et al.* (2015). Southern Ocean data are from Hemsing *et al.* (2018) and Hsieh and Henderson (2017).

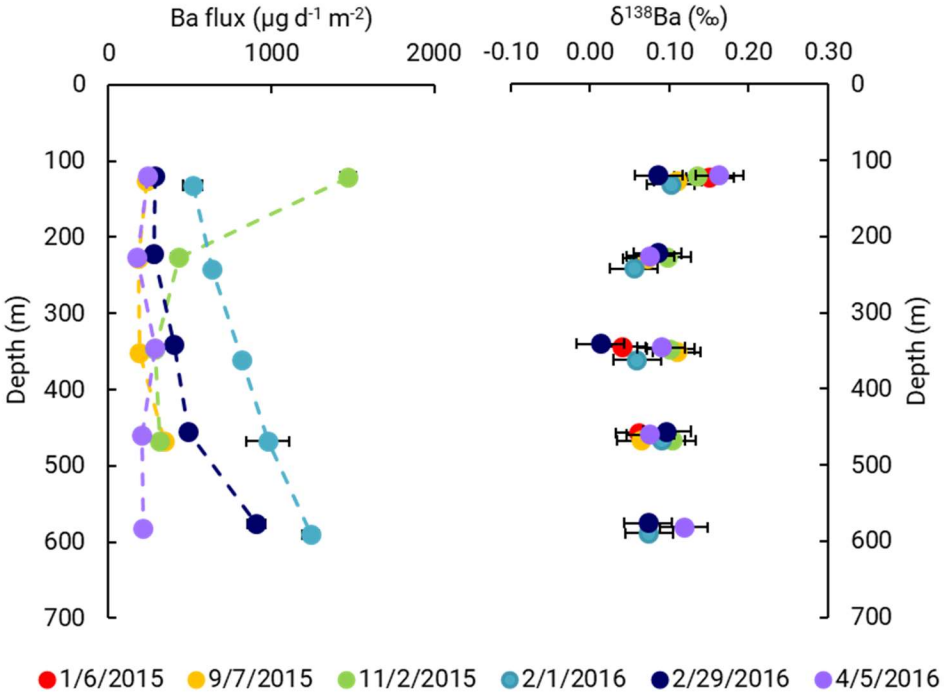

Figure 6 | Barium flux and isotopic composition of the particulate load from 1/6/2015 – 4/5/2016. (A) Ba flux calculated for each sediment trap of the time series, where the date represents the collection date of the ~monthly deployment. **(B)** δ^{138}Ba composition of the sediment trap samples. Color scheme in the legend applies to both flux and isotopic data.

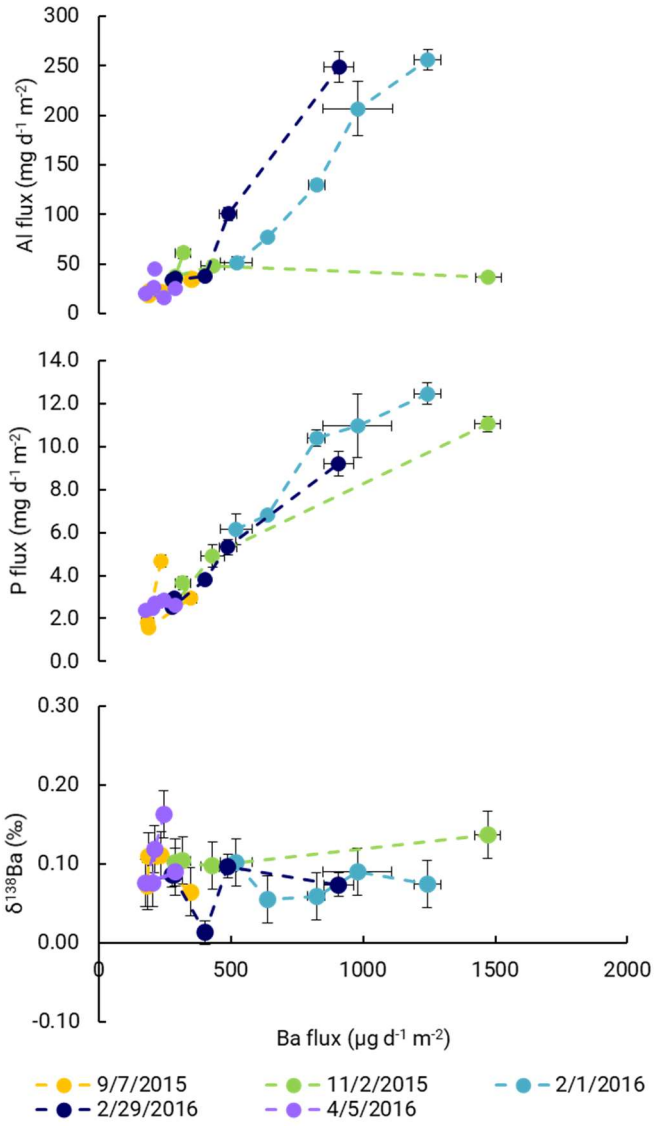

Figure 7 | Particulate Al and P fluxes, as well as the Ba isotopic composition of the particulates, relative to the particulate Ba flux. Colors represent fluxes calculated from different sediment trap profiles. Dates are representative of collection times **(A)** particulate Al vs. Ba flux, used to represent the relationship between Ba export and terrigenous dust sources **(B)** particulate P vs. Ba flux, used to represent

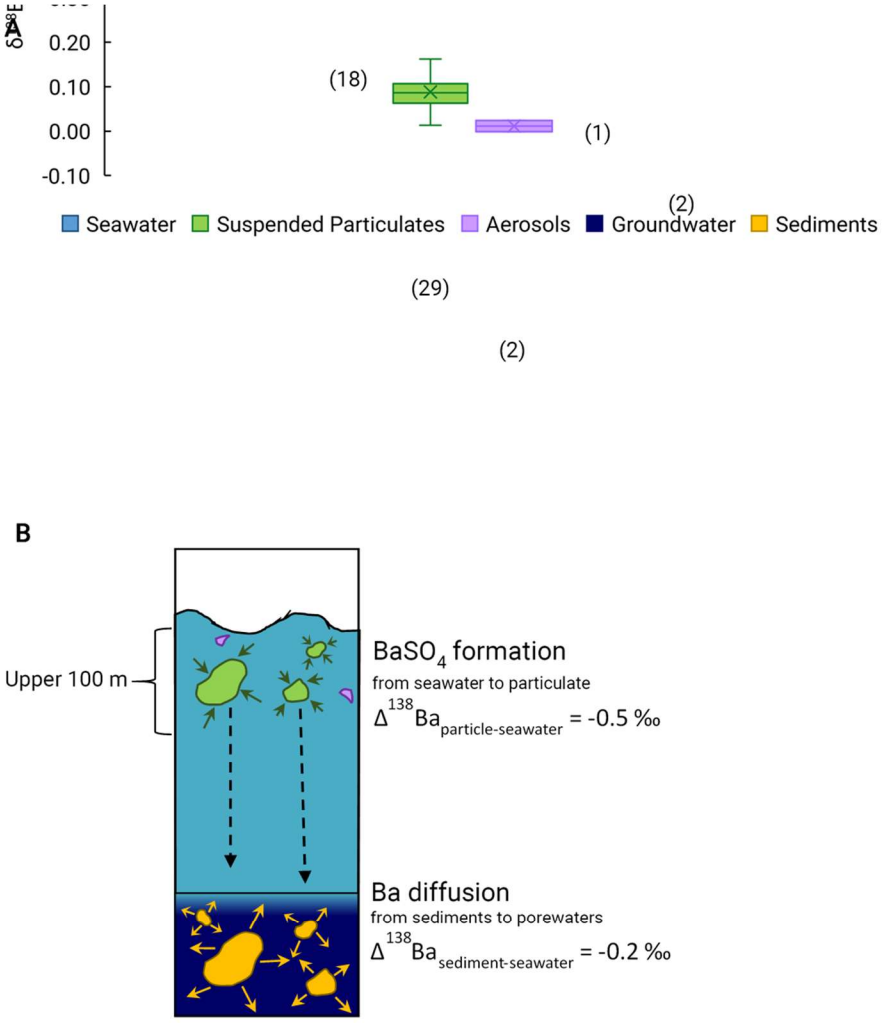

Figure 8 | Representations of the isotopic composition of Ba sources and sinks to the Gulf of Aqaba. (A) box-and-whisker plot of all samples analyzed in this study, where values atop the boxes represent the *n* for each sample type. **(B)** conceptual diagram of $BaSO_4$ formation in the surface waters and partial dissolution of barite in the sediments, as well as the isotopic offsets ($\Delta^{138}Ba$) observed between the pertinent reservoirs of Ba in this study.

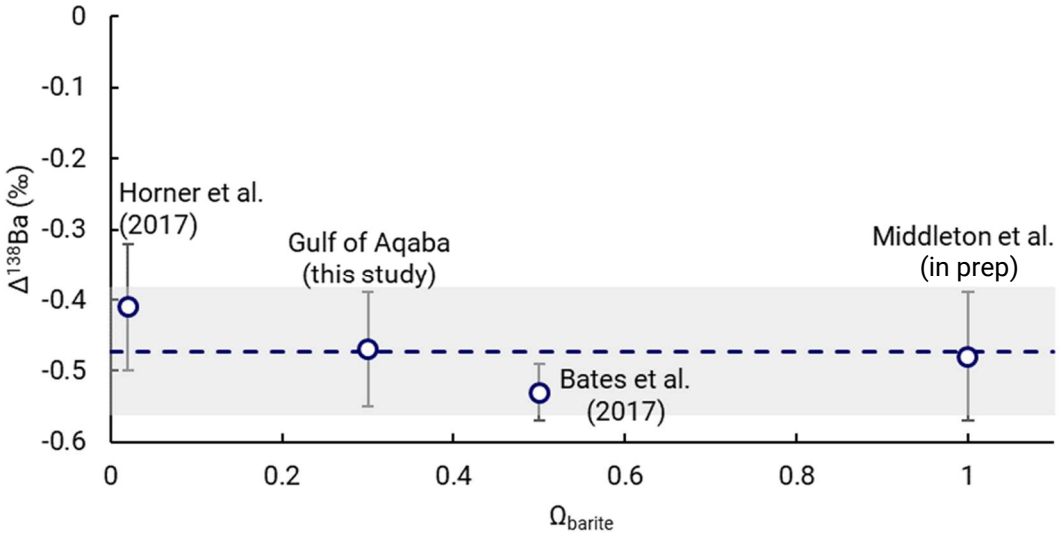

Figure 9 | Barium isotopic offset of particles from solution, relative to barite saturation state. $\Delta^{138}Ba$ was calculated by subtracting the seawater isotopic composition of Ba from the particulate load ($\delta^{138}Ba_{particle}$ - $\delta^{138}Ba_{seawater}$) and it is plotted against barite saturation state (Ω_{barite}). Dashed line represents the average of the four points (-0.46 ‰) and the shaded region represents the greatest uncertainty value amidst these points (0.09 ‰).

Table 1. [Ba] and $\delta^{138}Ba$ composition of dissolved seawater and groundwater samples

Parameter	Date mm/dd/yyy	Depth (m)	$\delta^{138}Ba_{NIST}$ (‰)	± 2 SD (‰)	[Ba] (nM)	±2 SD (nM)
Seawater	3/30/2016	35	0.58	0.04	46	1.2
Seawater	3/30/2016	120	0.63	0.04	47	1.2
Seawater	3/30/2016	200	0.58	0.04	46	1.2
Seawater	3/30/2016	250	0.54	0.04	44	1.2
Seawater	3/30/2016	300	0.56	0.04	47	1.2
Seawater	3/30/2016	400	0.60	0.04	48	1.2
Seawater	3/30/2016	500	0.55	0.04	49	1.2
Seawater	3/30/2016	550	0.55	0.05	49	1.2
Seawater	3/30/2016	600	0.63	0.04	46	1.2
Seawater	10/26/2015	0	0.54	0.03	47	1.2
Seawater	10/26/2015	20	0.56	0.03	46	1.2
Seawater	10/26/2015	40	0.56	0.03	46	1.2
Seawater	10/26/2015	120	0.50	0.03	54	1.4
Seawater	10/26/2015	250	0.54	0.03	50	1.3
Seawater	10/26/2015	350	0.55	0.03	50	1.2
Seawater	10/26/2015	500	0.53	0.03	49	1.3
Seawater	10/26/2015	600	0.48	0.03	48	1.3
Seawater	10/26/2015	700	0.51	0.03	52	1.3
Groundwater	8/24/2017	2	0.49	0.04	113	2.4

Chemical composition of Ba ([Ba] and $\delta^{138}Ba$) in all aqueous samples from this study in the Gulf of Aqaba.

Table 2. [Ba] and δ^{138}Ba composition of suspended particulate, aerosol, and sediment samples

Parameter	Date mm/dd/yyy	Depth (m)	δ^{138}Ba (‰)	± 2 SD (‰)	Ba flux (μg d^{-1} m^{-2})	± 2 SD	P flux (mg d^{-1} m^{-2})	± 2 SD	Al flux (mg d^{-1} m^{-2})	± 2 SD
Particulate	1/6/2015	123	0.15	0.03	-	-	-	-	-	-
	1/6/2015	345	0.04	0.03	-	-	-	-	-	-
	1/6/2015	458	0.06	0.00	-	-	-	-	-	-
	9/7/2015	127	0.11	0.03	236	14	4.7	0.3	22	1.3
	9/7/2015	229	0.07	0.03	184	25	1.8	0.2	19	2.6
	9/7/2015	352	0.11	0.03	189	10	1.6	0.1	22	1.1
	9/7/2015	468	0.06	0.03	347	23	2.9	0.2	35	2.3
	11/2/2015	121	0.14	0.03	1471	49	11.0	0.4	36	1.2
	11/2/2015	227	0.10	0.03	430	45	4.9	0.5	48	5.0
	11/2/2015	348	0.10	0.03	289	7	2.7	0.1	38	0.9
	11/2/2015	468	0.10	0.03	318	28	3.7	0.3	61	5.4
	2/1/2016	132	0.10	0.03	519	59	6.2	0.7	51	5.9
	2/1/2016	242	0.06	0.03	638	13	6.8	0.1	77	1.5
	2/1/2016	362	0.06	0.03	823	32	10.4	0.4	130	5.0
	2/1/2016	468	0.09	0.03	978	131	11.0	1.5	207	27.7
	2/1/2016	590	0.07	0.03	1242	51	12.5	0.5	256	10.4
	2/29/2016	120	0.09	0.03	286	24	2.9	0.2	35	3.0
	2/29/2016	222	0.09	0.03	277	20	2.5	0.2	34	2.4
	2/29/2016	341	0.01	0.04	402	17	3.8	0.2	38	1.6
	2/29/2016	456	0.10	0.03	488	33	5.3	0.4	100	6.7
	2/29/2016	576	0.07	0.03	907	56	9.2	0.6	249	15.3
	4/5/2016	120	0.16	0.03	245	22	2.8	0.3	16	1.5
	4/5/2016	226	0.08	0.03	177	4	2.4	0.1	20	0.5
	4/5/2016	346	0.09	0.03	290	1	2.6	0.0	25	0.0
	4/5/2016	460	0.08	0.03	205	8	2.5	0.1	27	1.0
	4/5/2016	582	0.12	0.03	210	13	2.7	0.2	45	2.8
Aerosol	1/15/2015	-	0.02	0.03	-	-	-	-	-	-
	8/6/2016	-	0.00	0.03	-	-	-	-	-	-
Sediment		0.02 – 0.05	0.32	0.03	-	-	-	-	-	-
		0.3	0.35	0.03	-	-	-	-	-	-

Chapter 5

Conclusion

The major (Mg, K, and Ca) and trace (Li, Sr, and Ba) elements of seawater examined in this thesis are well-mixed in the modern ocean, with residence times longer than meridional overturning of the ocean. Variations in their isotopic composition in marine archives have implications for reconstructions of paleo-hydrology, silicate weathering, carbonate formation/dissolution, oceanic circulation, and (perhaps) more. The utility of their non-traditional stable isotope systems, however, is predicated on a quantitative understanding of the magnitude and isotopic composition of their inputs to/outputs from the ocean.

In CHAPTER 2, I conducted the most complete characterization of the groundwater flux, which had been missing from most marine isotope budgets to-date, and found that groundwater-derived fluxes of Li, Mg, Ca, Sr, and Ba account for, at the minimum, 5 % of the riverine input. In addition to 'balancing the geochemical books', my results identify that the hydrologic controls on groundwater-derived fluxes are fundamentally decoupled from those of rivers—the former depending on relative sea-level and the latter on precipitation. I also found a remarkable sensitivity of Ba isotopes to terrestrial water inputs, hinting at potential proxy uses that should be valuable to modelers and paleoclimatologists alike.

In CHAPTER 3, I found that $\delta^{41}K$ and $\delta^{26}Mg$ inversely co-varied in the Fraser River main stem's dissolved load, which I argue is driven by silicate weathering, predominantly in the young, volcanic Coast Range. I also found a positive correlation between $\delta^{7}Li$ and $\delta^{26}Mg$, which is contrary to the relationship one would expect if these systems were responding solely to silicate weathering. I attribute this relationship to differences in the types (and, therefore, bonding surfaces/fractionation factors) of suspended clays in the river's particulate load over the course of the time series, driven by seasonal shifts in weathering provenance (Coast Range vs. Rocky Mountains). I also found a positive

relationship between $\delta^{44/42}$Ca and $\delta^{88/86}$Sr, which supports the body of work demonstrating that these isotope systems can be useful proxies for carbonate formation/dissolution. The combined results of this chapter provides a first-order approximation of how these isotope systems may co-vary globally if surficial processes were to shift from a regime dominated by young, volcanic bedrock (e.g. trap volcanism) to a regime dominated by erosion and weathering of collisional orogens dominated by ancient metasedimentary sequences (e.g. Himalayas).

In CHAPTER 4, I report the first seawater δ^{138}Ba values for the Gulf of Aqaba, which I constrained as +0.56 ‰ ± 0.08 ‰. I found that this isotopic composition of seawater was distinct from the particulate flux, which was constrained as +0.09 ‰ ± 0.06 ‰. I also found that neither seasonality or dust deposition (δ^{138}Ba: +0.01 ‰ ± 0.03 ‰), had a significant effect of the Ba isotopic composition of the exported particulate load. These results suggest that Ba isotopes in the marine export load are insensitive to regional changes in the Gulf of Aqaba and are constrained by an isotopic offset, Δ^{138}Ba, of ≈ -0.47 ‰, which is consistent with three other previous estimates of Δ^{138}Ba. However, I also found that this δ^{138}Ba composition of the export particulate load may experience diagenetic effects, such as partial dissolution, that isotopically fractionate the sediment, since sediments were heavier than the dissolved load, +0.34 ‰ ± 0.06 ‰. I argue that this is due to the undersaturation of barite in the overlying seawater and surficial porewaters.

Together, these chapters indicate that the non-traditional stable isotopes of Li, Mg, K, Ca, Sr, and Ba have a myriad of potential proxy applications in palaeoceanography and provide constraints on the inputs/output fluxes necessary to improve the accuracy of their marine isotope budgets. Looking to the future, I would most want to see global groundwater-derived solute fluxes expanded to more elements and isotope systems and with additional volumetric models/estimates. Additionally, I would like to see the Ba isotopic composition of coastal marine carbonates examined for potential relationships with terrestrial water inputs, with the aim of testing its sensitivity in the modern. For the

benefit of the Fraser River geochemical mixing model and our understanding of how these novel weathering proxies vary under a range of environmental conditions, with tributaries monitored more extensively to better constrain the concentration-discharge relationships in the tributaries.

Residents of the IUI coral nursery
Photo by Kimberley Bitterwolf

***

ʻAʻohe nui ka hana ke alu ʻia

No task is too big when done together by all

— ʻŌlelo Noʻeau, Hawaiian proverb